REVERSIBLE ATTRACTION-MEDIATED COLLOIDAL CRYSTALLIZATION ON PATTERNED SUBSTRATES

A Dissertation

by

GREGORY FERNANDES

Submitted to the Office of Graduate Studies of
Texas A&M University
in partial fulfillment of the requirements for the degree of

DOCTOR OF PHILOSOPHY

August 2008

Major Subject: Chemical Engineering

REVERSIBLE ATTRACTION-MEDIATED COLLOIDAL CRYSTALLIZATION ON PATTERNED SUBSTRATES

A Dissertation

by

GREGORY FERNANDES

Submitted to the Office of Graduate Studies of
Texas A&M University
in partial fulfillment of the requirements for the degree of

DOCTOR OF PHILOSOPHY

Approved by:

Chair of Committee,	Michael A. Bevan
Committee Members,	Paul S. Cremer
	James Silas
	Zhengdong Cheng
Head of Department,	Michael Pishko

August 2008

Major Subject: Chemical Engineering

ABSTRACT

Reversible Attraction-Mediated Colloidal

Crystallizaton on Patterned Substrates. (August 2008)

Gregory Fernandes, B.E., University of Mumbai;

M.S., Texas A&M University

Chair of Advisory Committee: Dr. Michael A. Bevan

In this dissertation we used tunable particle-particle and particle-substrate attraction to achieve reversible two-dimensional crystallization of colloids on homogeneous and patterned substrates. Total internal reflection and video microscopy techniques were used to quantify the interparticle and particle-substrate interactions in these colloidal systems. Equilibrium and dynamic simulations were then utilized to link these colloidal interactions to the experimental colloidal phase behaviour. The importance of the nature of the attractive interaction in successfully crystallizing colloids has also been documented.

The first set of experiments demonstrates the use of temperature and specific ion effects to reversibly control the net particle-substrate van der Waals (vdW) attraction. Colloidal stabilization was achieved via the use of adsorbed polymer brush layers. By using evanescent wave microscopy, we directly and precisely measured how temperature and specific ion effects control the dimensions of adsorbed polymer layers and hence the net van der Waals attraction in between the colloids and the substrate. However, the

magnitude of the van der Waals attraction decays very rapidly with increasing surface separation and is therefore not conducive to the self assembly of colloidal crystals.

We successfully used thermoresponsive polymer nanoparticles to control the depletion attraction between micron sized silica particles and thereby induced reversible crystallization of the micron sized silica colloids on homogeneous substrates. Video and evanescent wave microscopy techniques were used to measure the nanoparticle-induced attractive interaction as a function of temperature. The experimentally observed phase behaviour was verified via simulations that utilized knowledge of the measured colloidal depletion interactions.

Finally, patterned surface topologies were used to position attractive colloidal crystals. Simulations were used to link the measured colloidal interactions to experimental phase behaviour as well as substrate topology. An extension of the concepts developed in this dissertation might suggest a general strategy to assemble colloidal particles into robust and annealable crystals contributing to the fabrication of photonic bandgap materials.

To my mum and dad

ACKNOWLEDGMENTS

I would like to begin by thanking my dearest Mum and Dad for their infinte warmth, love and support. A massive thank you to my dearest brother John for patiently listening to my rants all these years. A special word of thanks to my wonderful cousins Siddharth, Rohan, Samantha and Robert. Writing this dissertation would have driven me insane if it weren't for one Ya-Wen Chang who took time off from her busy schedule to listen to my litany of complaints. I owe a big thank you to my advisor, Dr. Michael Bevan, whose guidance and encouragement have been invaluable. I would also like to thank my committee members, Dr. Paul Cermer, Dr. Zhengdong Cheng and Dr. James Silas for their willing support and help along the way.

Thank you Pradip, my raquetball buddy and officemate, for the ready ear you lent to my ridiculous ideas. A special word of thanks to Samartha for always being ready to help me with even the most stupid difficulties. Thank you, Hung-Jen for your help with experiments, code and Taiwanese culture. A big thank you to my dear friend Neil Everett for helping me out with difficulties, both lab related and otherwise. Thank you Richard for bringing your own brand of humor to graduate school. Thanks also to Daniel, my partner in crime when it came to procrastination. I would also like to thank Shannon, an expert experimentalist and baker. A massive thank you also to Towanna, Missy and Barbara, without whom I would not have completed my studies. Thank you Jingyi for being so generous with the microgel particles. Thanks also to all my friends who made my stay in College Station an enjoyable one.

TABLE OF CONTENTS

Page

Page

Page

LIST OF FIGURES

FIGURE Page

FIGURE Page

FIGURE Page

FIGURE Page

FIGURE Page

FIGURE Page

FIGURE Page

FIGURE Page

FIGURE Page

LIST OF TABLES

1. INTRODUCTION

1.1. Background

Colloids are tiny, 1nm-10μm particles that exhibit a range of interesting properties when dispersed in a solvent, the most important of which is Brownian motion, a result of thermal fluctuations in the dispersion medium. A colloidal dispersion may assume a fluid, solid or gel state depending on how these minute particles interact across the solvent in which they are dispersed. The source of this rich phase behavior stems from the delicate interplay between the Brownian force and a variety of attractive and repulsive forces that dictate the interactions between matter at the colloidal length scale. Colloidal systems, be they a stable fluid, an ordered crystal or a gel, find a wide range of industrial applications including inks, paints, personal care and cosmetics.[1,2] The ordered colloidal state is of particular importance to the fabrication of optical devices and photonics.[3]

Semiconductor technology uses the atomic lattice of semiconductor materials to control the propagation of electrons. A photonic bandgap material is an optical analogue of the electronic bandgap material (semiconductor) wherein a lattice of macroscopic dielectric media (photonic crystal) controls the propagation of photons (Figure 1.1a).[4-8] Devices based on the manipulation of light allow greater amounts of information to be transferred at a quicker rate and with lesser energy losses than their electronic cousins.[9]

This dissertation follows the style of The Journal of Chemical Physics.

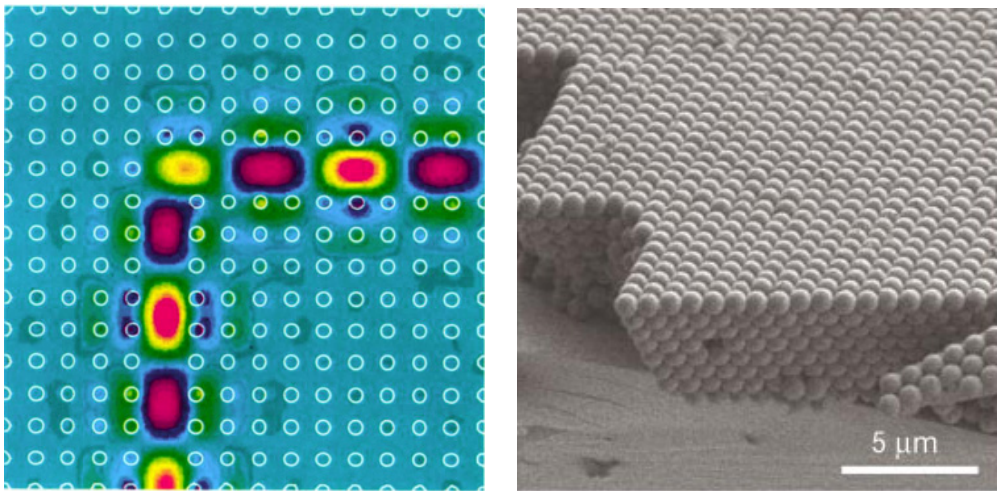

(a) (b)

Figure 1.1. (a) Light propagation around a sharp corner in a waveguide carved out of a square lattice of dielectric rods.[9] (b) A colloidal crystal of 855nm particles assembled on a planar Si substrate.[10]

To successfully fabricate such a photonic bandgap material, the size of the lattice constant of a photonic crystal must be on the order of the wavelength of light.[3,9] Colloidal crystals provide a simple, fast and cheap option for the successful fabrication of photonic crystals and the vast array of device applications they entail (optical switches, waveguides, high-efficiency diodes and 3D mirrors).[3,10] However for this to be a reality, we must first be able to fabricate mechanically robust, spatially controlled colloidal crystals, a challenge that has eluded research efforts thus far (Figure 1.1b).

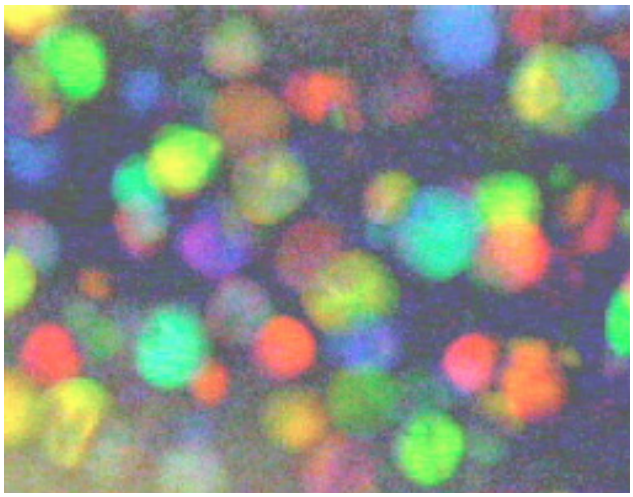

Figure 1.2. Electrostatic crystals of charged latex colloids 68nm in diameter at a volume fraction of ϕ=0.003 in deionized water.[11]

Colloids self-assemble into ordered structures at volume fractions that depend upon the nature of their mutual interaction. Conditions under which dispersions of hard sphere colloids crystallize (~50% v/v) have been verified by both simulation[12] as well as experiment.[13-17] Long ranged repulsion between colloidal particles permits the formation of electrostatic crystals at much lower volume fractions as shown in Figure 1.2.[11,18] However the shear modulus of these crystals is low due to the large surface separation between the constituent colloids, a shortcoming that can be overcome by crystallizing colloids with the use of short ranged attractive interactions. Colloids can also self assemble into crystalline structures when the nature of the interaction between them is attractive.

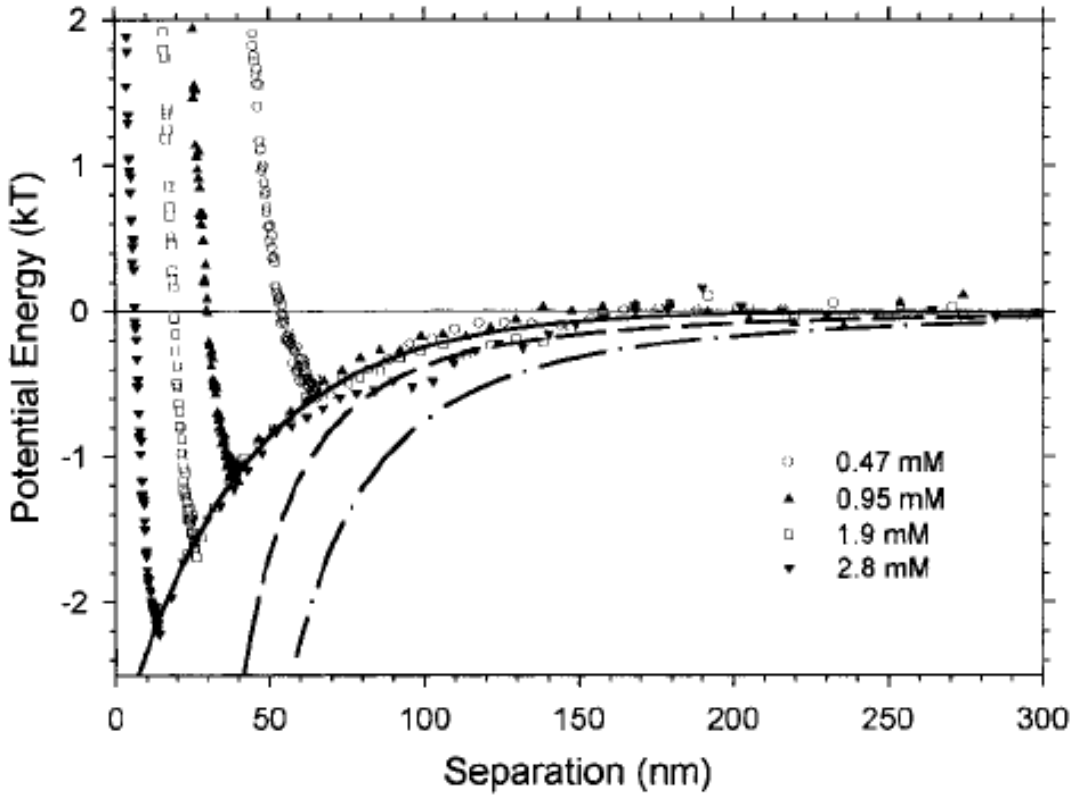

Figure 1.3. Net potential energy profile for a 6μm PS particle interacting with a glass substrate in an aqueous salt solution. The body force of gravity has been subtracted. Increasing salt concentration decreases the closest separation sampled by Brownian motion and increases the van der Waals attraction.[19]

In the absence of a repulsive force, colloidal particles dispersed in a solvent with different dielectric properties will always aggregate via Brownian collisions due to attractive dispersion forces. Past studies have quantified how ionic electrostatic repulsion can be used to mediate the closest separation between colloids and thereby the van der Waals attraction between them (Figure 1.3).[19] A similar effect called "steric stabilization" can be achieved by the adsorption or anchoring of polymer onto the

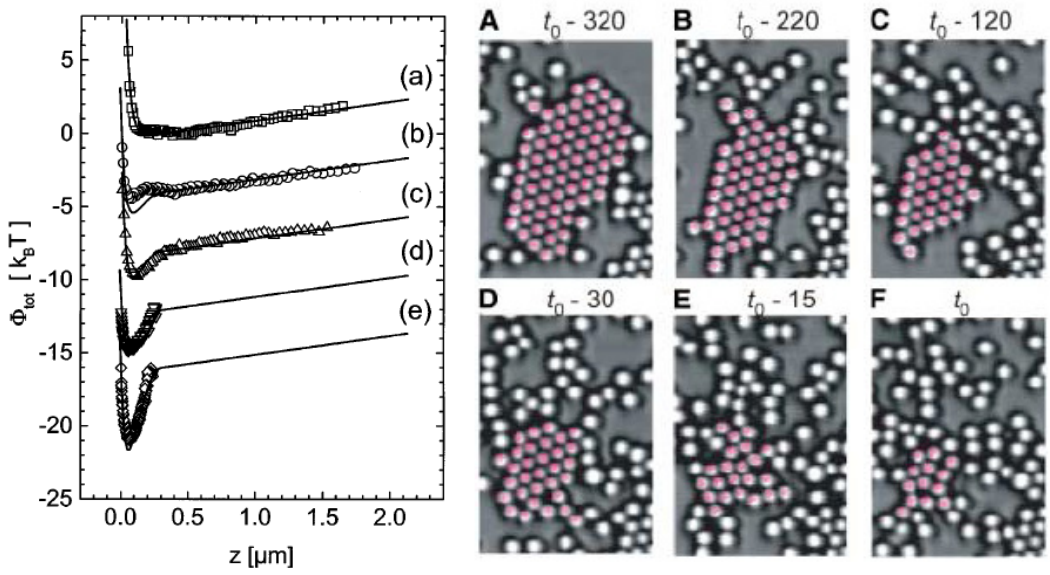

(a) (b)

Figure 1.4. (a) Increasing depletion attraction contribution with increasing non-adsorbing bulk PEO concentration (a-e) to the net interaction profile between a PS sphere and a wall measured using total internal reflection microscopy (TIRM).[20] (b) Sublimation of depletion-induced colloidal crystals comprised of 0.7μm PS colloids.[21]

surface of the colloidal particles. Steric stabilization depends on the thickness of the adsorbed polymer layers and their interaction with the surrounding solvent and the core particle ad well as adsorbed brush layer contributions to the van der Waals attraction. Polyethylene oxide (PEO) has been widely used for steric stabilization of colloids.

Changing the adsorbed polymer layer thickness directly controls the amount of van der Waals attraction in sterically stabilized colloidal dispersions. Control over PEO layer thickness can be achieved via temperature or specific ion effects.[22-28] Past studies have shown that PEO layers undergo a reversible change in their dimensions with changes in either the temperature or the concentrations of specific ions. Continuum van

der Waals interactions between sterically stabilized colloids and glass substrates have been quantified.[29] Rheology studies have also investigated van der Waals attraction-induced gellation in systems PEO stabilized latex particles due to temperature and specific ion mediated polymer layer collapses.[30,31] In this dissertation we report studies that show equivalent temperature and specific ion tunablity of polymer layer thickness-mediated van der Waals attraction between colloids and surfaces.[32]

An attractive "depletion" interaction can also be induced between colloids by the addition of non-adsorbing polymer, surfactant micelles or smaller colloids.[33] Direct quantitative measurements of the depletion attraction between colloids[34-36] and between colloids and surfaces[20,37-42] have been reported (Figure 1.4a). The propensity of dissolved non-adsorbing polymer to effect attraction induced crystallization of colloids has also received considerable theoretical[43-45] and experimental[46-55] attention. The same depletion attraction has also been used to induce phase separation in binary colloidal suspensions in bulk,[56-62] interfacial[63] and two-dimensional[64-68] systems. However, barring a single micellar depletant study,[21] no work has been conducted on exploiting thermoresponsive polymer microgel particles as a means of obtaining a tunable depletion attraction (Figure 1.4b). There have been no reported studies using directly measured, tunable attractive depletion forces to explain the phase behavior of binary colloidal systems. The development and characterization of such a system represents a significant advancement as it would allow the assembly of mechanically robust colloidal crystals that could be annealed via cycling of the depletion attraction for crystal defect elimination. One of the main findings of this dissertation is the successful use of cross-

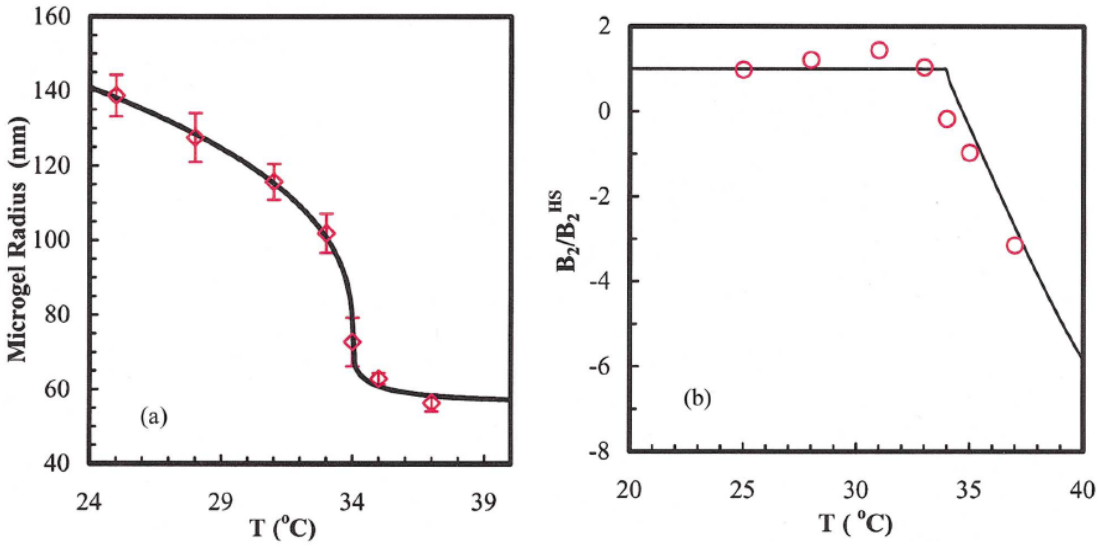

(a) (b)

Figure 1.5. (a) Size of PNIPAM microgel colloids as a function of temperature.[69] (b) Normalized osmotic second virial coefficients for the PNIPAM colloids obtained from dynamics light scattering. B_2^{HS} is the hard sphere second virial coefficient.[69]

linked poly(N-isopropyl acrylamide) or PNIPAM microgel particles in inducing reversible attractive interfacial colloidal crystallization.

Like PEO, PNIPAM is a synthetic thermoresponsive macromolecule that becomes insoluble upon heating in an aqueous solution.[70,71] The LCST of PNIPAM (~31°C) can also be reduced by the addition of specific salts whose anions follow the Hofmeister series,[72-77] a classification of ions based on their ability to precipitate proteins out of solution. The phase behavior of crosslinked PNIPAM microgel particles[78] has been characterized and reveals that the microgel particles behave like hard spheres at temperature below the LCST (Figure 1.5).[69] These PNIPAM particles shrink with

increasing temperature, an effect that is completely reversible (Figure 1.5a).[69] PNIPAM is also very sensitive to the pH and the ionic strength of the surrounding solvent. In this dissertation we use these tunable, reversible properties of PNIPAM in conjunction with TIRM[79-81] to perform the first direct measurements of tunable depletion attraction.

Spatial control over interfacial colloidal crystallization is crucial for the successful fabrication of photonic bandgap materials. Colloidal epitaxy, a method wherein a physical, chemical or biomolecular patterned substrate or template is used to direct the crystallization of sedimenting colloids serves this purpose.[82-84] A large majority of template directed colloid assembly employs strong attractive interactions to cause irreversible deposition of colloids on surfaces,[85,86] resulting in disordered aggregates rather than crystals. Template directed colloidal assembly with a fixed depletion potential has been used to form crystals on periodically patterned substrates.[87] Recently a comprehensive investigation into the influence of the patterned substrate on the structure and dynamics of an interfacial colloidal fluid was performed for a purely repulsive 2D system of SiO_2 colloids in equilibrium with a physically patterned substrate.[88] Herein, we report the first experiments that combine tunable depletion attraction and physical substrates to engineer reversible, spatially controlled 2D colloidal crystallization.

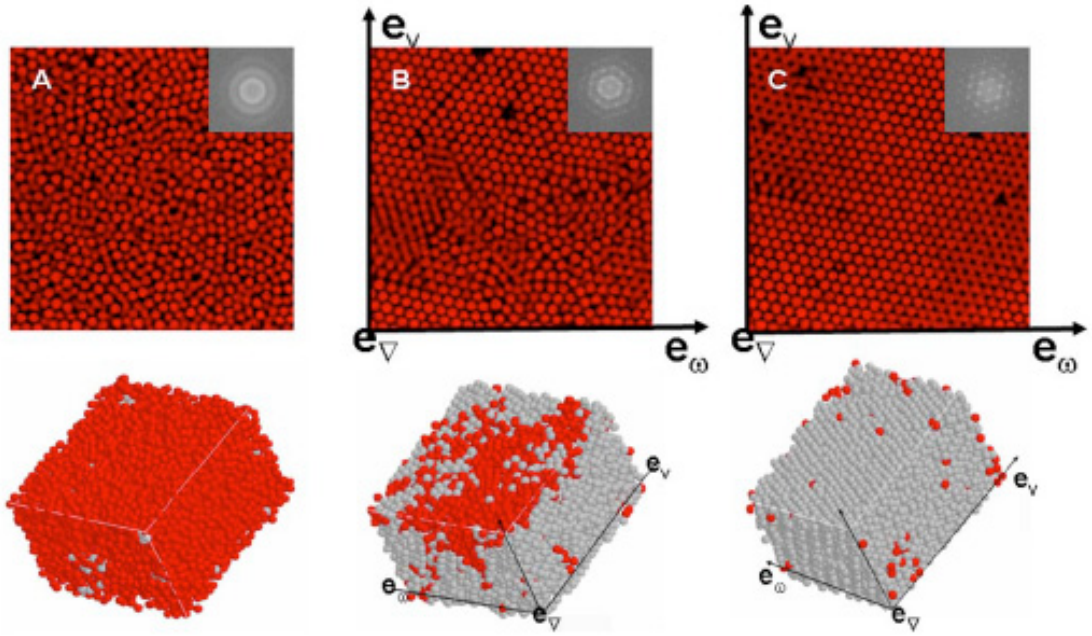

(a) (b) (c)

Figure 1.6. (a) A quiescent suspension of 48% (v/v) poly(methyl methacrylate) colloids before the application of shear, (b) after 5mins and (c) 10mins of shear showing increasing crystallinity with time.[89]

The methods for assembly of colloids reviewed thus far are all termed as "self-assembly methods". These approaches rely on the spontaneous assembly of colloids without the influence of an external field (other than gravity). The ordering of colloids can be induced via external control involving manipulation with fields such as shear,[89] electric,[90,91] magnetic,[92] optical,[93-95] and flow[96,97] (Figure 1.6). Most literature studies however rely solely on the external field to induce order. Ordering thus induced is lost once the field is removed unless some extra attractive interaction is present to maintain the field induced structure. These methods, if correctly applied to attractive systems

could be tremendously helpful in enabling experimentalists to avoid kinetically arrested states that occur in systems with high amounts of attraction.[49,59,98-103] External fields can also be used to speed-up the timescales for crystallization via formation of metastable intermediates.

Robust, spatially controlled, annealable, defect-free colloidal crystals are highly desirable for their potential applications to photonics. From the review presented above, it is clear that most literature studies have successfully addressed at most two of the above mentioned goals. By exploiting the thermosensitivity of the synthetic macromolecule, we propose the use of a system that successfully allows reversible, attraction driven colloidal crystallization on homogeneous and patterned substrates, thereby providing a path to achieving all of the aforementioned goals.

1.2. Objectives and Significance

The main objective of this dissertation is to design a colloidal system in which the magnitude and the range of interparticle and particle-substrate attraction can be tuned sensitively and reversibly in order to achieve 2D equilibrium interfacial colloidal crystallization on homogeneous and patterned surfaces. This dissertation documents the quantitative characterization of the system, its components, the prevalent forces and how they directly affect the observed phase behavior. The overall approach involves the use of advanced optical microscopy techniques like total internal refection (TIRM)[79] and video (VM)[104] microscopy to directly measure interfacial colloidal system interactions, dynamics and structure followed by the use of appropriate theoretical tools like Monte

Carlo (MC)[105,106] and Stokesian Dynamics (SD)[107] to interpret and predict the aforementioned experimental observations. The goal is to be able to self-assemble spatially controlled, robust colloidal crystals whose defects can be eliminated by annealing for emerging advanced material applications. Central questions related to attaining these objectives are:

- How can short ranged particle-particle and particle-surface attraction be reversibly controlled on the order of kT ?
- How can control over attraction in 2D colloidal systems be used to induce reversible interfacial crystallization on homogeneous substrates?
- How can spatial control over attraction induced crystallization in 2D colloidal systems be achieved?
- How can we achieve spatially controlled, attraction-mediated colloidal crystallization on patterned-surfaces independent of their size, shape and nature?

The strategy adopted in this dissertation to address these issues consists of a systematic series of experiments and simulations directed towards understanding a) how adsorbed or bulk polymer solvent quality effects mediate short-ranged colloid-colloid and colloid-substrate attraction, b) how these tunable attractions influence the equilibrium structure and dynamics of interfacial colloids on homogeneous substrates and c) how periodic interfacial colloid density enhancements induced by physically patterned substrates influence the equilibrium structure and dynamics of the self-same interfacial colloidal system. The overarching objective of this research, therefore, is to develop a method whereby the colloids can be reversibly self-assembled into robust

crystals of any shape at desired locations. The specific objectives of this research work are summarized below:

- Quantify the temperature and specific-ion-mediated collapse of stabilizing PEO brush layers adsorbed on silica particles via direct TIRM measurements of silica particle-silica substrate van der Waals attraction at different solvent conditions. Knowledge of how adsorbed polymer layers respond to changes in temperature and ion concentration allows us to sensitively control van der Waals interactions between the colloids they stabilize. Understanding how to manipulate such interactions between polymer coated colloids provides the ability to reversibly control the stability, phase behavior, and self-assembly of such particles.
- Utilize the temperature mediated collapse of non-adsorbing bulk PNIPAM microgel nanoparticles to induce tunable silica particle-particle and particle-substrate depletion attraction and quantify our findings with direct TIRM and VM measurements.
- Use the temperature-tunable depletion attraction to manipulate the equilibrium interfacial phase behavior of the silica colloids on homogeneous substrates. Use prior knowledge of the depletion forces in MC and SD simulations to verify the structure and dynamics of the experimentally observed equilibrium phases.
- Utilize physically patterned substrates to achieve spatial control over the location of the depletion crystals. Quantify the effect of the underlying substrate on the structure and dynamics of the colloids that diffuse over it. As with the previous study on homogeneous substrates, we will use prior knowledge of the

depletion forces in MC and SD simulations to verify the structure and dynamics of the experimentally observed equilibrium phases.

- Conduct MC simulation studies to generate phase diagrams that isolate conditions for depletion attraction driven colloidal crystallization on patterned substrates independent of feature size, shape and nature.

The significance of the dissertation work derives from the use of colloids as essential building blocks in emerging technologies based on nanostructured materials such as protein crystals,[108] magnetic storage devices,[92] chemical & biological sensors,[109] optical switches,[110] and photonics.[10] As mentioned as the start of this Section, colloidal crystals, on account of their size, provide a simple, fast and cheap option for the successful fabrication of photonic crystals and the vast array of device applications they entail (optical switches, waveguides, high-efficiency diodes and 3D mirrors).[3,10] However for this to be a reality, we must first be able to fabricate mechanically robust, annealable, spatially controlled colloidal crystals, a challenge that has eluded research efforts thus far. This dissertation details the characterization of a system that allows equilibrium attraction-mediated colloidal self-assembly on patterned substrates, a method that, in essence, satisfies all the criteria required for colloidal crystals to the successfully applied to the fabrication of photonic bandgap devices.

1.3. Dissertation Outline

This dissertation is organized as follows: Section 2 briefly reviews the characteristic interaction potentials in systems containing spherical colloidal particles immersed in an aqueous solution. In addition, the theoretical aspects concerning Monte Carlo and Stokesian Dynamic simulations are discussed. Section 3 provides details of the colloidal systems and optical microscopy experiments including protocols for fabricating physical and chemical patterns on glass substrates. Sections 4-7 contain the results from this research work. Detailed total internal refection microscopy (TIRM) measurements of silica colloid-substrate van der Waals attraction as a function of solvent quality mediated adsorbed polymer layer collapse are described in Section 4. Synergistic TIRM and VM experiments and MC and SD simulations of temperature tunable depletion attraction and the resulting interfacial colloidal phase behavior are described in Section 5. The use of physically patterned substrates to control the spatial location of attraction induced crystallization is demonstrated in Section 6. Extensive MC simulations aimed at isolating attraction-induced crystallization conditions on patterns of any shape, size or nature are described in Section 7. A summary of the findings of this dissertation is provided in Section 8. Finally, current and future work not presented as part of this dissertation is summarized in Section 9.

2. THEORY

2.1 Colloidal and Surface Forces

Brownian motion, a manifestation of the kinetic energy imparted to a colloid by the impacting solvent molecules that surround it, has a direct bearing on both the phase behavior and the dynamics of colloidal systems. The atomic system like phase behavior exhibited by colloidal suspensions stems from the balance between the conservative interparticle forces and is also dependent on the kinetic energy of the colloids. Viscous dissipative forces arising from the motion of colloidal particles in the surrounding solvent determine the dynamics of the said phase. As a result, any colloidal self-assembly study necessitates a comprehensive treatment of both the conservative and dissipative forces and their relation to the accompanying phase behavior. In this section, we discuss the various conservative interparticle forces that we measure, quantify and document the effects of in our experiments.

The balance of conservative forces can be expressed in the form of a net interaction potential $u(h)$ between two colloidal particles. An important distinction needs to be made between particle-wall and particle-particle interactions. The net potential energy profile for a single colloid levitated above a wall is obtained by adding the body force of gravity to the various surface forces acting on the particle. Relevant interactions presented in this dissertation include soft electrostatic repulsion, $u_{edl}(h)$, hard wall repulsion due to adsorbed polymer brush layers, $u_{steric}(h)$, van der Waals attraction, $u_{vdw}(h)$ and depletion attraction, $u_{dep}(h)$. The net separation dependent particle-wall

interaction potential $u_{pw}(h)$ can therefore be expressed as,

$$u_{pw}(h) = u_{edl}(h) + u_{steric}(h) + u_{vdw}(h) + u_{dep}(h) + u_{grav}(h) \tag{2.1}$$

where h is the particle-wall surface-to-surface separation. The particle-particle interaction potential $u_{pp}(h)$ is obtained in the same way, sans the addition of the body force of gravity.

$$u_{pp}(h) = u_{edl}(h) + u_{steric}(h) + u_{vdw}(h) + u_{dep}(h) \tag{2.2}$$

where h is the surface-to-surface separation between two colloidal particle centers. As will become evident in the subsequent discussion, the electrostatic, van der Waals and depletion interaction contributions are different for the particle-wall and particle-particle cases.

2.1.1 Electrostatic Interactions

Most surfaces immersed in water acquire a charge, which in turn modifies the distribution of free ions in solution. The silica colloids used in experiments presented in this dissertation acquire their surface charge by dissociation of surface silanol groups. This acquired surface charge, which results in a surface potential, is balanced by an atmosphere of counterions close to the surface, known as a diffuse electrical double layer whose characteristic length is referred to as the Debye length κ^{-1}. For thin electrical double layers, where the Debye length is smaller than particle-wall surface separations (κh>1) and much smaller than the sphere radius (κa>1), the electrostatic particle-wall interaction, $u_{edl}(h)$, is accurately described using the non-linear

superposition and the Derjaguin approximations. For the specific case of a 1:1 electrolyte, the interaction is expressed as,[79]

$$u_{edl}(h) = B_{pw} \exp(-\kappa h) \tag{2.3}$$

$$B_{pw} = 64\pi\varepsilon a \left(\frac{kT}{e}\right)^2 \tanh\left(\frac{e\Psi_p}{4kT}\right) \tanh\left(\frac{e\Psi_w}{4kT}\right) \tag{2.4}$$

$$\kappa = \left(\frac{2CN_A e^2}{\varepsilon kT}\right)^{0.5} \tag{2.5}$$

where a is the particle radius, ε is the dielectric permittivity of water, k is Boltzmann's constant, T is the absolute temperature, e is the elemental charge, ψ_p and ψ_w are the Stern potentials of the particle and the wall, C is the bulk electrolyte concentration, and N_A is Avagadro's number. The corresponding electrostatic interaction between identical particles is expressed as,

$$u_{edl}(h) = B_{pp} \exp(-\kappa(h)) \tag{2.6}$$

$$B_{pp} = 32\pi\varepsilon a \left(\frac{kT}{e}\right)^2 \tanh\left(\frac{e\Psi_p}{4kT}\right) \tanh\left(\frac{e\Psi_w}{4kT}\right) \tag{2.7}$$

At the lower salt concentrations reported in this dissertation (1.5mM in Sections 5&6), the κ^{-1} value (7.84mM) result in an electrostatic repulsive contribution which kinetically stabilizes colloids in a secondary minimum. Other studies conducted in this work used high salt concentrations (400mM in Section 4), which necessitated the use of adsorbed polymer brush layers for entropic stabilization.

2.1.2 Gravitational Interactions

The body force of gravity needs to be accounted for in the case of a colloid levitated over a wall. The gravitational potential energy for a colloidal particle at a height *h* above a surface is the product of its buoyant weight, *G* and the said height. The buoyant particle weight is the product of gravitational acceleration, *g* and its buoyant mass, *m*, which is in turn, a product of particle volume and the density difference between the particle and the fluid. Thus,

$$u_{grav}(h) = Gh = mgh = (4/3)\pi a^3(\rho_p - \rho_f)gh \tag{2.8}$$

where ρ_p and ρ_f are the particle and fluid densities.

2.1.3 van der Waals Interactions

In the absence of an adsorbed polymer brush, colloidal particles aggregate at high salt concentrations when they undergo Brownian collisions due to attractive van der Waals interactions. Two colloids separated by a solvent interact via electromagnetic waves, with fluctuations in local polarization in one particle inducing a correlated response in the other,[1] a phenomenon that results in van der Waals attraction. To theoretically describe the van der Waals interaction, Lifshitz continuum theory is used to compute the Hamaker constant, $A_{132}(l)$, between two half-spaces, composed of materials #1 and #2, separated by distance *l* of medium #3 as,[111,112]

$$A_{132}(l) = -\frac{3}{2}kT\sum_{n=0}^{\infty}{}'\int_{r_n}^{\infty} x\left\{\ln\left[1-\Delta_{13}\Delta_{23}e^{-x}\right]+\ln\left[1-\bar{\Delta}_{13}\bar{\Delta}_{23}e^{-x}\right]\right\}dx \tag{2.9}$$

$$\Delta_{jk} = \frac{\varepsilon_j s_k - \varepsilon_k s_j}{\varepsilon_j s_k + \varepsilon_k s_j} \qquad \bar{\Delta}_{jk} = \frac{s_k - s_j}{s_k + s_j} \qquad s_k^2 = x^2 + \left(\frac{2\xi_n l}{c}\right)^2 \left(\varepsilon_k - \varepsilon_2\right)$$

$$r_n = \frac{2l\xi_n\sqrt{\varepsilon_2}}{c} \qquad \varepsilon_k = \varepsilon_k\left(i\xi_n\right) \qquad \xi_n = \frac{nk_BT}{\hbar}$$

where $i=(-1)^{0.5}$, $\hbar$ is Planck's constant divided by 2π, c is the speed of light *in vacuum*, k is Boltzmann's constant, T is absolute temperature, and $\varepsilon_k(\omega)$ is the dielectric spectrum of material k. The prime (') next to the summation indicates that the first term (n=0) is multiplied by $\frac{1}{2}(1+2\kappa l)\exp(-2\kappa l)$. The factor of 0.5 avoids double counting while the remainder of this factor accounts for screening of the zero-frequency contribution.

The dielectric spectra for water and silica was reported by Bevan and Prieve[19] that of gold was reported by Parsegian and Weiss[113]. The van der Waals interaction between a sphere and a half space is accurately described using Derjaguin approximation as,[19,114]

$$u_{vdw}(h) = -\frac{a}{6}\int_h^\infty \frac{A_{132}(l)}{l^2} dl \tag{2.10}$$

The vdW attraction increases smoothly from the rapidly decaying far-field limit to values that are large relative to kT at small separations. For convenience, the particle-particle and particle-wall vdW interactions in this dissertation are represented by non-integer power-law decay fits to the continuum Lifshitz theory given by[19]

$$\begin{aligned} u_{vdw}^{pp}\left(h\right) &= -aA\left(h\right)^{-p} \\ u_{vdw}^{pw}\left(h\right) &= -2aA\left(h\right)^{-p} \end{aligned} \tag{2.11}$$

where a is the particle radius and A and p are fitting parameters.

2.1.4 Depletion Interactions

It is now widely known that initial observations of the flocculation of suspensions of colloids by dissolved non-adsorbing polymer were due to the so called entropic depletion effect. A similar effect is obtained when large colloids are introduced into a solution of micelles or smaller colloids. These smaller components, be they polymeric, micellar or colloidal, are referred to as depletants and depending on their concentration and size relative to the larger particles, they induce an attraction between the larger particles. The origin of this attraction comes from the exclusion of depletants from gaps lesser than their characteristic size, be it a particle-wall or particle-particle gap. Thus, when the separation between two surfaces is lesser than the diameter of a depletant colloid, the osmotic pressure of these depletants on the outside of the gap manifests itself as an attractive force between those surfaces.

The simplest theoretical description of this depletion potential was presented by Asakura and Oosawa and is called the Asakura-Oosawa (AO) model.[33] Both the particle-particle and particle-wall depletion potential can be expressed in the same general way; as a product of a fixed osmotic pressure, Π, and an excluded volume, V, which is different for particle-particle and particle-wall. Thus,

$$u_{dep}(h) = V(h)\Pi \tag{2.12}$$

For a larger colloid of radius a, and a depletant of radius L, the particle-particle AO depletion potential takes the form given below.[115]

$$u_{dep}^{pp}(h) = -\frac{4\pi}{3}(a+L)^3\left(1-\frac{3(h+2a)}{4(a+L)}+\frac{(h+2a)^3}{16(a+L)^3}\right)\Pi \tag{2.13}$$

For a larger colloid of radius *a* interacting with a wall, the AO depletion potential takes the form shown below.[37]

$$u_{dep}^{pw}(h) = -\pi\left[4L^2\left(\frac{L}{3}+a\right)-4Lah+(a-L)h^2+\frac{h^3}{3}\right]\Pi \tag{2.14}$$

In this dissertation, we treat the depletant phase as a fluid of uniform density and use a second virial coefficient to describe the behavior of the depletants and thus their osmotic pressure. The osmotic pressure, defined by the depletant number density (*n*) and second virial coefficient (B_2), is expressed as shown below.

$$\Pi = nkT\left(1+B_2 n+...\right) \tag{2.15}$$

We can also assume hard sphere behavior for the depletants, allowing the second virial coefficient to be expressed as a function of the depletant particle volume, V_p.

$$B_2 = 4V_p = (16/3)\pi L^3 \tag{2.16}$$

2.2 Total and Ensemble Total Internal Reflection Microscopy

As is evident from Equation 2.1, the repulsive and attractive contributions to the net interaction potential for a colloid levitated above a wall balance each other at a height value determined by the strength and nature of the constituent interactions. The colloid samples heights about this value on account of Brownian motion. The relative probability of a certain height being sampled is related to the potential energy of the

colloid at that position. It is therefore obvious that the most sampled height will represent the position of the minimum in the particle-wall interaction potential. Thus, by recording the height excursions of a colloid above a wall, it is possible to obtain the particle-wall potential energy. This is the underlying concept behind total internal reflection microscopy (TIRM)[116].

In TIRM, an evanescent wave generated at the interface between a wall and the liquid above it is used to track the height excursions of a single levitated colloidal particle as it scatters light when in the wave. The decay in evanescent wave intensity as a function of separation from the wall is accurately known, which allows the instantaneous position, h, of the particle to be extracted from its scattering intensity through,[79,117]

$$I(h) = I_0 \exp(-\alpha h) \tag{2.17}$$

where $I(h)$ is the scattered intensity at height h, I_0 is the intensity at particle-wall contact or zero separation, $h=0$, and α^{-1} is the evanescent wave decay length. The decay length of the evanescent wave is given by,

$$\alpha = \frac{4\pi}{\lambda}\sqrt{(n_1 \sin\theta_1)^2 - n_2^2} \tag{2.18}$$

where n_1 and n_2 are the refractive indices of the incident and transmitted media, and θ_1 is the incident angle. The probability of sampling each height above the surface is related to the potential energy at that elevation by Boltzmann's equation,[79]

$$p(h) = A\exp\left[-\frac{u(h)}{kT}\right] \tag{2.19}$$

where *p(h)* is the probability density of heights sampled by a single particle, *u(h)* is the particle-wall potential energy profile, and *A* is a normalization constant related to the total number of height observations. With sufficient statistics, *p(h)* is generated as a histogram of the heights, *n(h)*, sampled during the course of an experiment.

The potential energy relative to a reference state can determined by measuring *n(h)*, substituting for *p(h)* in Equation 2.19, and then rearranging as[118],

$$\frac{u(h)-u(h_{ref})}{kT} = \ln\left[\frac{n(h_{ref})}{n(h)}\right] \tag{2.20}$$

where h_{ref} is often chosen as h_m, which is the most probable height sampled in *n(h)*. Ensemble Total Internal Reflection Microscopy (ETIRM)[118] is an extension of TIRM and uses integrated evanescent wave scattering and video microscopy techniques to monitor the three-dimensional trajectories of many colloids near a wall. ETIRM measurements can be analyzed to yield many single-colloid surface potential energy profiles as well as an ensemble average colloid-surface potential energy profile by averaging over all colloids and surface regions sampled by the laterally diffusing colloids in much the same way as TRIM. The measured potential energy profile is only due to the conservative forces and is unaffected by dissipative hydrodynamic forces.

2.3 Energy Landscapes from 2D Colloid Distributions

All lateral diffusion experiments reported in this dissertation were performed using sub-monolayer concentrations of 2.34μm SiO_2 colloids in water. Due to their high buoyant weight, these particles experience height excursions that are far lesser than their radius. This results in the silica colloids being confined by gravity to a two-dimensional plane above a homogeneous substrate, thus permitting treatment of this system as purely two-dimensional. Consider a two-dimensional fluid composed of *N* silica 2.34μm SiO_2 colloidal particles in equilibrium above a homogeneous wall. Due to the fact that the particle-wall interaction is homogeneous, the density, ρ, is homogeneous in the two dimensional plane parallel to the wall containing the colloids. In this case the probability of finding a colloid in a given position, $\rho(x, y)$, is the same for all (x, y) positions.

For a similar fluid adjacent to a chemically or physically patterned substrate, interactions of colloidal particles with the underlying wall surface will cause lateral density variations. Such density variations can be described in two dimensional colloidal fluids approaching infinite dilution by Boltzmann's equation as,

$$\frac{u(x,y)-u_{ref}(x,y)}{kT} = -\ln\left[\rho(x,y)/\rho_{ref}(x,y)\right] \tag{2.21}$$

where $u(x, y)$ is the local dependent interaction potential between single colloids and the underlying substrate, which can be referred to as a potential energy landscape. In the experiments with physical patterns reported in this dissertation, the surface is clearly three-dimensional, but the depth of the physical features are small compared to the

radius of the colloids and that coupled with the small height excursions of the particles and the submonolayer coverage allows us to treat the inhomogeneous fluid as two-dimensional. As the concentration of colloidal particles increases, multi-particle packing effects and many-body interactions become important and the Boltzmann inversion of concentrated $\rho(x, y)$ will yield a position dependent potential of mean force, $w(x, y)$, which we refer to as a free energy landscape in this dissertation. This effectively captures the average interaction between a single colloid and each surface location as mediated by all nearby and intervening colloids.

In these concentrated fluids, we attempt to obtain $u(x, y)$ from the experimentally recorded $\rho(x, y)$. The goal is to extract the interaction of single colloids with the underlying physically patterned surface, which we refer to as a potential energy landscape, $u(x, y)$. To accurately recover $u(x, y)$ by accounting for many-particle effects, we run forward two-dimensional Monte Carlo (MC) simulations for known particle-particle potentials and estimates of the physical feature profile (depth, shape and width). The physical feature profile that yields a $w(x, y)$ that agrees closely with the experimentally obtained $w(x, y)$ is taken to be the accurate description of the physical feature or $u(x, y)$.

2.4 Self Diffusion in Sub-Monolayer Colloidal Fluids

The diffusion coefficient of an isolated colloidal particle undergoing three-dimensional diffusion far from any boundaries is given by the Stokes-Einstein equation as,

$$D_0 = \frac{kT}{6\pi\mu a} \tag{2.22}$$

For a single colloid near a planar surface, particle-surface hydrodynamic interactions hinder the particle's diffusion lateral to the surface as given by,

$$D_{\|}(h) = D_0 f_{\|}(h) \tag{2.23}$$

where the function $f_{\|}(h)$ is conveniently represented by a rational expression fit to the exact solutions (with less than ±0.001 relative error) as,[119,120] For a single colloid near a planar surface, particle-surface hydrodynamic interactions hinder the particle's diffusion lateral to the surface as given by,

$$f_{\|}(h) = \frac{12420\gamma(h)^2 + 5654\gamma(h) + 100}{12420\gamma(h)^2 + 12233\gamma(h) + 431} \tag{2.24}$$

where $\gamma(h)=(h-a)/a$. In dilute sub-monolayer colloidal fluids, particles experience lateral motion relative to underlying surfaces within normal potential energy wells and without particle-particle hydrodynamic interactions. The ensemble average lateral, $D_{\|}$, diffusion coefficient in such dilute sub-monolayer colloidal fluids are given by,[121]

$$D_{\parallel} = \frac{\int D_{\parallel}(h)\, p(h) dh}{\int p(h) dh} \tag{2.25}$$

where $p(h)$ is the particle height distribution related to $u_{\mathrm{pw}}(h)$ in Equation 2.1 by Boltzmann's equation given as,[118,122]

$$p(h) = p_{ref} \exp\left[-u_{pw}(h)/k_B T\right] \tag{2.26}$$

where p_{ref} is the probability of a reference height (that also determines the reference potential, usually the most probable height). The integral of $p(h)$ over all h is not necessarily unity so that Equation 2.25 is normalized by the integral of $p(h)$.

For concentrated sub-monolayer colloidal fluids, particle self diffusion is affected by many-particle packing effects and both conservative and dissipative forces acting between particles and surfaces. At short times, particles diffuse over distances small compared to their radius, which depends only on hydrodynamic interactions with surrounding particles in a given instantaneous configuration. Such short time self diffusion lateral to the surface is given by,[123]

$$D_{S,\parallel}^{S} = \frac{1}{N_p} \sum_{i=1}^{N_p} \frac{D_i^{xx} + D_i^{yy}}{2} \tag{2.27}$$

where $\mathbf{D}$ is the N_p particle diffusion tensor given by,[124]

$$\mathbf{D} = k_B T \mathbf{R}^{-1} \tag{2.28}$$

where $\mathbf{R}$ is a $3N_p \times 3N_p$ tensor depending on the instantaneous particle position vector, $\mathbf{r}$, which is a vector of dimension $3N_p$ in bulk colloidal dispersions. In interfacial colloid

fluids, **R** also depends on the particle positions relative to a wall surface. To incorporate wall boundary conditions, the wall is discretized into a regular array of N_w fixed spheres of radius a.[125,126] By including both free and fixed wall particles, **R** is a $3N\times3N$ tensor with $N=N_p+N_w$ particles. To accurately compute both far-field, multi-body and near-field hydrodynamic forces, **R** is calculated using the method of Brady as,[124]

$$\mathbf{R} = \mathbf{R}^{\infty} + \mathbf{R}_{2B} - \mathbf{R}_{2B}^{\infty} \tag{2.29}$$

where $\mathbf{R}^{\infty}$ is the many-body, far-field resistance tensor, $\mathbf{R}_{2B}$ is the exact two-body resistance tensor, and $\mathbf{R}_{2B}{}^{\infty}$ is the two-body, far-field resistance tensor. $\mathbf{R}^{\infty}$ is obtained by inverting the far-field mobility tensor, $\mathbf{M}^{\infty}$, To accurately compute both far-field, multi-body and near-field hydrodynamic forces, **R** is calculated using the method of Brady as,[124]

$$\mathbf{R}^{\infty} = \left(\mathbf{M}^{\infty}\right)^{-1} \tag{2.30}$$

where $\mathbf{M}^{\infty}$ is calculated using the Ewald-summed Rotne-Prager tensor derived by Beenakker.[127]

In this dissertation, short-time, D_S^S, self-diffusivities for the MC simulated equilibrium configurations are computed from the trace of the diffusion tensor, **D**, given in Equation 2.28.

3. EXPERIMENTAL METHODS

3.1 Materials and Equipment

3.1.1 Generic Chemicals

The following chemicals were purchased and used without further purification:

- Sodium chloride, hydrogen peroxide, sulfuric acid, acetone, methanol and toluene (Sigma-Aldrich)
- Magnesium sulfate heptahydrate (Alfa Aesar)
- Sylgard polydimethylsiloxane (Dow Corning)
- Pluronic F108 (BASF Corp.)

3.1.2 Wall Surfaces and Particles

- Nominal 2.34μm silica colloids (ρ_p=1.96 g/ml) were purchased from Bangs Laboratories (Fishers, IN)
- Nominal 1.58μm silica colloids (ρ_p=2.18 g/ml) were purchased from Duke Scientific (Fremont, CA)
- Nominal 110nm polystyrene (PS) colloids were purchased from Molecular Probes (Eugene, OR)
- 22×22, 18×18, 24×50mm coverslips and 24×75mm microscope slides (Gold Seal, Corning, NY)

3.1.3 Silanes and Thiols

- >90% octadecyltrichlorosilane (OTS) and 1-octadecanol (1-oct) were purchased from Sigma-Aldrich while >95% 1-hexadecanethiol (HDT) was purchased from Alfa Aesar.

3.1.4 Photolithography Chemicals

- SU-8 2002 (MicroChem, Newton, MA), S1827 and S1805 (Shipley)
- MF 319 and SU-8 developers; HDMS adhesion promoter

3.1.5 Equipment and Instrumentation

- 15mW 633 (red) and 543nm (green) lasers (Melles Griot, Carlsbad CA)
- 12-bit CCD camera (max 43fps) from Hamamatsu (Japan)
- Axioplan 2 and Axiovert 135 optical microscopes (Zeiss, Germany)
- 100 (oil N.A.=1.4), 63 (air N.A.=0.6) and 40× (air N.A.=0.6) objectives (Olympus)
- ZetaPALS particle analyzer (Brookhaven Instruments)
- Q4000 mask aligner (Quintel); SCS P6204 spin coater; reactive ion etcher (March Plasma Systems, CS-1701); metal evaporator (306, BOC Edwards), Accument AR20 pH and conductivity meter; Branson 1510 ultrasonicator.

3.1.6 Miscellaneous

- Index matching oil (n=1.518, Cargille, Cedar Grove, NJ), 68° dovetail prism (Reyard Corp., CA), 99.99% Au shot (Premion, MA), Viton O-rings (McMaster

Carr, CA), vacuum grease (Dow Corning) and Loctite quick set epoxy (Henkel Consumer Adhesives, Avon, OH)

3.1.7 Ionic Solutions

Deionized (DI) water from an in-house purification system with a conductivity value of ~1 μS cm^{-1} was used in the preparation of all aqueous ionic solutions used in the studies presented in this dissertation. NaCl and $MgSO_4$ solutions with ionic strengths of ≥0.4M were used in the specific ion effect studies reported in Section 4 while 0.15mM NaCl solutions were used in Sections 5 and 6. The pH of the electrolyte solutions was maintained well above the isoelectric point of the colloidal particles to ensure a negative surface charge.

3.1.8 Gold Vapor Deposition

The gold coated substrates used in Section 4 were prepared by evaporating 5nm of chromium and 5nm of gold onto the silica slides ~0.1nm/s using a metal evaporator chamber (306, BOC Edwards).

3.1.9 Cleaning Procedures

Glass surfaces were immersed in a piranha solution (3:1 mixture of 99% H_2SO_4 to 35% H_2O_2) for ~1hr to remove organic contaminants and increase surface charge. This was followed by washing with DI water and immersion in 0.1M KOH to further enhance the surface charge. The last step involved thorough washing with DI water and

drying with high purity nitrogen. For the gold substrates used in Section 4, the KOH step was skipped.

3.1.10 Surface Modification

The hydrophobic glass and gold sides used in Section 4 were produced by solution phase deposition of self-assembled monolayers (SAMs).[128] Solution phase self-assembly was performed at a molar concentration of 5mM for all silanes and thiols. Care was taken to ensure all glassware and substrates were dry. All solution phase bonding was carried out in a desiccator jar for 10hr. Following the formation of SAMs, slides were removed amd immediately rinsed twice with the same solvent they were immersed in during SAM formation (typically toluene for silanes and 200-proof ethanol of thiols). The hydrophobic slides were stored in toluene before use to reduce dust adsorption. All slides were used less than two days after preparation. The surface of the 1.58μm silica colloids was made hydrophobic by modification with 1-octadacanol.[129]

3.1.11 Physisorption of Macromolecules

F108 Pluronic was adsorbed to hydrophobic glass and gold slides as well as the 1-octadecanol-modified 1.58μm silica colloids used in Section 4. Substrate adsorption was carried out for ~5hrs by pipetting a drop of 1000ppm F108/water onto the slides. Colloid surface adsorption was performed by shaking the 1-octadecanol-modified 1.58μm silica colloids in a 1000ppm F108/water solution for ~24hrs.

3.1.12 PNIPAM Particle Synthesis

The PNIPAM gel particles used in Sections 5 and 6 were synthesized using free radical polymerization of N-isopropylacrylamide (NIPAM) and N,N'-methylene-bis-acrylamide (MBA). A mixture of 0.950 g portion of the NIPAM monomer, 0.016 g of MBA monomer cross-linker, 0.028 g of sodium dodecyl sulfate (SDS) surfactant, were dissolved in 55mL distilled water in a three-neck flask. The solution was stirred for ~2hrs under nitrogen purge in an oil bath at 87°C. This was followed by the addition of a solution of 0.040 g potassium persulfate (KPS) in 6mL degassed distilled water to initiate the polymerization. The reaction was carried out at 87°C oil bath for ~4hrs.

The PNIPAM particles thus obtained were purified via dialysis against DI water for two weeks at room temperature, with the DI water being changed twice per day. The dialysis membrane had a molecular weight cutoff of 10,000. The particles were then concentrated by centrifugation at 30,000 rpm for 2 hours at 34°C followed by re-dispersion in DI water.[69]

3.1.13 Assembly of Experimental Cells

All experiments presented in this dissertation involved heating of the sample cell. Batch experimental cells were assembled by trapping a drop of sample solution between two glass substrates and sealing the edges with quick-setting epoxy. The volume of solution used (~15μL) ensured a gap width of ~100μm and resulted in a system where gap width did not confine any of the particles used in this report. The sample cell was placed on a dove prism which provided a fair degree of thermal inertia and improved

temperature stability at the set point. Temperature control was implemented by using Kapton heaters, a CN77332 controller and a thermocouple (Omega Engineering Inc., Stamford, CT) affixed to the top coverslip near the area of interest.

3.2 Microfabrication

3.2.1 Patterning Physical Patterns on Glass Substrates

The physically patterned glass substrates used in Section 6 were prepared using conventional photolithographic techniques (Figure 3.1) with all the microfabrication steps conducted in a class 1000 clean room. Piranha cleaned glass microscope slides were baked at 200 ºC for 5 minutes in a contact hotplate to dehydrate the surface. A ~1μm thick SU-8 2002 negative photoresist layer was spin-coated onto the slides at 4000 rpm for 30 seconds. The photoresist coated slides were then soft baked on a hotplate at 95 ºC for 2min followed by exposure to ultraviolet (UV) light through a patterned mask for 20 seconds.

Following exposure, the substrates were post-baked for 1min at 65 ºC and 1 min at 95 ºC to selectively cross-link the exposed portions of the photoresist film. The substrates were then immersed in SU-8 developer for 60s. The developed photoresist pattern was placed in a reactive ion etcher and exposed to 0.3 cm^3/s oxygen plasma for 30s at 200 W to get rid of any residual photoresist and developer. A drop of a HF:DI water mixture (1:1) was place on the photoresist patterned slide for 1-4s which results in a range of feature depths (Figure 3.2). Slides were then thoroughly rinsed with DI water to cease the etching process.

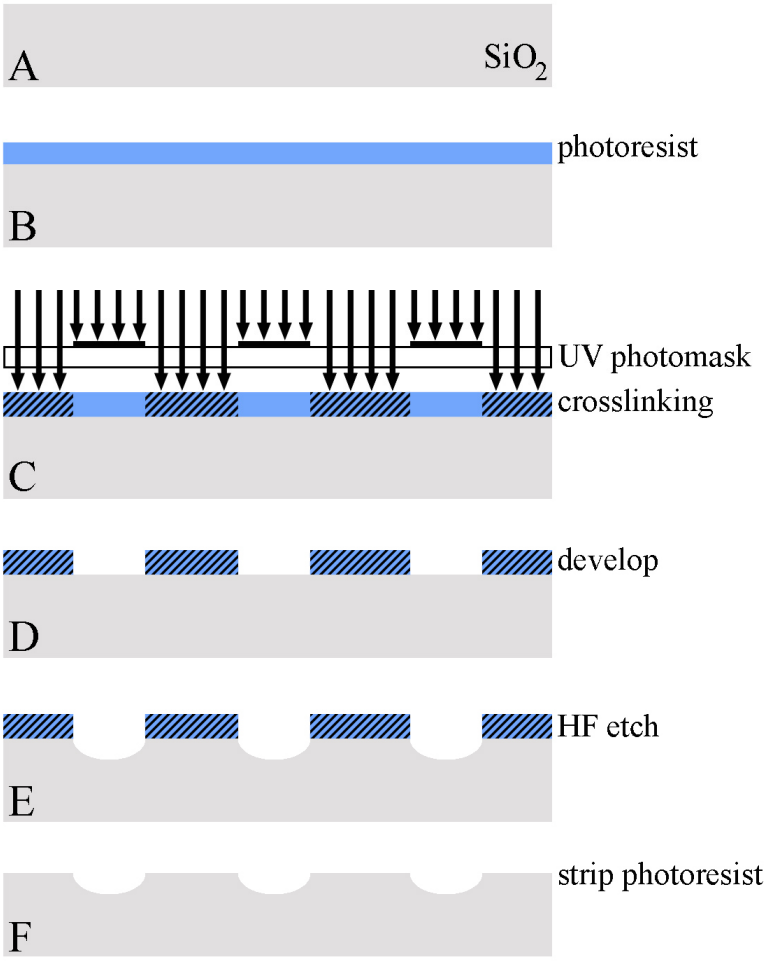

Figure 3.1. Schematic representation of the general microfabrication steps used to pattern physical features on a glass substrate.

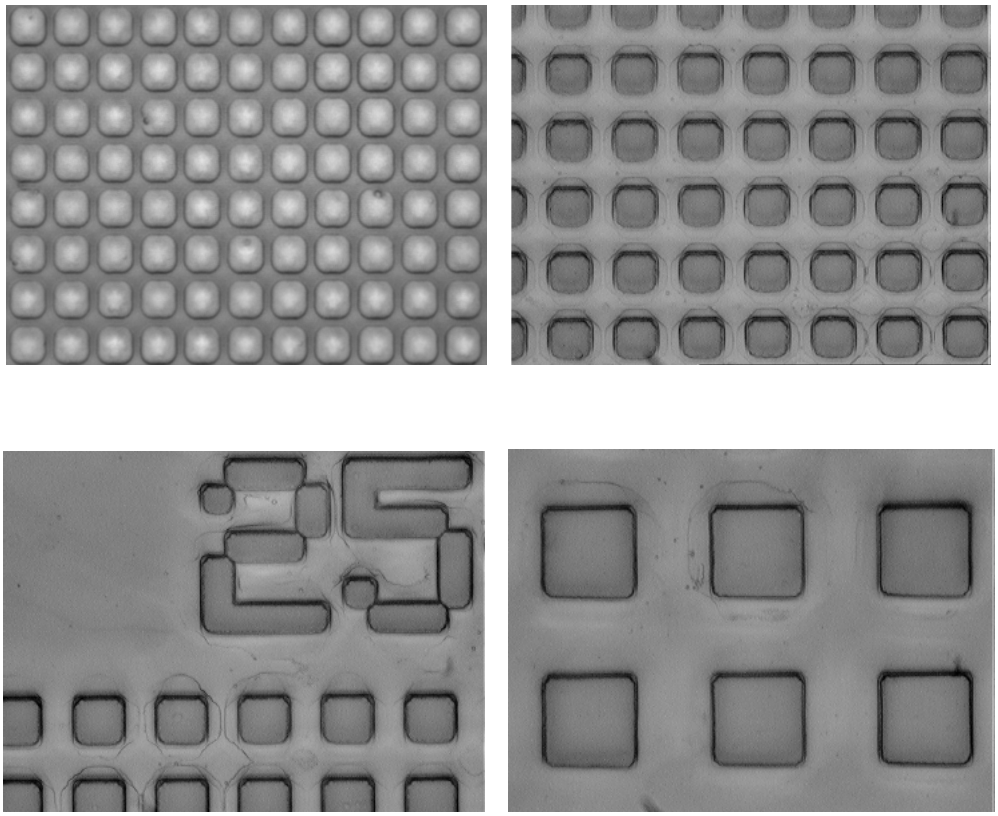

Figure 3.2. (Clockwise from top left) CCD images of physically patterned glass substrates containing square arrays of varying sizes (a) 8 μm x 8 μm, (b) 20 μm x 20 μm, (c) 50 μm x 50 μm, and (d) 25 μm x 25 μm.

3.3 Microscopy Techniques

3.3.1 Ensemble Total Internal Reflection Microscopy (ETIRM)

Figure 3.3 shows a schematic representation of a typical ETIRM experimental setup. A batch cell, optically coupled to a 68° dovetail prism with the aid of index matching oil, is mounted on a three point leveling stage. In particle-wall potential energy measurements, a 40X objective (NA=0.65) and a 1.6X magnifying lens were

used in conjunction with a 12 bit CCD camera operated at 4x binning (128μm x 97μm images were obtained with 336x256 resolution to produce ~379nm pixels). $6.0x10^4$ images were recorded at a 27 frames/s framerate. A 15 mW, 632.8 nm Helium-Neon laser was used to generate an evanescent wave with a decay length of 113.67 nm.

To track each particle's three dimensional trajectory, typical image analysis algorithms[104] coded in Fortran were used to locate center coordinates (~10 nm) on each scattering pattern. Each particle's scattering intensity was integrated to obtain the height of the center above the bottom surface, z (~1 nm) (see Section 2 and Fig. 3.3). Figure 3.4 shows representative results from a typical ETIRM experiment in which the ensemble particle-wall interaction potential was measured for 2.34 μm silica colloids interacting with a glass substrate in DI water. An average particle size of 2.27 μm and a Debye screening length of κ^{-1}=89nm, was obtained from the theoretical fits to the measured potential energy profile.

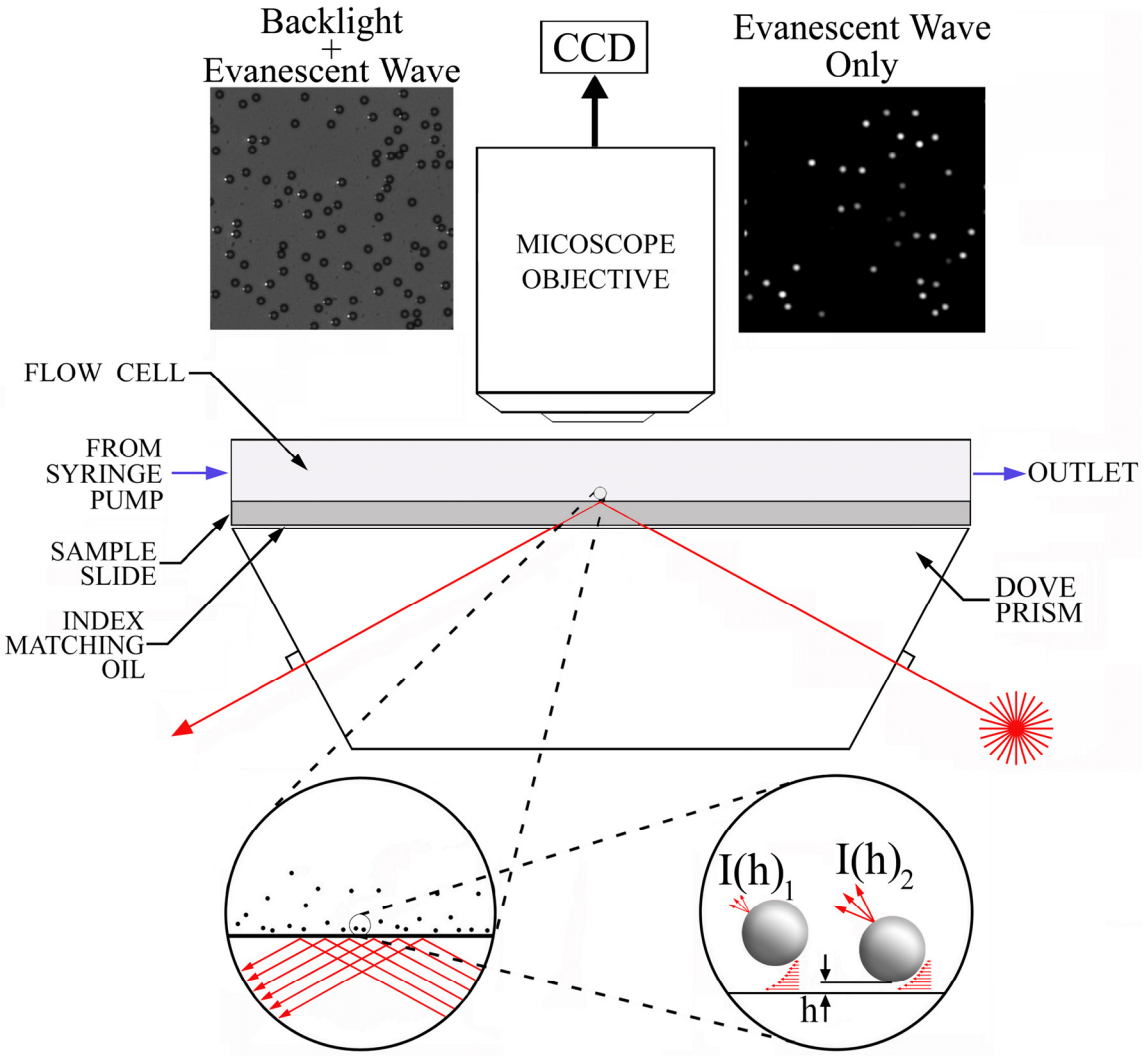

Figure 3.3. Schematic illustration of the ETIRM apparatus with HeNe laser, prism, batch cell, microscope, CCD camera, and data acquisition PC. Insets shows schematic representation of levitated particle scattering evanescent wave with intensity, *I(h)*, as a function of particle-wall surface separation, *h*. CCD image from top view of levitated particles scattering evanescent wave (white spots) with transmitted light illuminating particles (dark rings) is also shown.

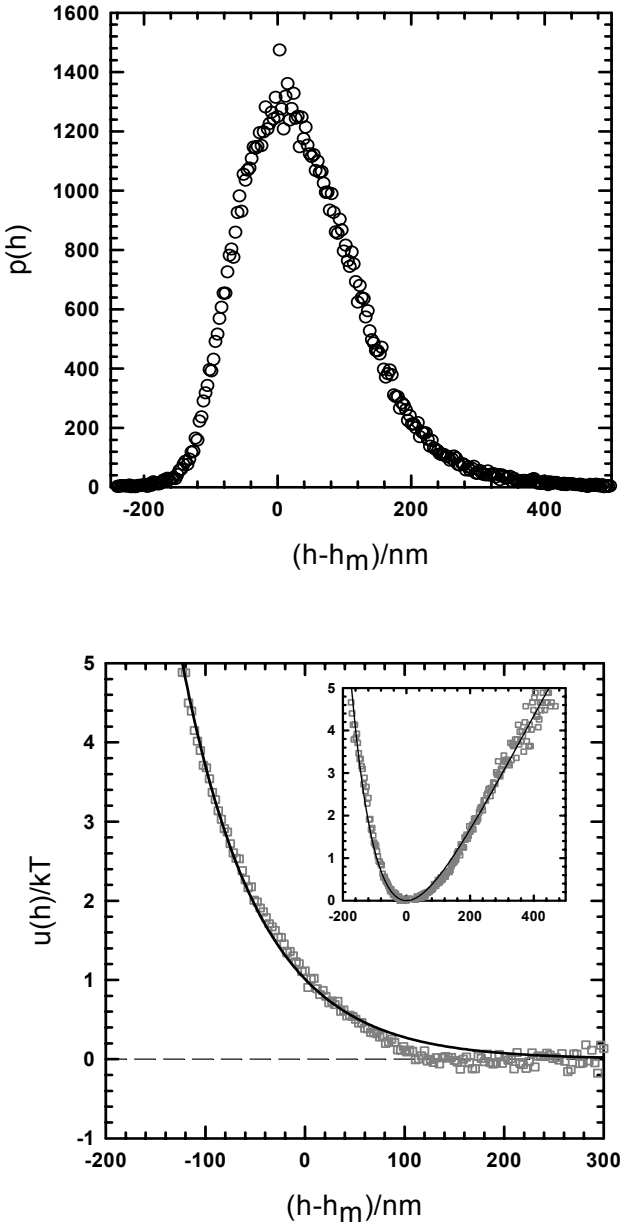

Figure 3.4. TIRM measurements of particle-wall interaction potential between 2.34 μm silica colloids in DI water interacting with a glass substrate. (a) Ensemble averaged particle-wall distribution function. (b) Ensemble averaged particle-wall potentials determined from the probability density function in (a) using Boltzmann's equation (Eq. (2.1)). Solid lines (—) are theoretical DLVO fits to the measured potential.

3.3.2 Video Microscopy (VM)

As with the ETIRM experiments, batch cells were placed on a three point levelling stage and adjusted for particle migration prior to the experiment. Bright field digital images were obtained using a 63X objective and a 1.6X magnifying lens in conjunction with a 12 bit CCD camera operated with 2x binning. A sequence of equilibrium particle configurations was recorded at 18 frames/s, with total observation times depending on the nature of the experiment. 115μm x 77μm images were obtained with 608 x 404 resolution to produce ~190nm pixels, which allowed centroid location to within ~95nm using typical particle tracking algorithms.[104] The details of the image analysis algorithm used are not repeated in this dissertation for the sake of redundancy. All image analysis was performed using single-processor PC's and multi-page TIFF files containing up to 10^5 608 x 404 separate images.

4. EQUIVALENT TEMPERATURE AND SPECIFIC ION EFFECTS IN MACROMOLECULE-COATED COLLOID INTERACTIONS*

4.1. Synopsis

In this section, we report the use of ensemble total internal refection microscopy (ETRIM) to measure reversible temperature and specific ion mediated interaction potentials between macromolecule coated colloids and surfaces. Equilibrium interaction potentials were measured between PEO-PPO-PEO block copolymers adsorbed to

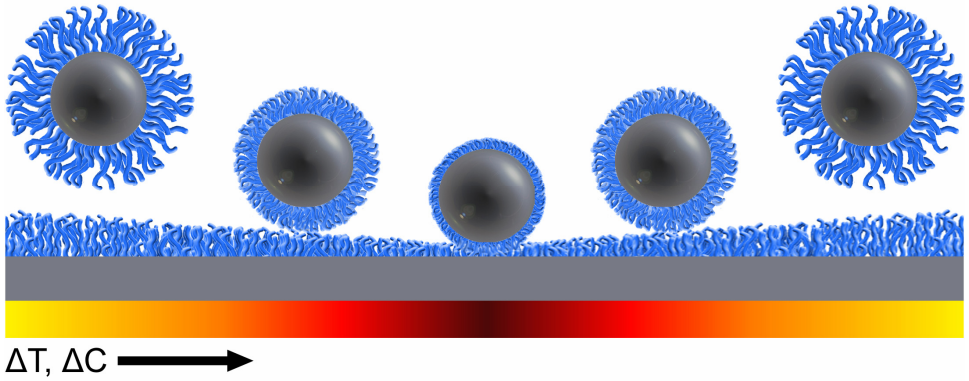

Figure 4.1. A conceptual illustration showing solvent quality controlled levitation and deposition of a macromolecule coated silica colloid interacting with a macromolecule coated silica substrate. Yellow indicates conditions of temperature and salt concentration that yield thick brush layers (A) whereas Red signifies collapsed layers (B). The color bar signifies an A-B-A change in solvent conditions.

* Reprinted with permission from "Equivalent Temperature and Specific Ion Effects in Macromolecule-Coated Colloid Interactions" by Gregory E. Fernandes and Michael A. Bevan, 2007. *Langmuir*, **23** (3), 1500-1506, Copyright (c) 2006 by American Chemical Society.

hydrophobically modified silica colloids and glass or gold planar surfaces. We investigated a range of solvent conditions that included temperatures from 20-47°C and $MgSO_4$ concentrations from 0.2-0.5M. The solvent quality mediated copolymer layer collapse inferred by comparing measured potentials and the predicted van der Waals attraction, including effects of the adsorbed copolymer and surface roughness, displayed good agreement with expected limits based on the PEO block contour length and the bulk PEO density. Herein, we report an equivalence of increasing temperature and increasing $MgSO_4$ concentration when mediating layer interactions and dimensions. This claim is supported by the fact that it is possible to superimpose all PEO layer collapse measurements reported in this dissertation onto a single universal curve via a transformed temperature scale relative to a reference temperature in each case. Accurate knowledge of nanometer and *kT* scale interactions of copolymer coated colloids as a function of temperature and $MgSO_4$ concentration provides the ability to reversibly control the stability, phase behavior, and self-assembly of such particles.

4.2. Introduction

By changing temperature or the concentration of inorganic electrolyte co-solutes, it is possible to alter the solubility, phase behavior, and solution conformation of nonionic and polyelectrolyte macromolecules in aqueous media. Although polymer solution theories successfully capture many aspects of non-aqueous macromolecule solutions,[130,131] significant limitations have been encountered in the description of aqueous macromolecular solution properties such as reduced solubilities at elevated

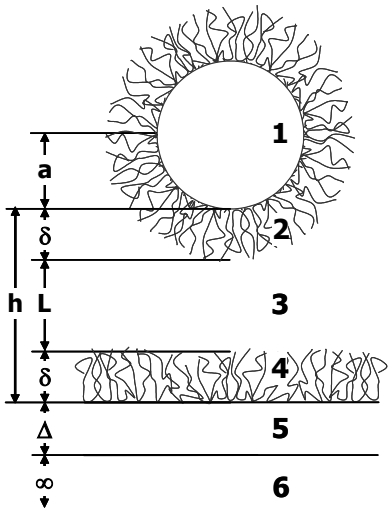

Figure 4.2. Schematic of a macromolecule stabilized colloid interacting with a planar surface (not drawn to scale). Variables define relevant dimensions, and numbers define materials.

temperatures (i.e. lower critical solution temperature behavior)[132,133] and perhaps more famously, the role of specific ions in a wide range of phenomena, particularly involving biological macromolecules (e.g. proteins, nucleic acids, carbohydrates).[72,134,135] A lack of fundamental understanding of the origin of temperature and specific ion mediated interactions places serious limitations on the ability to interpret and predict numerous natural and technologically important phenomena.

A basic example where temperature and specific ion mediated interactions are important, but remain poorly understood, is in the case of solvated macromolecules adsorbed to colloids dispersed in aqueous media. Macromolecular stabilization of colloids[24] is essential in high ionic strength aqueous media where electrostatic interactions are highly screened, and as a result, is an important mechanism in

biomedical[136] and environmentally benign industrial applications employing aqueous dispersions.[137] The ability to reversibly tune kT scale attraction between macromolecule coated colloids makes such particles desirable as model systems for investigating the statistical mechanics of phase behavior[2,102] and as basic components in closely related problems involving equilibrium colloidal self-assembly. However, beyond the classic early work of Napper,[24] relatively little work has attempted to directly measure and understand how combined temperature and specific ion effects mediate the net pair potential of macromolecule coated colloids.[31]

Herein, we use ensemble total internal reflection microscopy (ETIRM)[118,122] to directly measure the evolution of temperature and specific ion dependent potential energy profiles between many single colloids and a planar surface bearing adsorbed PEO-PPO-PEO block copolymers (see Figure 4.2). ETIRM uses integrated evanescent wave scattering and video microscopy techniques to monitor the three dimensional center coordinates of colloids near planar surfaces. Such measurements can be analyzed to yield many single colloid-surface potential energy profiles as well as an ensemble average colloid-surface potential energy profile by averaging over all colloids and surface regions sampled by laterally diffusing colloids. Here, we report ensemble average potential energy profiles to provide statistically significant measurements of the interactions between macromolecule coated colloids and surfaces.

Potential energy profiles are measured at different $MgSO_4$ concentrations (C=0.2-0.5M) as a function of temperature (T=20-47°C) to understand interactions in better than theta conditions.[25] A continuous, reversible PEO layer collapse is inferred

from the measured potentials via fits to theoretical van der Waals potentials that include both adsorbed layer and core colloid contributions.[30,31,138] By plotting temperature dependent layer collapses at each $MgSO_4$ concentration on a modified scale relative to a reference temperature in each case, a universal PEO layer collapse curve is obtained that indicates an equivalence of increasing temperature and increasing $MgSO_4$ concentration in controlling layer interactions and dimensions. By quantitatively connecting nanometer and kT scale ETIRM measured potentials to rigorous van der Waals predictions and an inferred PEO layer collapse, this work demonstrates the ability to sensitively measure and reversibly manipulate temperature and specific ion mediated attraction between macromolecule coated colloids. Accurate knowledge of nanometer and kT scale interactions of copolymer coated colloids as a function of temperature and $MgSO_4$ concentration provides the ability to reversibly control the stability, phase behavior, and self-assembly of such particles.

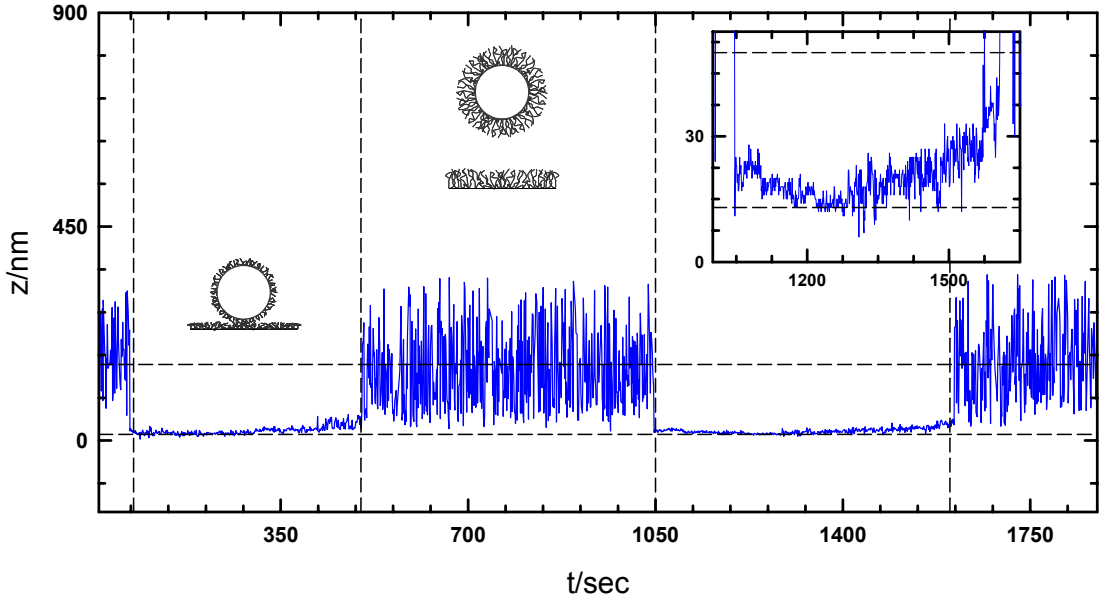

Figure 4.3. Height excursions corresponding to reversible, solvent quality dependent levitation and deposition of a single 1.58μm SiO_2 colloid on a glass slide with PEO-PPO-PEO block copolymers adsorbed to both surfaces. In 0.4M $MgSO_4$ aqueous media, the single colloid is levitated at T=20°C and deposited at T=32°C. The inset shows rapid deposition and re-levitation with changes in solvent quality. Horizontal lines (---) indicate average surface separations for deposited and levitated conditions, and vertical lines (---) indicate temperature changes.

4.3. Results and Discussion

4.3.1 Temperature and Specific Ion Mediated Reversible Deposition

Figure 4.2 schematically depicts the interaction of a polymer coated colloid and a planar surface with relevant dimensions and materials labeled by variables and numbers. In this work, temperature (T=20-47°C) and $MgSO_4$ (C=0.2-0.5M) mediated potential energy profiles and deposition measurements are reported for PEO-PPO-PEO block

copolymers adsorbed to alkyl modified 1.58μm silica colloids and alkyl modified glass or gold coated glass surfaces. The copolymer is abbreviated as PEO based on the importance of the solvent quality dependent properties of the PEO block compared to the insoluble PPO block.[132] The divalent $MgSO_4$ concentration exceeds 0.2M in all experiments so that electrostatic interactions are negligible at separations greater than the ~ 1nm Debye screening lengths (κ^{-1}=0.3-0.2nm). The only appreciable interactions to consider in this work (apart from gravity) are macromolecular interactions due to interpenetration and compression of PEO layers on adjacent surfaces[24,139] and van der Waals attraction (only $u_{steric}(h)$ and $u_{vdw}(h)$ in Equation 2.1).[140]

Figure 4.3 demonstrates the thermodynamically reversible nature of the solvent quality dependent interactions and can be used to qualitatively describe different contributions to colloid-surface interactions at different solvent conditions. While results in Figure 4.3 are for the specific case of alternating between T=20°C and T=32°C with C=0.4M $MgSO_4$, this behavior was observed for all temperature and $MgSO_4$ conditions investigated in this work. For the initial conditions in Figure 4.3, the single colloid experiences large height excursions within a potential energy well determined by a short range macromolecular repulsion and a longer range buoyant gravitational potential. As solvent quality is diminished, the single colloid rapidly experiences (~30s) much smaller height excursions within a deep (relative to kT) and narrow energy well determined by macromolecular repulsion and van der Waals attraction. By reverting to the initially better solvent conditions, the colloid rapidly responds (~30s) by again experiencing large height excursions indicative of robust levitation (and bulk dispersion

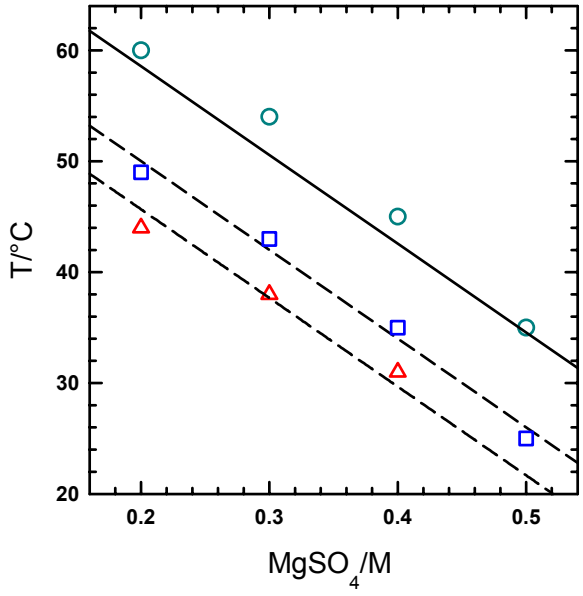

Figure 4.4. Summary of CDT and CFT as a function of $MgSO_4$ concentration. SLS CFTs of PEO copolymer coated 120nm PS colloids shown by circles (O), and ETIRM CDTs of PEO copolymer coated 1.58μm silica colloids for deposition on bare glass (□) and 5nm gold coated glass (Δ). The solid line (—) is a fit to the CFT data of PEO grafted on 104nm latex colloids.[23] The dashed lines are best fits to the CDT data with the same slopes as the CFT line.

stability).

The reversible levitation-deposition behavior observed in Figure 4.3 and all experiments in this paper are in contrast to the irreversible behavior observed in a previous TIRM study using the same PEO copolymers with larger colloids and only temperature mediated interactions.[29] An important difference in this work is the greater contribution of the PEO layers to the net interaction potential compared to contributions from smaller core colloids due to relative size effects.[141] Changes to interactions on the order of *kT* due to temperature and specific ion dependent properties of solvated PEO

layers will be demonstrated in the following measurements via the evolution of attraction in potential energy profiles and deposition measurements.

Figure 4.4 shows results in the limit where the net temperature and $MgSO_4$ dependent attraction is strong compared to kT, which produces deposition of colloids on surfaces (and bulk dispersion aggregation). The solid line in Figure 4.4 is the critical flocculation temperature (CFT) of 100nm latex colloids with grafted 800kDa PEO fit to light scattering results of Napper,[23] and the circles are our light scattering CFT measurements of 110nm latex colloids with the adsorbed PEO copolymer (with 5kDa PEO blocks). The similarity of both CFT measurements to the $MgSO_4$ dependent θ temperature of bulk PEO homopolymer solutions indicates that both grafted and PEO layers control colloid stability via intermolecular interactions that favor interpenetration of chains. This indicates that core particle van der Waals attraction does not contribute to the net interaction for ~100 nm latex colloids with grafted 800kDa or adsorbed 5kDa PEO layers for the conditions investigated in Figure 3.[141]

The squares and triangles in Figure 4.4 correspond to critical deposition temperatures (CDT) for PEO polymer coated 1.58μm silica colloids on PEO polymer coated glass and gold surfaces as shown in the example in Figure 4.3. The CDT is determined experimentally as the lowest temperature for which colloids become trapped in deep and narrow van der Waals wells (that do not allow sampling of long range, linear gravitational potentials beyond the range of colloid-surface interactions). For these much larger colloids, the core colloid van der Waals contributes to the net attraction to produce CDTs less than the CFT for 100 nm latex colloids due to size scaling effects

(i.e. Derjaguin approximation).[141] The increased core particle contribution arises due to the solvent quality dependent dimensional collapse of the PEO layers, which allows the core colloid and substrate surfaces to approach each other within separations where their van der Waals attraction becomes appreciable. This mechanism is analogous to increased screening of repulsive electrostatic interactions between charged colloids with increasing ionic strength to expose van der Waals attraction. The onset of significant van der Waals attraction before the PEO layers experience favorable interpenetration, which is shown by the CFT data in Figure 4.4, instead causes lower CDTs for larger colloids. Likewise, the increased van der Waals attraction due to the 5nm gold film further reduces the CDT in Figure 4.4.

In the limit where colloids are deposited on the surface in Figure 4.4, the potential well is deep relative to kT and exceedingly narrow due to the strong macromolecular repulsion and van der Waals attraction that confine colloids against the wall surface. In the following section, we use ETIRM to measure the evolution of potential energy profiles (i.e. diminishing range of repulsion and increasing attraction) as a function of changing solvent conditions due to the combined effects of changing temperature and specific ion concentrations. This allows for quantitative interpretation of the relative contributions of the PEO layer and core colloid to the net interaction potential, which is used to quantify the solvent quality dependent PEO layer collapse.

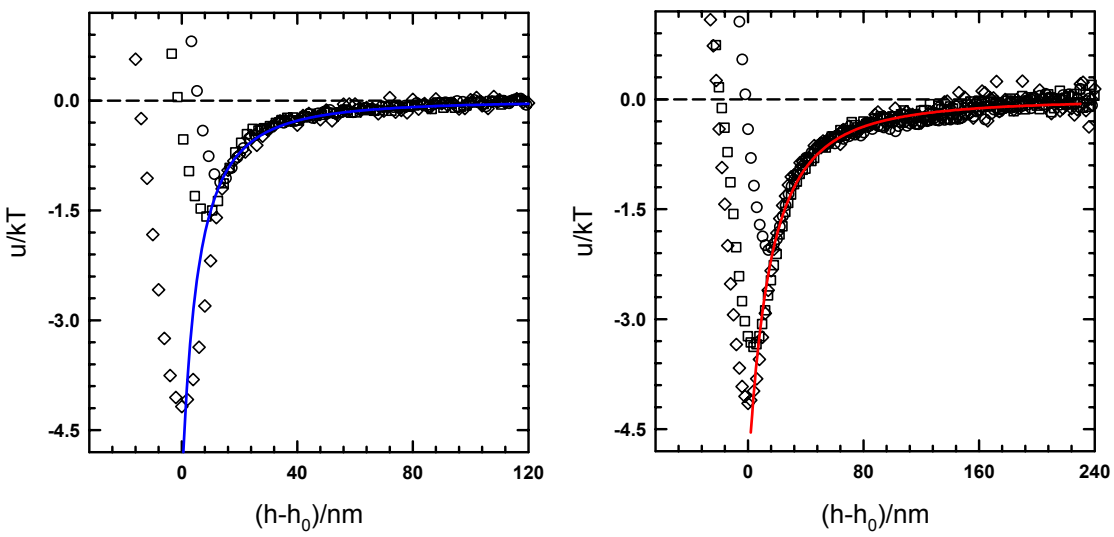

(a) (b)

Figure 4.5. Ensemble average potential energy profiles for PEO copolymer coated 1.58μm SiO_2 colloids and (a) a glass surface at T=31(O), 32(□), 33(Δ)°C in 0.4M $MgSO_4$, and (b) a 5nm gold coated glass surface at T=26(O), 34 (□), 36(Δ)°C in 0.4M $MgSO_4$. Solid curves (—) are theoretical van der Waals predictions fit to the data. Contact (h_0=0) is defined at the deepest potential energy minimum.

4.3.2 Temperature and Specific Ion Mediated Potentials

Figure 4.5 shows several representative potential energy profiles measured with ETIRM for varying temperatures at fixed $MgSO_4$ concentrations. A total of 7 sets of evolving potential energy profile measurements (5 more in addition to 2 sets shown in Figure 4.5) were obtained for the better than theta conditions in Figure 4.4 corresponding to the 7 terminal CDT points. Figure 4.5a shows ensemble average potential energy profiles for the glass surface for T=31, 32, 33°C and C=0.4M $MgSO_4$, and Figure 4.5b

shows similar results except for the presence of a 5nm gold film on the glass surface and conditions of T=26, 34, 36°C and C=0.3M $MgSO_4$. The linear gravitational potentials have been subtracted in each case to leave only the macromolecular repulsion and van der Waals attraction. The potentials are reported relative to the minimum of the profile with the deepest minimum in each case.

As shown in Figure 4.5, the range of repulsion decreases and the depth of the attractive minima increases for both $MgSO_4$ concentrations with increasing temperature. It is evident from the profiles that all colloids remain levitated since they experience excursions beyond the range of the van der Waals attraction in both cases (which has been truncated to focus on separations in the vicinity of the minima). For the next higher temperature in the two cases shown in Figure 4.5 (36 and 38°C), the colloids are deposited on the wall in >6kT deep wells and do not escape the surface.

The PEO layer collapse as a function of temperature for each $MgSO_4$ concentration can be obtained from theoretical fits to the measured potential energy profiles in Figure 4.5 (and 5 additional sets of evolving potential energy profiles). The solid curves in both cases are the van der Waals attraction as a function of distance between the silica colloid and glass or gold surfaces, which is the separation labeled as h in Figure 4.2. The van der Waals predictions are fit to the measured profiles in Figure 4.5 using absolute particle-surface separation as the only adjustable parameter. Because the sharp onset of osmotic repulsion between PEO layers at each condition is equal to twice the adsorbed layer thickness, 2δ in Figure 4.2, the potential energy profiles measured in Figure 4.5 in better than theta conditions, can be used to infer the

temperature and $MgSO_4$ mediated PEO layer collapse, $2\delta(T, C)$. Separations less than $2\delta(T, C)$ are sampled in each profile due to interpenetration and compression of the adsorbed layers and are artificially extended to shorter separations by ~10nm due to signal noise.[29]

The predicted van der Waals curves in Figure 4.5 require some explanation since they include contributions from both the core SiO_2 colloid and glass surface interaction as well as the PEO layers, which has been identified in previous measurements by us.[29-31] To first motivate consideration of the layer's contributions to the net van der Waals attraction, it is important to realize that the PEO layers have dielectric properties different from the intervening aqueous medium, colloid, and substrate materials, which indicates they have a finite contribution to the net continuum van der Waals attraction as expected from theoretical considerations.[138,140,142-145] For fully solvated PEO layers, the average concentration within the PEO layer is ~10vol% (based on an adsorbed amount of $2mg/m^2$, initial thickness of 20nm, and a bulk PEO density of 1 gm/cm^3, which are characterized and explained in extensive detail in previous papers[30,146,147]). These PEO layer characteristics produce dielectric properties within the adsorbed polymer layers not significantly different from the aqueous media in good solvent conditions. As the PEO layers experience a solvent quality mediated dimensional collapse into an increasingly concentrated polymer solution approaching a homogeneous film in the limit of complete phase separation, their contribution to the net van der Waals attraction increases. As a result, it seems important to at least consider the relative importance of the adsorbed PEO layer contribution to the net attraction.

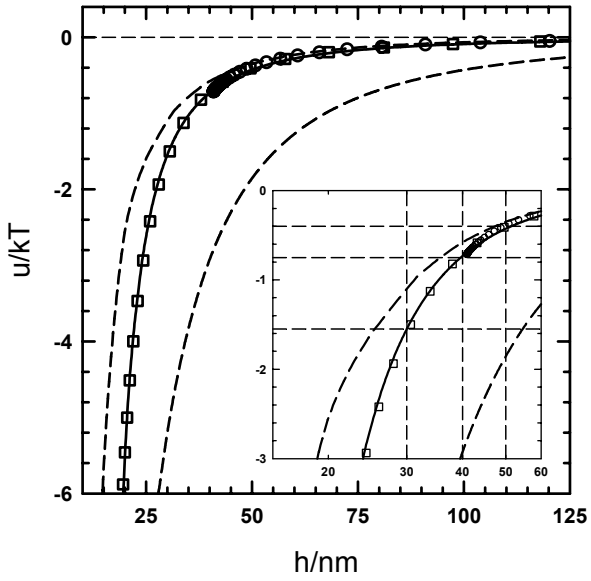

Figure 4.6. Theoretical van der Waals potentials for 1.58μm SiO_2 colloid-glass without (short-range ---) and with PEO copolymer (—) and for 1.58μm SiO_2 colloid-5nm gold coated glass without PEO copolymer (long-range ---).

To compute the contribution of the PEO layers to the net van der Waals attraction, we use the theory of Parsegian[138] that we have previously described in detail[30] but briefly explain here for completeness. To specify the nonuniform PEO layer dielectric properties in this theory, we use a parabolic concentration profile for a range of layer thicknesses that preserve the adsorbed amount[139] and then use a single peak model for the concentration dependent dielectric properties obtained from Cauchy plots[148] of PEO solutions.[30] Retardation and geometric effects are included by comparing bare colloid predictions from Parsegian's theory with retarded Lifshitz[149] predictions using the Derjaguin geometric correction.[114]

Figure 4.6 shows predictions of the van der Waals attraction between bare and PEO polymer coated colloids and surfaces as a function of solvent quality. Specifically, Figure 4.6 shows the bare 1.58 μm SiO_2 colloid-glass surface interaction as well as potentials for the same colloid-surface interaction but with 2 different PEO layer thicknesses for separations down to contact at 2δ. The 2 separate PEO coated surface potentials are shown in Figure 4.6 due to the unique potential obtained for each collapsed layer (as noted in previous work[30]). However, because these curves are approximately superimposable within ~0.1kT for the conditions investigated, they are reasonably well fit by a single solid line representing the van der Waals attraction between PEO coated surfaces for h>20nm.

From the predictions in Figure 4.6, it is clear that PEO layers have a negligible contribution beyond h≈40 nm. This is expected based both on the similarity of the fully solvated layers to the aqueous medium dielectric properties and the range over which very thin, fully collapsed layers are expected to affect the interaction.[138] However, for h<40nm an additional attraction >1kT is provided by dense collapsed layers that significantly affects the temperature and specific ion mediated equilibrium phase behavior and stability of such particles as well as the layer collapse inferred from measured potentials. The predicted van der Waals potential including the effect of the PEO layers in Figure 4.6 appears to be an accurate representation of the measured potentials in Figure 4.5a both in terms of functional shape, and as will be shown, in terms of absolute separation dependence.

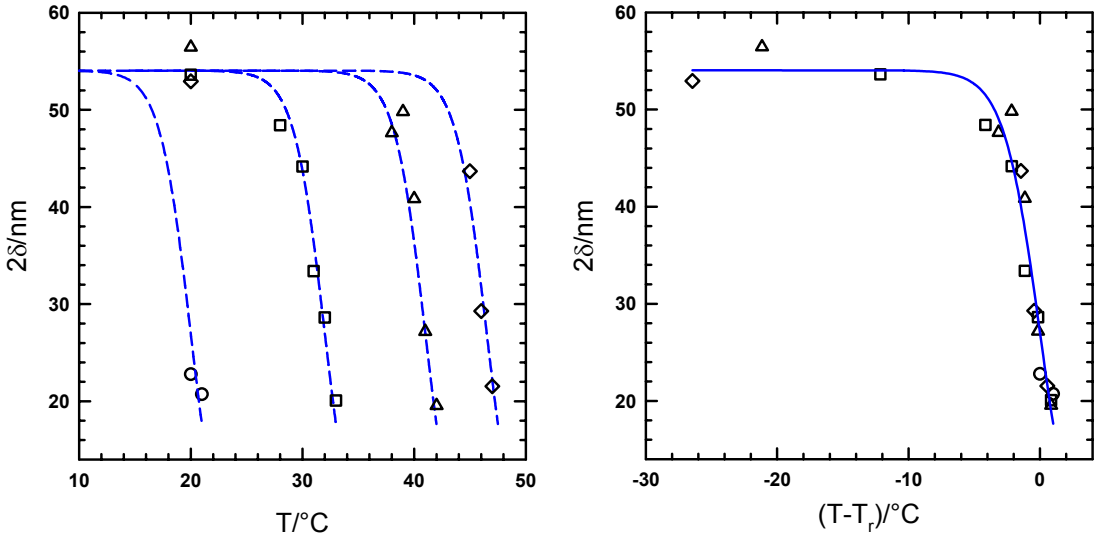

(a) (b)

Figure 4.7. (a) PEO layer collapse data obtained from van der Waals fits to measured 1.58μm SiO_2 colloid-glass potential energy profiles for $MgSO_4$ concentrations of 0.2M (◊), 0.3M (Δ), 0.4M (□), and 0.5M (O). The dashed curves (---) are sigmoidal fits to each data set. (b) Superposition of all PEO layer collapse curves from Figure 6a on transformed temperature scale with solid curve (—) showing single sigmoidal fit.

Based on the 1.58 μm SiO_2 colloid-glass surface van der Waals predictions in Figure 4.6, it is also clear that it is not necessary to consider the effects of the PEO layer in the interpretation of the van der Waals potential in Figure 4.5b where the glass slide has a 5nm gold film. Although the PEO layer contribution becomes significant for the 1.58 μm SiO_2 colloid-glass surface interaction for h<40nm, the increased colloid-substrate attraction due to the 5nm gold film results in colloidal deposition at h>40nm, rendering the PEO layer contribution insignificant for all measurements in this work involving the 5nm gold film.

4.3.3 Equivalence of Temperature and Specific Ion Mediated PEO Layer Collapses

From the representative curve fits shown in Figure 4.5 and to all evolving profiles for the levitated colloid conditions in Figure 4.4, $\delta(T, C)$ can be obtained as half the position of the energy minimum, which can be considered as the onset of osmotic macromolecular repulsion. Because of its determination via energetic considerations, values of $\delta(T, C)$ can also be expected to be different from other measurements including hydrodynamic thicknesses obtained from dynamic light scattering[146] or optical thicknesses measured using ellipsometry.[150] Figure 4.7a reports 2δ values extracted from 1.58 μm SiO_2 colloid-glass surface measurements for varying temperatures (T=20-47°C) at fixed $MgSO_4$ concentrations (C=0.2, 0.3, 0.4, 0.5M). Sigmoidal curve fits to each data set in Figure 4.7a are shown to represent the data and guide the eye, although this functional form is not known *a priori*.[151] The same sigmoidal form is used in all cases with only a single adjustable reference temperature for each $MgSO_4$ concentration.

Based on the functional similarity of the layer collapses in Figure 4.7a, Figure 4.7b shows superposition of all four measured data sets onto one universal curve by transforming the abscissa as T-T_r where T_r are fit reference temperatures in Figure 4.7a (T_r=46, 40, 31, 20°C for $MgSO_4$ C=0.2, 0.3, 0.4, 0.5M). This superposition suggests the equivalence of increasing temperature and increasing $MgSO_4$ concentration in controlling solvent quality dependent collapses of adsorbed aqueous PEO layers. In particular, the absolute PEO layer thickness and the rate of change of the layer collapse (vs. T) appear nearly identical at lower temperatures for increased $MgSO_4$ concentrations. In addition, effects of increasing temperature and $MgSO_4$ concentration

are additive and do not produce any non-linear response indicative of a synergistic mechanism due to combined temperature and specific ion effects. The data and curve fit in Figure 4.7b well represent the PEO layer collapse and evolving potentials between PEO copolymer coated 1.58 μm SiO_2 colloids and glass surfaces for all conditions investigated in this work (see Figure 4.4).

In assessing the accuracy of the inferred layer collapse in Figure 4.7, one issue to consider is the sensitivity of the measured potentials to the PEO layer thickness. For the 1.58 μm SiO_2 colloid-glass surface potentials in Figure 4.5a, the well depth is somewhat insensitive to the layer thickness for separations greater than ~50nm. As shown in the inset of Figure 4.6, a 10 nm change in 2δ from 50nm to 40nm corresponds to a well depth change of $0.3kT$ ($0.4kT$ to $0.7kT$), where the initial absolute well depth of $0.4kT$ and the change in the well depth by $0.3kT$ are both relatively close to the order $0.1kT$ experimental uncertainty associated with surface heterogeneity, polymer layer polydispersity, signal noise, etc. In contrast, a 10 nm change in 2δ from 40nm to 30nm corresponds to a well depth change of $0.9kT$ ($0.7kT$ to $1.6kT$), which has a smaller relative uncertainty given the greater absolute values and changes involved. As a result, the layer collapses in Figure 4.7 are more accurate for 2δ<50nm and T- T_T>-5°C, which is where steep change occurs in Figure 4.7b.

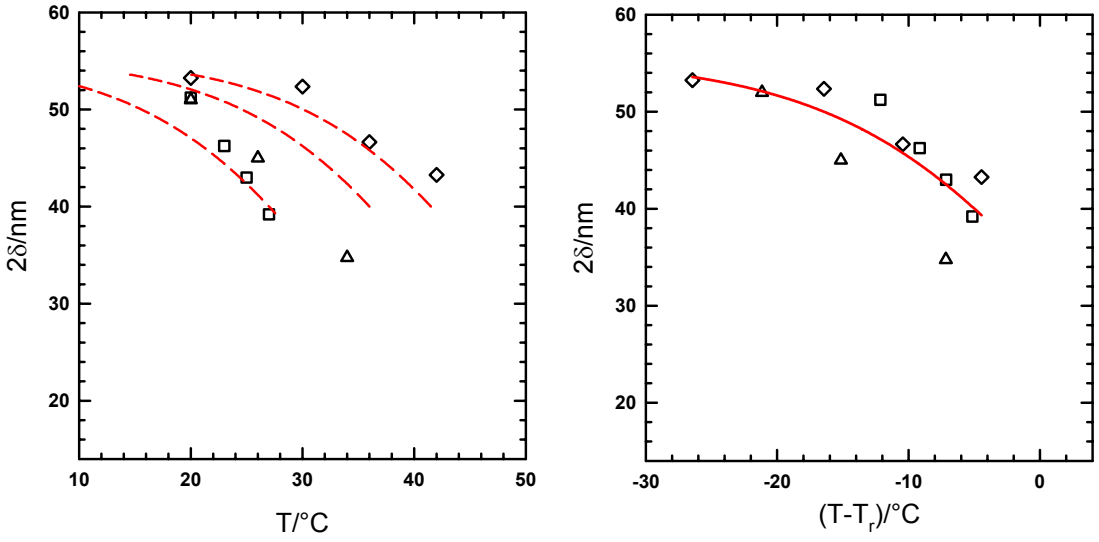

(a) (b)

Figure 4.8. (a) PEO layer collapse data obtained from van der Waals fits to measured 1.58μm SiO_2 colloid-5nm gold coated glass potential energy profiles for $MgSO_4$ concentrations of 0.2M (◊), 0.3M (Δ), and 0.4M (□). The dashed curves (---) are sigmoidal fits to each data set. (b) Superposition of all PEO layer collapse curves from Figure 7a on transformed temperature scale with solid curve (—) showing single sigmoidal fit.

To more sensitively probe the initial PEO layer collapse, Figure 4.8 shows 2δ values extracted from measurements of 1.58 μm SiO_2 colloids interacting with 5nm gold films on glass with T=20-46°C and C=0.2, 0.3, 0.4M $MgSO_4$ and sigmoidal curve fits. Because of the stronger substrate van der Waals attraction due to the 5nm gold film, the initial well depths for good solvent conditions in Figure 4.5b are >1.5kT so that the initial PEO layer collapse appears more rapid in Figure 4.8a than Figure 4.7a. In exchange for sensitivity to the initial layer collapse, the additional attraction encountered

due to the 5nm gold film produces colloid deposition for relatively good solvent conditions. As a result, the layer collapse cannot be measured following colloid deposition in good solvent conditions. The lack of layer collapse data in Figure 4.8a near theta conditions does not allow values of T_r to be obtained directly. However, using same values obtained in Figure 4.7a also produces a universal collapse in Figure 4.8b. It is reasonable that the same T_r values can be used to superimpose the layer collapses in all cases since similar hydrophobic surface modifications should produce similar adsorbed copolymer layer architectures and associated responses to temperature and $MgSO_4$ concentration changes.

To exploit the sensitivity of the different potentials to the PEO layer collapse in different solvent quality regimes, Figure 4.9 shows a composite layer collapse constructed from data in Figures 4.7 and 4.8. Specifically, the PEO layer collapse is fit to the gold film data for 2δ>40nm for the relatively good solvent conditions in Figure 4.8 and to the bare surface data for 2δ<40nm for the closer to theta conditions in Figure 4.7. Figure 4.9 shows three composite layer collapse curves including: (1) a fit to the data taken directly from Figures 4.7 and 4.8, (2) a fit to the collapse inferred from the potentials in Figure 4.5 that ignores the van der Waals contribution of the PEO layers, and (3) a fit to data inferred from the potentials in Figure 4.5 that also includes the effect of surface roughness in addition to the effect of the adsorbed copolymer. The effect of surface roughness was included using the theoretical potential in Figure 4.6 corrected by the factor, $[1+(20\text{nm}/2h)]^{2.1}$,[152] where 20nm is the peak-to-valley roughness (similar to previous work[19]) and the 2.1 power is based on an approximate fit to the exact results for

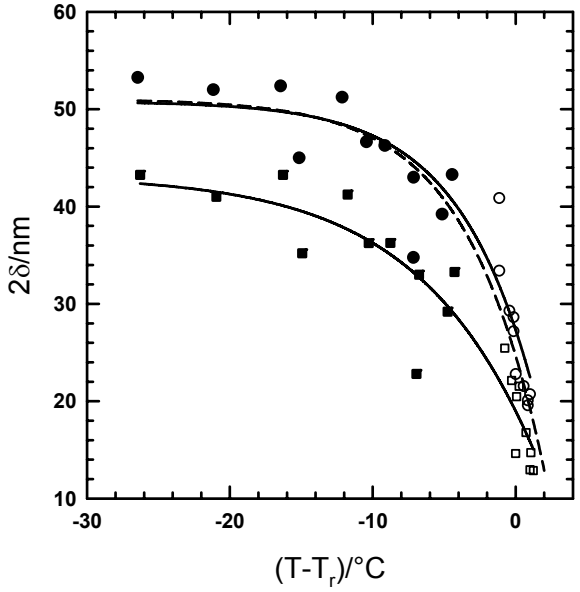

Figure 4.9. Composite PEO layer collapse curves from data in Figures 6 and 7. The circles are based on van der Waals potentials including effects of PEO copolymer with open circles (O) based on bare glass data in Figure 6 an filled circles (●) based on gold coated glass data in Figure 7. The squares are based on van der Waals potentials including effects of PEO copolymer and surface roughness with open squares ( ) based on bare glass data in Figure 6 an filled squares (■) based on gold coated glass data in Figure 7. Solid curves (—) are fits to the two data sets and the dashed curve (---) is based on potentials fit to van der Waals potentials that do not include either PEO copolymer or surface roughness effects.

the separations of interest in this work.[153]

The three curves in Figure 4.9 demonstrate the effects of considering the PEO layer contribution and surface roughness to the net van der Waals colloid-surface attraction when inferring the PEO layer collapse. Although the curves with and without the polymer layer contribution are initially similar, they are different by ~10nm near theta conditions. By including the effects of roughness in addition to the polymer layer

contribution, the absolute value of initial layer thickness ($2\delta \approx 40$nm) displays good agreement with independent measurements of single PEO layers adsorbed to hydrophobically modified surfaces.[29,146,154,155] If the PEO layer and surface roughness contributions are not included, the initial brush layer thickness is closer than expected to the PEO block contour length (~40nm), and the fully collapsed layer is too thin with dimensions approaching zero to produce films with greater densities than bulk PEO. In any case, the collapse in Figure 4.9 on the transformed temperature scale accurately represents kT scale van der Waals potentials between PEO-PPO-PEO copolymer coated colloids and surfaces in better than theta conditions including temperature and $MgSO_4$ concentration effects.

The PEO layer collapse in Figure 4.9 is also consistent with relevant theory and previous measurements. Theoretical predictions for the solvent quality dependent collapse of adsorbed or grafted brushes suggest a second order, or continuous, transition on planar surfaces (instead of a first order or discontinuous transition at the theta temperature).[151] As a result, the continuous collapse in Figure 4.9 is expected for the wall surface and colloids with radii large compared to adsorbed layer dimensions ($a/\delta \sim 40$). The collapse is also generally consistent with a previously reported collapse indirectly inferred from rheological measurements of the same PEO layers on smaller 360nm polystyrene colloids in the same temperature and $MgSO_4$ concentration range.[31] A somewhat different functional dependence of the collapse is obtained in this work that is expected to be the more accurate given the direct and sensitive nature of ETIRM measurements compared to rheological measurements.

4.4. Conclusions

ETIRM measurements of temperature and specific ion mediated potential energy profiles are used to infer the solvent quality dependent collapse of PEO-PPO-PEO copolymers adsorbed to hydrophobically modified surfaces. A composite PEO layer collapse curve is obtained from measurements of bare and gold coated glass substrates having different levels of van der Waals attraction to provide maximum sensitivity to different solvent quality regimes. By including both adsorbed polymer and roughness contributions to the net van der Waals attraction, the inferred layer collapse displays good agreement with expected limits based on the PEO block contour length and the bulk PEO density. Superposition of all PEO layer collapse data onto a single universal curve, via a transformed temperature scale relative to reference temperatures in each case, suggests the equivalence of increasing temperature and increasing $MgSO_4$ concentration in decreasing solvent quality and the collapse of adsorbed copolymers.

Ultimately, the inferred PEO layer collapse inferred from van der Waals predictions accurately captures the nanometer and kT scale interaction potentials of PEO-PPO-PEO copolymer coated colloids as a combined function of varying temperature and $MgSO_4$ concentration. Understanding how to manipulate such interactions between polymer coated colloids provides the ability to reversibly control the stability, phase behavior, and self-assembly of such particles.

5. INTERFACIAL COLLOIDAL CRYSTALLIZATION VIA TUNABLE HYDROGEL DEPLETANTS

5.1. Synopsis

In this section we demonstrate the use of a colloidal system that allows reversible, attraction-induced interfacial crystallization of colloids. Crosslinked microgel particles of the thermoresponsive polymer PNIPAM have been used to obtain tunable depletion attraction in a quasi-2D system of SiO_2 colloids. The change in the SiO_2 colloid interparticle and particle-substrate interaction with temperature and its effect on the resulting phase behavior of the system are measured and quantified by a combination of Video Microscopy (VM) and Total Internal Reflection Microscopy (TIRM). The directly measured temperature dependent forces are then used in simulation studies to verify the structure and dynamics of the experimentally observed phases.

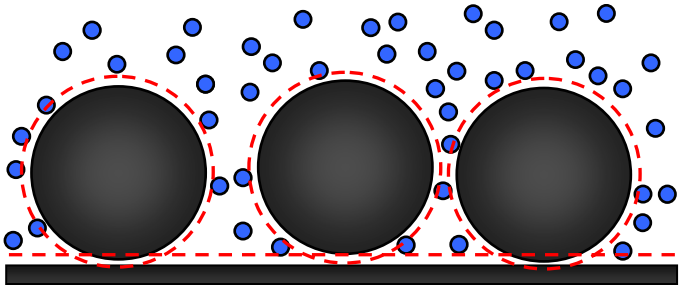

Figure 5.1. A schematic representation of a mixture of 2.34μm SiO_2 (black) and 24% (v/v) PNIPAM microgel (blue) colloids levitated above a homogeneous glass surface. The red curves represent excluded volumes for the PNIPAM colloids.

5.2. Introduction

Depending on their solution concentration, macromolecular and colloidal depletants directly determine the interaction potentials and consequently the phase behavior of the larger colloids in binary mixtures. Bulk, three-dimensional, depletion-induced colloidal crystallization has received much theoretical[43,44,115] and experimental[46-48,53,55,156-158] attention. Interfacial crystallization studies in such three-dimensional systems reveal the advent of depletion induced, wall-crystals well before bulk crystal nucleation.[56,57,63] Confined binary colloidal mixtures have been used to study two-dimensional depletion crystallization.[64-66] In addition to the widely reported depletion attraction-driven equilibrium phase transitions, both two and three dimensional colloidal systems display arrested states at sufficiently high depletant concentrations, some of which rearrange into their thermodynamic equilibrium configurations over time.[55,64-66,158] However, direct measurements of interparticle and particle-wall depletion potentials complimenting direct visualization studies of phase behavior have yet to be performed.

The ability to directly measure and quantify the effective depletion interaction is invaluable for understanding the accompanying phase behavior. The assumption that the depletants behave like an ideal gas, combined with simple excluded volume calculations allows particle size ratio and depletant concentration effects to be expressed in the form of a simple effective attractive depletion potential (Asakura and Oosawa or AO potential) between the larger colloids.[33] Video (VM) and Total Internal Reflection Microscopy (TIRM) techniques have been used to directly measure particle-particle and

particle-wall depletion potentials respectively.[20,34,37-40] While the AO model satisfactorily explains the recorded potentials for systems with low depletant concentrations,[20] quantification of higher depletant concentration effects require more rigorous methods like Density Functional Theory (DFT).[38] Barring a recent VM experiment,[21] all phase behavior and potential measurement studies have focused exclusively on systems with fixed large and small particle sizes, thereby restricting themselves to non-tunable potentials.

We present the first direct measurements of tunable depletion potentials and VM studies of the accompanying phase behavior in a purely two-dimensional system. Our system consists of 2.34 μm silica particles and 220nm poly-*N*-isopropylacrylamide (PNIPAM) microgel depletants levitated over a homogeneous silica substrate in 1.5mM sodium chloride (NaCl). The reversible, continuous volume transition that PNIPAM microgel particles exhibit in water at around 34°C is well documented.[78,159] This temperature dependence of depletant size is exploited to tune particle-particle and particle-substrate interaction potentials and thereby directly influence equilibrium phase behavior. The structure and dynamics of the resultant equilibrium phases are measured. We observe the occurrence of crystalline phases at lower temperatures (20°C-26°C) and fluids at higher temperatures (28°C-29°C), with the temperature effect being completely reversible. We also report the formation of temporary arrested states on initial assembly of the cells, for the depletant concentration used in our work. These non-equilibrium structures relax over time into crystalline phases, displaying a spinodal-like behavior.[55,64,66]

Table 5.1. Parameters used in TIRM theoretical fits and MC simulations based on VM measured radial distribution functions. Adjustable parameters are shown in bold. All other parameters were fixed from independent measurements described in the following notes: (a) fits to the gravitational contribution to the TIRM measured potential energy profiles, (b) DLS measurements, (c) zeta potential measurements.

$T(°C)$												
	20	22	24	26	27	28	28.5	29	29.5	30.5	31	31.5
$2a$(nm)[a]	1100	1100	1100	1100	1100	1100	1100	1100	1100	1100	1100	1100
$2L$(nm)[b]	227	224	220	212	207	200	196	192	187	176	170	163
$-\psi_p, -\psi_p$(mV)[c]	50	50	50	50	50	50	50	50	50	50	50	50
κ^{-1} (nm)	8	8	8	8	8	8	8	8	8	8	8	8
C(mM)	1.5	1.5	1.5	1.5	1.5	1.5	1.5	1.5	1.5	1.5	1.5	1.5
(ETRIM) fix B_{2HS}, adjust n												
$n(10^{-8}\text{nm}^{-3})$	**6.13**	**6.13**	**6.13**	**6.13**	**6.13**	**6.24**	**6.13**	**6.13**	**6.22**	**5.4**	**5.05**	**5.35**
ϕ	0.37	0.36	0.34	0.31	0.28	0.26	0.24	0.22	0.21	0.15	0.13	0.12
$B_2(10^{-7}\text{nm}^3)$	2.44	2.34	2.22	2.00	1.86	1.68	1.58	1.47	1.36	1.14	1.03	0.90
$\Pi/kT(10^{-7}\text{nm}^{-3})$	1.53	1.50	1.45	1.37	1.31	1.28	1.21	1.17	1.15	0.87	0.76	0.78
(ETIRM) fix n, adjust B_2												
$n(10^{-8}\text{nm}^{-3})$	6.13	6.13	6.13	6.13	6.13	6.13	6.13	6.13	6.13	6.13	6.13	6.13
$B_2(10^{-7}\text{nm}^3)$	**2.44**	**2.34**	**2.22**	**2.00**	**1.86**	**1.80**	**1.58**	**1.48**	**1.40**	**0.68**	**0.40**	**0.43**
$\Pi/kT(10^{-7}\text{nm}^{-3})$	1.53	1.50	1.45	1.37	1.31	1.29	1.21	1.17	1.14	0.87	0.76	0.78
(iMC) adjust Π												
$\Pi/kT(10^{-7}\text{nm}^{-3})$	**1.36**	**1.37**	**1.25**	**1.3**	**-**	**1.13**	**-**	**0.65**	**-**	**-**	**-**	**-**

5.3. Results and Discussion

5.3.1 Simulation Studies

A variety of simulation studies are presented in this section. We briefly explain these methods here. In order to quantify experimental observations of equilibrium structure, 2D (*NVT*) inverse Monte Carlo (MC) simulations were performed for 512 SiO_2 colloids with a mean diameter of 2.0μm and a geometric standard deviation of 1.076.

The salt concentration was fixed at 1.5mM and the net interparticle interaction, a sum of an electrostatic repulsion and an AO attraction ($u_{edl}(h)$ and $u_{dep}(h)$ in Equation 2.2), was varied until good agreement was obtained between the experimental and simulated radial distribution functions. The detailed list of parameters used to define the interaction potential in the simulations is provided in Table 5.1. All inverse Monte-Carlo (MC) simulations were run at a core particle area fraction of $\phi_A = 0.225$ for 10^7 steps with data collection commencing after 10^6 steps. In order to quantify the experimentally observed equilibrium dynamics, 3D, forward MC simulations ($\phi_A = 0.225$) were performed for 36 monodisperse SiO_2 colloids with a mean diameter of 2.2μm and fixed particle-wall and interparticle potential energy profiles. The equilibrium configurations obtained from these simulations were then used to obtain short time self-diffusion coefficients (D_S^S) by the method of Brady and Bossis.[124] A detailed discussion of the procedure is documented in Section 2 (Section 2.4).

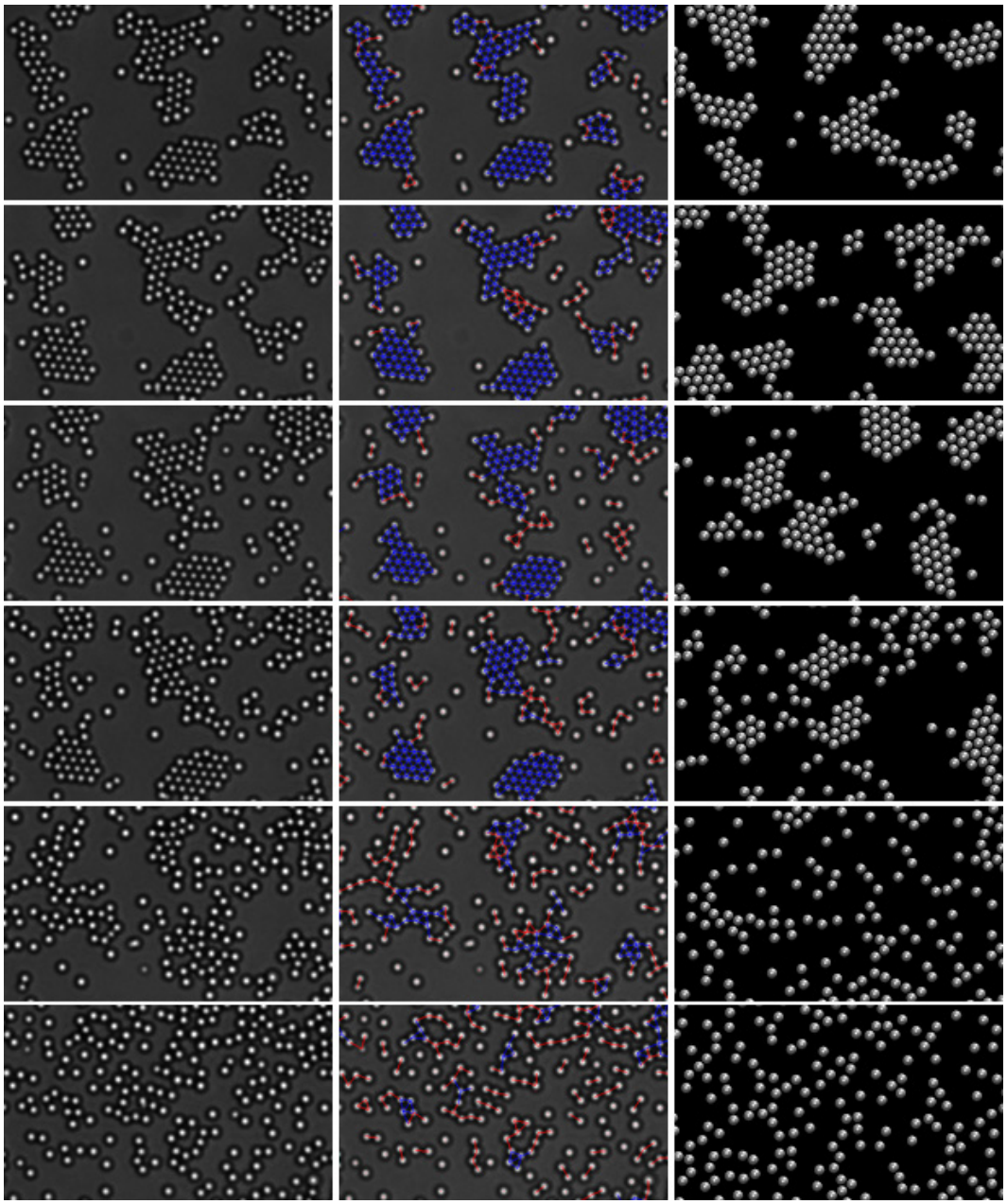

Figure 5.2. 2D configurations of 2.34 μm SiO_2 particles over a homogeneous substrate at T = 20 °C, 22 °C, 24 °C, 26 °C, 28 °C and 29 °C respectively obtained from experiment (Column 1, top-bottom) and simulation (Column 3, top-bottom). (Column 2, top-bottom) Equilibrium configurations with populations of colloids in regions of high connectivity and order (blue lines) separated from those in regions of low connectivity and order (red line). The interparticle depletion potentials used in these MC simulations are shown in Figure 5.3d.

5.3.2 Local Bond Orientation Order Parameter

Average local bond orientation order parameter (ψ_6) was used to quantify the degree of crystallinity in the observed phases. The bond orientation order parameter was evaluated for each particle (j) as $\psi_6(j) = \left|(1/N)\Sigma e^{6i\theta jk}\right|$ for its N number of neighbors (k), a neighbor being a particle that fell within the separations that defined the first peak of the radial distribution function ($g(r)$) for that phase. At a fixed temperature, ψ_6 was obtained by averaging over all particles that had $N \geq 3$ and over all recorded frames. For perfect six-fold symmetry, ψ_6 assumes a value of 1. Many factors like polydispersity lower this value as they affect the quality of the crystalline phase. For all studies in this Section, all particles with $\psi_6 \geq 0.8$ were considered part of an ordered assembly and were connected to their neighbors by blue lines. Particles that did not meet this criterion were connected to their neighbors by red lines.

5.3.3 Quasi 2D Colloidal Crystallization: Equilibrium Structure

Figure 5.2 shows experimental (VM) and simulated (MC) results for the PNIPAM hydrogel depletant-mediated quasi two dimensional crystallization of 2.2μm SiO_2 colloids. Results are reported as a function of temperature (T=20-29°C), which controls the PNIPAM size and the resulting magnitude and range of the depletion attraction. The aqueous media also contained 1.5mM NaCl which allowed colloids to be electrostatically stabilized in the presence of weak depletion attraction. The experimental crystals were observed to relax over several hours from initially three dimensional aggregated networks whereas fluid microsctructures equilibrated over time

periods on the order of minutes. In Figure 5.2, the first column shows single unprocessed experimental observations, the second column shows images with colored lines added showing triangulation and indicating the local bond orientational order, and the third column show MC simulated configurations based on independently measured depletion potentials (Equation 2.13).

For each temperature, the two-dimensional equilibrium configurations obtained from simulation and experiment in Figure 5.2 display close agreement. In both cases, gas-solid coexistence is observed for T<28°C whereas a concentrated homogeneous liquid is observed for T>28°C. Depletion potentials used to generate the MC simulated configurations in Figure 5.2 were measured using two methods including: (1) directly between the particles and wall using ensemble total internal reflection miscropy[118,122] with fits to Equations 2.14-2.16 as shown in Figure 5.3a & b, and (2) via an inverse MC method[160,161] that takes into account image resolution limitations and polydispersity[162] with fits to Equations 2.2 & 2.13 as shown in Figures 5.3c, d. Figure 5.3a shows ensemble averaged height histograms for of 2.2μm SiO_2 colloids, and Figure 5.3b shows $u^{pw}(h)$ obtained via a Boltzmann inversion of the histograms in Figure 5.3a (Equation 2.19). Figure 5.3c shows time averaged $g(r)$ obtained from image data sets (containing the single images in Figure 5.2, Column 1) and inverse MC simulations, and Figure 5.3d shows $u_{pp}(h)$ obtained from via the inverse MC algorithm.

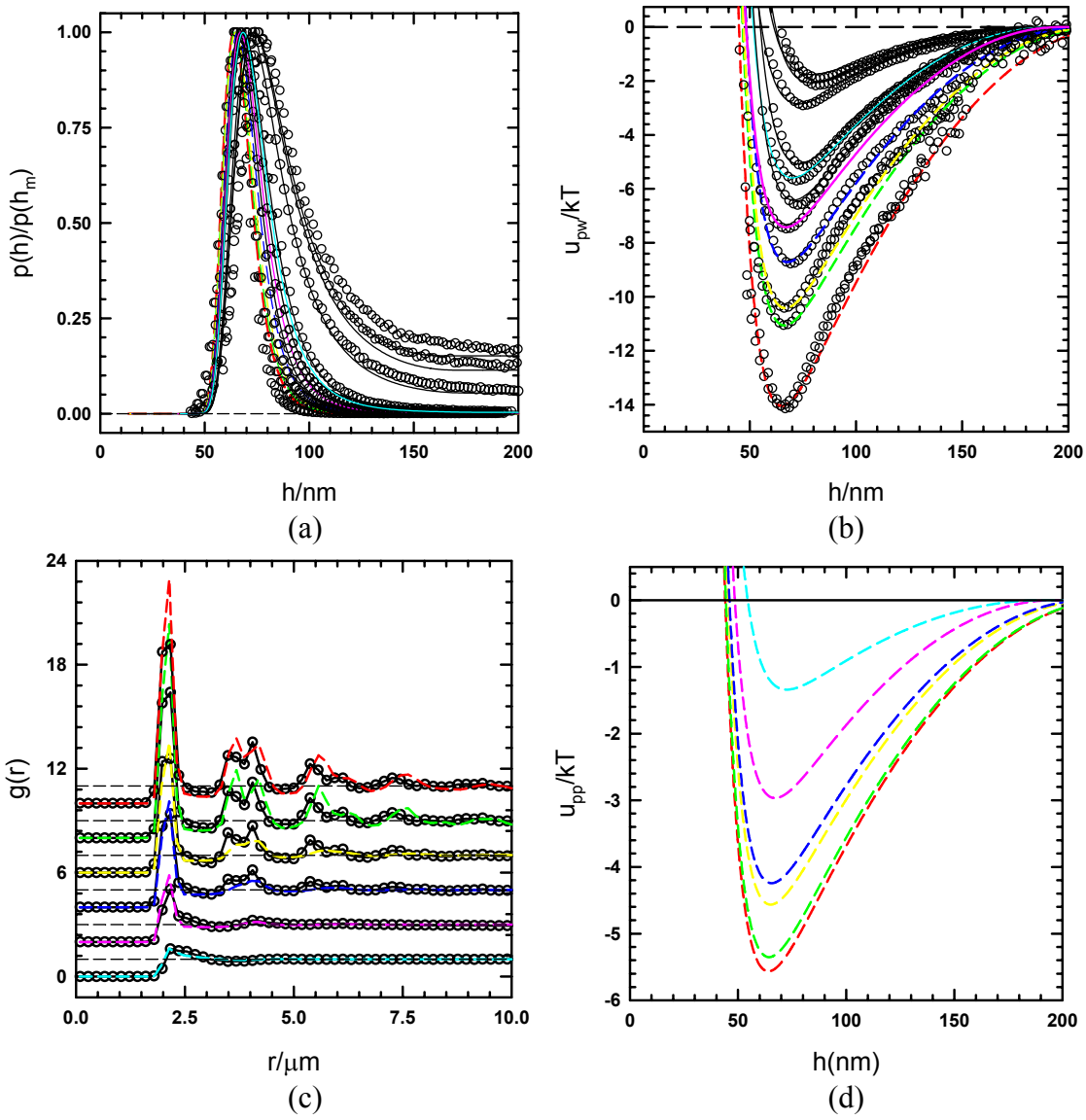

Figure 5.3. (a) Gravity included, ensemble-average 2.34 μm SiO_2 particle-wall distribution functions at temperatures of T = 20–31.5 °C. (b) Gravity subtracted, ensemble-averaged particle-wall potentials determined from the distribution functions in (a) at temperatures of T = 20–31.5 °C (bottom-top) and a salt concentration of C = 1.5mM NaCl. The colored lines represent theoretical fits to interactions at temperatures of T = 20 °C (red), 22 °C (blue), 24 °C (green), 26 °C (yellow), 28 °C (pink) and 29 °C, at which phase behavior experiments reported in Figure 5.2 were performed. (c) (Open circles, bottom-top) Equilibrium two-dimensional radial distribution functions corresponding to experimental observations reported in Figure 5.2 (Column 1, top-bottom). The colored lines represent g(r)'s obtained from the inverse MC simulations (Column 3, top-bottom) carried out at equivalent solvent conditions. (d) Interparticle potentials obtained from inverse MC simulations that yield the g(r)'s curves shown in Figure 5.3c (colored lines).

Table 5.1 summarizes the parameters that define the 2.34 μm SiO_2 colloid interparticle and particle-wall interaction potentials as a function of temperature. Figure 5.3 and Table 5.1 clearly show that as the temperature is increased, the 2.34 μm SiO_2 interparticle and particle wall attraction decreases monotonically. This reduction in attraction with increasing temperature is what causes gas-solid coexistence to be observed for T<28°C as opposed to a concentrated homogeneous liquid for T>28°C. The cause for this reduction in attraction with increased temperature is the shrinking of the thermoresponsive PNIPAM particles.

Figure 5.4a (top) and Table 5.1 quantify this effect of decreasing PNIPAM particle size with increasing temperature from independent DLS measurements (red points). Table 5.1 shows that if we assume hard sphere (HS) behavior for the PNIPAM particles over this range of temperatures, the resulting osmotic pressure between the 2.34 μm SiO_2 colloids and the glass wall obtained by fitting Equations 2.14-2.16 to the ETIRM data in Figure 5.3b decreases with increasing temperature in the manner shown by the open red circles in Figure 5.4a (bottom). Figure 5.4b (top) and Equation 2.16 specify the second virial coefficient (B_2) for PNIPAM colloids that display HS behavior over the entire range of temperatures investigated in this work (red crosses). Figure 5.4b (bottom) and Table 5.1 also provide estimates of the PNIPAM particle number density, n, and volume fraction, ϕ (red circles).

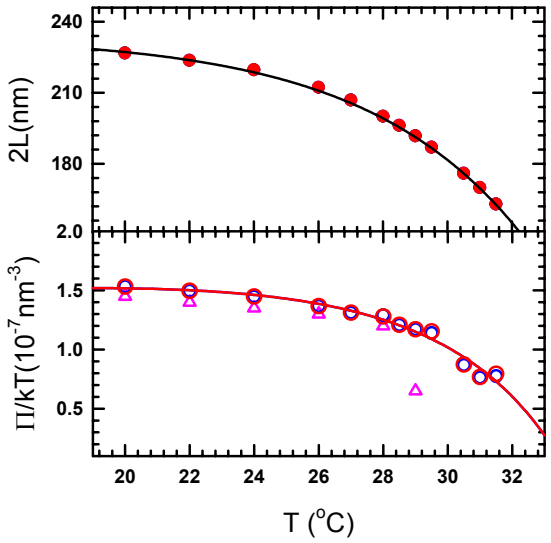

(a)

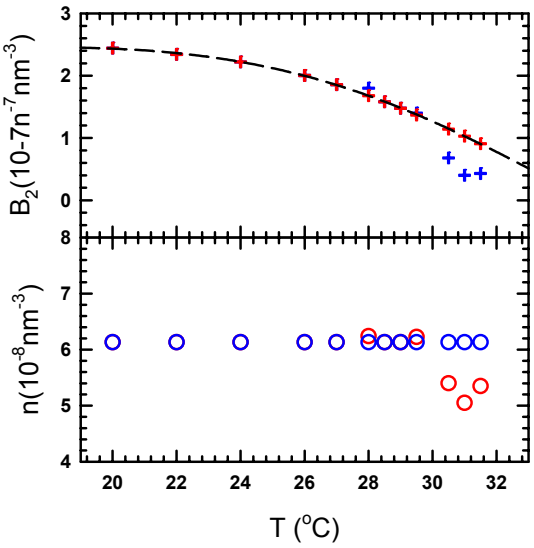

(b)

Figure 5.4. (a-top) An estimate of the temperature dependent PNIPAM microgel depletants size obtained from DLS measurements (solid line and closed black circles). (a, bottom) Osmotic pressure values obtained from ETIRM (red and blues circles) and iMC studies (pink triangles). PNIPAM second virial coefficients (b, top) and depletant number density (b, bottom) obtained from ETIRM data fits. All parameters obtained from fits that assume hard sphere behavior are in red and those obtained from fits that use the second virial coefficient are in blue.

If HS behavior of PNIPAM particles is assumed at T>30.5°C, the resulting fits indicate a drop in PNIPAM concentration, indicating adsorption of PNIPAM. However we know that temperature values of T > 30.5 °C are close to the LCST of PNIPAM (T = 32 °C)[163], which could result in attractive interactions between the depletant particles, thus invalidating the HS assumption under these solvent conditions. The blue crosses in Figure 5.4b (top) show that the PNIPAM particles indeed deviate from HS behavior (red crosses) at T > 30.5 °C from fits to the ETIRM data in Figure 5.3b by Equations 2.14-2.15 wherein we assume no adsorption of PNIPAM (Figure 5.4b (bottom), blue circles). The resulting osmotic pressure values extracted for this fitting assumption are plotted as open blue circles in Figure 5.4a (bottom). The osmotic pressure values extracted from $u_{pp}(h)$ obtained from via the inverse MC algorithm are represented by pink triangles in Figure 5.4a (bottom) and show good agreement with the ETIRM measurements.

All the phase behavior studies presented in Figure 5.2 are for a temperature range of T=20-29°C, wherein the PNIPAM particles display HS behavior. The volume fraction of depletants corresponding to the extracted number density at room temperature is ~ 37%, roughly 1.5 times the expected value of 24%. This because Equations 2.12-2.16 assume a uniform density distribution of the PNIPAM depletant particles, an assumption that fails at higher depletant volume fractions due to structuring effects in the depletant fluid. To rigorously account for these shortcomings, density functional theory (DFT) would have to be used to correctly estimate the theoretical bulk density from Equations 2.12-2.16.[38] Figures 5.3 and 5.4 and Table 5.1 completely quantify and explain the 2.34 μm SiO_2 colloid phase behavior from accurate assessments of SiO_2

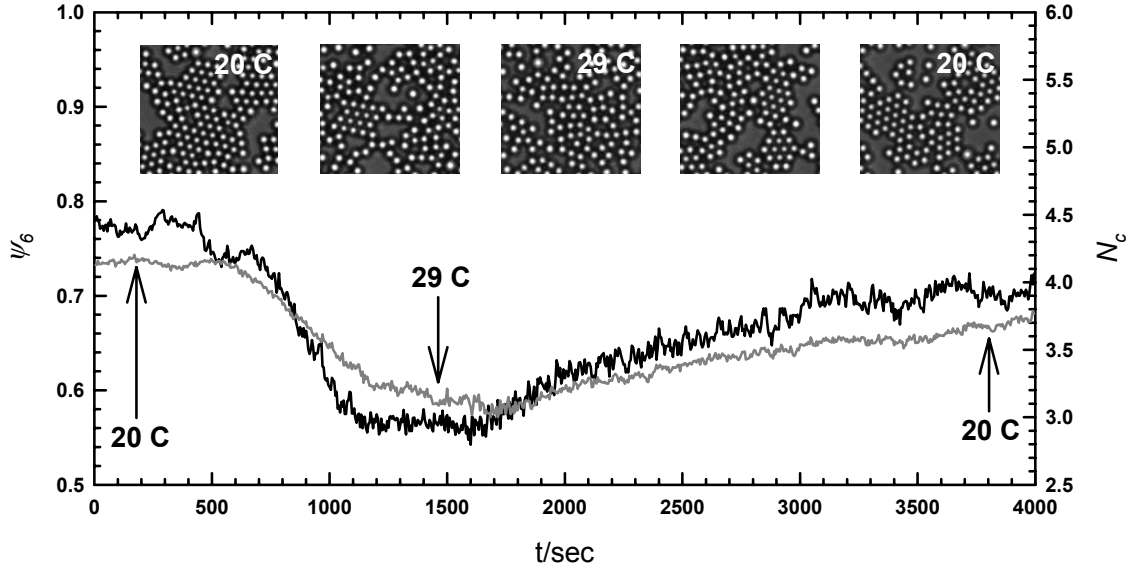

Figure 5.5. The reversible nature of the temperature induced phase transition in the larger 2.34 μm SiO_2 colloids shown by tracking local bond orientation order parameter (black curve) and coordination number (gray curve).

colloid interparticle and particle wall interaction potentials as a function of changing PNIPAM particle size and interaction.

In order to quantify the reversible nature of the tunable depletion induced phase behavior, we performed a non-equilibrium experiment in which the system was first heated from T = 20-29 °C and then cooled from T = 29-20 °C (Figure 5.5). We kept track of the bond order parameter ψ_6 and the coordination number *Nc* values during the course of this experiment, with the snapshots in Figure 5.5 showing the changing structure at various times. The data clearly shows that as the temperature is increased, the crystal melts and on restoration original conditions, it returns to its original crystalline state. Even though only one temperature cycle is shown in this report, we

observe no change in the either the reversibility of this process or the observed phase behavior even after repeated temperature cycling. There are two important observations from Figure 5.5 that need clarification.

The first observation is the obvious difference in rate at which the crystals disappear and the rate at which they grow. While the melting and freezing processes are kinetically different, the data presented here cannot be analyzed to this end because the rates of heating and cooling for our setup are vastly different and we did not keep track of the time dependent changes in the temperature during the course of the experiment. Another difference is that ψ_6 does not return to its original value, instead for the timeframe of the experiment, it finishes at a lower value. It is important to keep the observation timeframe in mind while comparing the initial and final states in this experiment.

At all solvent conditions conducive to crystallization ($T \leq 26$ °C), the longer the system was allowed to equilibrate, the larger the crystals that formed, and greater the rearrangements. For both, the equilibrium measurements in Figure 5.2 and for the initial state in Figure 5.5, we afforded the system ~1hr for rearrangements before beginning the experiments. In Figure 5.5, we observed the system for only ~0.5hr after the first nucleation event on cooling, at t~1800sec, resulting in the observed discrepancy. At room temperature, if we had afforded the system more time, we would have obtained larger domains and possibly better quality crystals. The primary objective of this work

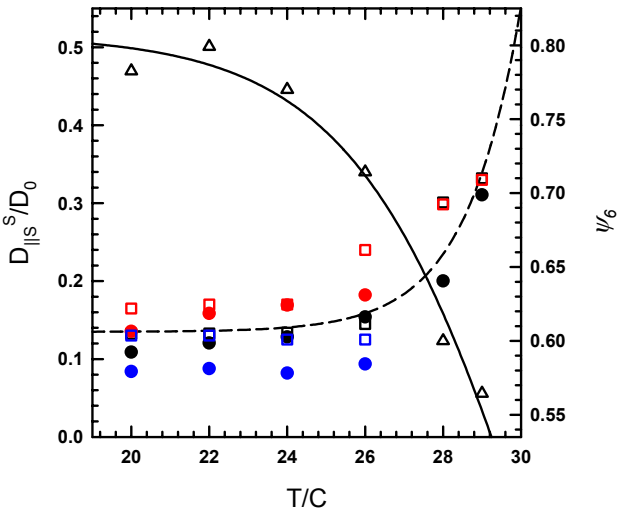

Figure 5.6. Temperature dependent, experimental, normalized, short-time lateral self-diffusivities ($D_{\|S}^S/D_0$) averaged over all observed particles (closed black circles) compared with those from MC simulations (open black squares). The solid blue circles correspond to experimental, ensemble averaged short-time lateral self-diffusivities for only those particles that are in the solid phase (Those connected by blue lines in Figure 5.2 – Column 2). The solid red circles correspond to experimental, ensemble averaged short-time lateral self-diffusivities for only those particles that are in the fluid phase (Individual particles and those connected by red lines in Figure 5.2 – Column 2). The blue and red squares are the ensemble averaged short-time lateral self-diffusivities for the corresponding solid and fluid phases in the simulations. The open triangles correspond to average local six-fold bond orientation order parameters for the experimentally observed phases in Figure 5.2. The lines are guides to the eye.

is to introduce the concept of completely quantified, tunable, reversible, attraction-driven two dimensional phase behavior for which the domain sizes obtained after ~1hr suffice.

5.3.4 Quasi 2D Colloidal Crystallization: Equilibrium Dynamics

Figure 5.6 quantifies the structure and dynamics of the equilibrium two-dimensional phases reported in Figure 5.2. As is evident from Figure 5.2, Figure 5.6 shows $\psi_6 \approx 0.8$ at T = 20 °C, indicative of high amounts of six-fold symmetry due to the presence of an equilibrium crystal phase (triangles). As the temperature is increased, the strength of the interparticle depletion attraction eventually weakens (Figure 5.3d) to a point where the crystal sublimates, indicated by a lower value of $\psi_6 = 0.6$ at T = 28 °C. At the next higher temperature of T = 29 °C, ψ_6 drops further, indicating that strength of the interparticle attraction at T = 28 °C, while insufficient to induce crystallization at the given area fraction of $\phi = 0.225$, still results in a more strongly associated fluid than the phase at T = 29 °C. We expect this value of ψ_6 to decrease further as the larger particles become more hard-sphere-like.

While the strength of the interparticle depletion attraction is sufficient to induce crystallization at all temperatures of T ≤ 26 °C, ψ_6 asymptotes to a value of *0.8* for all crystallites below 26 °C. As mentioned earlier, the reason ψ_6 does not asymptote to unity is partly due to the limited lateral resolution in the VM experiments (190nm/pixel), which compromises the accuracy with which particle centers and hence the angles that can be measured, thus directly affecting ψ_6, a parameter which depends on the accuracy with which these angles can be measured. This effect is overshadowed by the high polydispersity of the 2.34μm SiO_2 colloids (7.6%), which has a major effect on six-fold symmetry and the quality of the crystals. The lower the polydispersity of the SiO_2

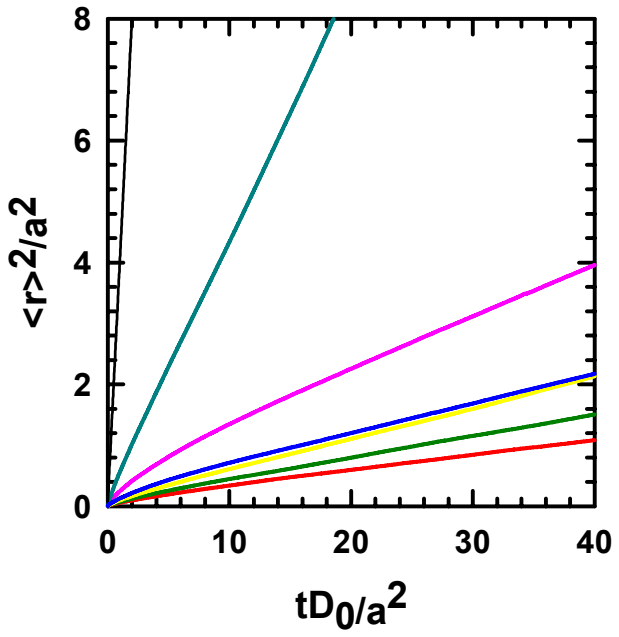

Figure 5.7. Ensemble averaged mean squared displacements for the SiO_2 colloids shown in Figure 5.2. The different colored curves represent MSDs at T = 20°C (red), T = 22 °C (green), T = 24°C (yellow), T = 26°C (blue), T = 28°C (pink) and T = 29°C (cyan) respectively.

colloids, the closer to unity ψ_6 would get for all the crystals at temperatures of T ≤ 26 °C. The ψ_6 still does capture the structural changes in the equilibrium phases as they go from a crystal at T ≤ 26 °C to a fluid at T ≥ 28 °C (Figure 5.6, squares).

The dynamics of the system in its different equilibrium states in Figure 5.2 was quantified by constructing ensemble averaged 2.34μm SiO_2 particle lateral mean square displacements (MSD) at each temperature (Figure 5.7). The Short-time lateral self-diffusivities ($D_{\|S}^{S}$), obtained from these lateral MSDs, contain information about how the Brownian motion of a particle is affected by hydrodynamic interactions with the

underlying substrate as well as its neighbors on diffusive length scales less than the particle radius *a*. We have already measured and quantified that decreasing temperature increases both the interparticle as well as the particle-substrate attraction, resulting in smaller equilibrium interparticle and particle-substrate separations. As shown in Figure 5.6, $D_{\|S}^{S}$ quantifies this reduction in local particle mobility.[164]

Figure 5.6 shows the experimentally determined values of $D_{\|S}^{S}/D_0$ (solid black circles) averaged over all particles in the system irrespective of whether they are in the gas or solid phase. D_0 in this case is the Stokes-Einstein diffusivity ($D_0=kT/6\pi\mu^* a$) for a single 2.34μm SiO_2 particle diffusing through a solvent consisting of PNIPAM microgel hard sphere depletants in water. The adjusted viscosity of the solvent phase (μ^*) is calculated from Equation 5.1 by De Kruif et al[165], approximated to the third order in ϕ. As mentioned earlier, we know the small particle volume fraction and radius at T = 20 °C to be ϕ = 0.24 and L =111nm respectively. Because we know how L varies with T, we also know how ϕ varies as a function of T, which allows complete specification of μ^* (Equation 5.1) and as a result, $D_{\|S}^{S}/D_0$ over the entire range of temperatures investigated in this report.

$$\eta_{dep}/\mu = 1 + 2.5\phi + 4\phi^2 + 42\phi^3 \qquad (5.1)$$

Normalized short-time lateral self-diffusivities ($D_{\|S}^{S}/D_0$) obtained form MC simulations and averaged over both solid and gas phase colloids are also shown in Figure 5.6 (open black squares). These values were obtained from equilibrium configurations of 36, 2.34μm silica particles levitated over a silica substrate for particle-

substrate and interparticle interaction potentials shown in Figures 5.3b and 5.3d respectively by using the method of Brady and Bossis.[124] In these simulations, the PNIPAM depletants are not physically present, their contribution being entirely accounted for in the effective depletion potentials. As a result, the solvent viscosity used in determining D_0 in this case is that of water.

The simulation results show remarkable agreement with the experimental data. $D_{||S}^{S}/D_0$ values decrease with increasing attraction strength, a result of the decrease in equilibrium particle separation as the system is cooled to T = 20 °C. The $D_{||S}^{S}/D_0$ values can be directly related to estimate the lifetime of interparticle bonds though $\tau = (a^2/D_{||S}^{S})exp(-u_{min}/kT)$ (Figure 5.3d). Figure 5 shows that particles in crystallites at lower temperatures (higher attraction) move and rearrange slower than those at higher temperatures as is revealed by the ratio of bond lifetimes ($\tau_{20\,°C}/\tau_{22\,°C} = 1.37$, $\tau_{22\,°C}/\tau_{24\,°C} = 2.34$, $\tau_{24\,°C}/\tau_{26\,°C} = 1.654$). For temperatures of T ≥ 28 °C, the attraction in now insufficient to induce condensed phases, and the crystal melts, resulting in a dramatic increase in local particle mobility ($\tau_{26\,°C}/\tau_{28\,°C} = 4.65$). The $D_{||S}^{S}$ value will eventually reach the hard sphere limit as the attraction is decreased further.

As discussed in Figure 5.2 (Column 2), we can isolate the populations of solid and gas phase particles, thus allowing us to evaluate their dynamics separately. The experimental solid phase $D_{||S}^{S}/D_0$ values are represented by solid blue circles in Figure 5.6 whereas the corresponding gas phase values are indicated by the solid red circles. Following the same procedure for the MC simulations yields the crystal and fluid $D_{||S}^{S}/D_0$ values shown by the open blue and red squares respectively. While all the

values show a consistent trend, the agreement that characterized the combined treatment of the dynamics of the two phases is lacking. A possible cause of this discrepancy could be the limited system size used in the MC simulations.

We have successfully captured the structure and dynamics of the equilibrium phases shown in Figure 5.2. By sensitive direct measurements of the SiO_2 particle-wall and particle-particle interactions and independent verification of the PNIPAM particle size, the forces governing the phase behavior of these systems was explored. Accurate knowledge of these forces yields structure and dynamic simulation data that shows quantitative agreement with the experiments. In this section we have designed a novel colloidal system that allows us to realize reversible equilibrium 2D attraction driven crystallization. We have also shown that we understand the forces that govern phase behavior in these systems and intend to use this knowledge to design intelligent and provocative experiments in the following Sections.

5.4. Conclusions

A novel, purely two-dimensional system that allows tunable, completely reversible interfacial crystallization is presented in this report. Temperature sensitive PNIPAM microgel depletants are used to accurately and reversibly tune interparticle and particle-substrate depletion attraction in purely two-dimensional systems of silica particles levitated over a homogeneous silica substrate and thereby induce reversible crystallization. Direct ETIRM measurements and iMC simulations were used to quantify the tunable nature of the particle-substrate and interparticle depletion potentials respectively. The iMC simulations showed excellent quantitative agreement with VM

measurements of equilibrium phase behavior. We characterized the equilibrium structure and the dynamics of the observed phases and also demonstrated the completely reversible nature of the observed solid-fluid phase transition. This is the first study demonstrating the use of tunable attraction to engineer robust, completely reversible colloidal crystals in pure two-dimensional systems.

6. REVERSIBLE 2D EQUILIBRIUM CRYSTALLIZATION OF ATTRACTIVE COLLOIDS ON ENERGETICALLY PATTERNED SUBSTRATES

6.1. Synopsis

In this Section we used shallow physically etched features on glass substrates to spatially control the crystallization-location of 2D attractive colloids. In Section 5 we used temperature to control the size of PNIPAM microgel nanoparticles, a method which allowed us to exquisitely tune the forces between the larger 2.34μm SiO_2 particles to obtain reversible 2D attractive colloidal crystallization on homogenous substrates. We

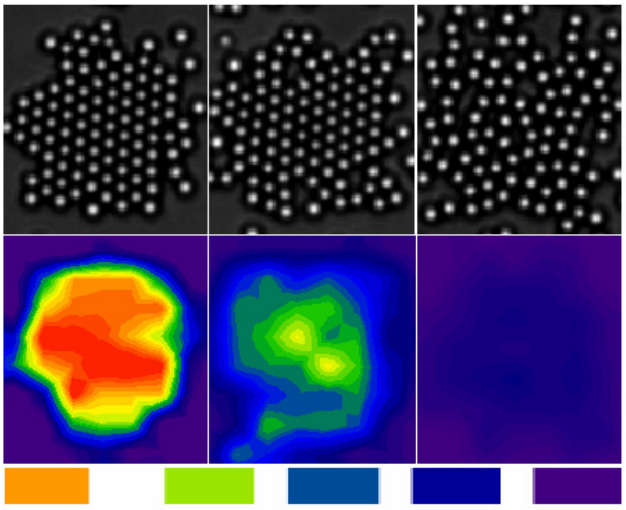

Figure 6.1. (Top) Equilibrium configurations of 2.34μm SiO_2 colloids levitated above a glass substrate with ~310nm (4kT) deep physical features, at temperatures of 20, 26 and 28°C respectively (left-right). (Bottom) Corresponding normalized 2D density profiles across the pattern, with the lowest value (purple) corresponding to a normalized density of 1 and the highest (red) corresponding to a normalized density of 10. Blue, cyan, green and orange correspond to normalized density values of 2, 4, 6 and 8 respectively. In each case the density of the colloidal fluid outside the pattern is used to normalize all density values.

quantified, in that selfsame Section, the 2.34μm SiO_2 interparticle and particle-substrate forces as a function of temperature/PNIPAM microgel particle size and showed that these forces completely explained the phase behavior and dynamics of that system. In this Section, we used shallow (~310nm) physically etched patterns to control the location of crystallization, a detail lacking in the work reported in Section 5.

Apart from the obvious change in the nature of the underlying substrate, the only other difference between the 2.34μm SiO_2/220nm PNIPAM microgel particle systems used in Section 5 and the present Section is the higher 2.34μm SiO_2 area fraction of ϕ=0.431 used in all experiments reported here. As with the results presented in Section 5, the heterogeneous substrate used here showed crystals at temperatures of T=20°C, 22°C, 24°C and 26°C and fluids at 28°C and 29°C (Figure 6.1). For the homogeneous substrates investigated in Section 5 as well as the patterned substrates in this Section, the lowest temperature at which fluids are first observed is T=28°C. Since we have only studied equilibrium states separated by temperature increments of 2°C, direct evidence of the effect of the pattern on the equilibrium phase transition temperature would only be possible for patterns deep enough to allow crystals to persist at T=28°C. Video microscopy experiments were used to record and quantify the phase behavior while Monte Carlo and Stokesian Dynamics simulations were used in conjunction with the already measured and quantified forces (Section 5, Figure 5.3) to explain the influence of the heterogeneous substrate on the equilibrium phase behavior and dynamics of the colloids.

6.2. Introduction

Due to their size and the way they interact with light, colloidal crystals are of tremendous consequence to the proposed fabrication of photonic bandgap devices like waveguides and switches.[3,9] Colloidal crystals instantaneously self assemble in systems with long range electrostatic repulsion,[11] but the resultant ordered phases lack mechanical strength due to the lack of interparticle attraction. This shortcoming can be overcome by employing short-ranged attraction-driven self assembly.[43,63,158] External electric fields are highly effective in inducing order in colloidal systems.[90,91,166,167] However, in the absence of any added attraction holding the colloids in place, the order is lost when the field is removed. Template driven assembly solves the problem of spatial control over crystal location.[82,168,169] However, most research undertaken in this regard has been confined to irreversible deposition.[85] To truly facilitate a way for colloidal crystals to realize their potential applications to photonics, we must have a system that allows the engineering of robust, spatially-controlled, ordered colloidal structures. Herein we suggest the use of equilibrium, depletion-attraction mediated self assembly on physically patterned substrates as a possible solution to this problem.

First suggested by Alfons van Blaaderen,[82] colloidal epitaxy is a method wherein a physical, chemical or biomolecular patterned substrate is used to direct the crystallization of sedimenting colloids. Yodh and coworkers used this approach in conjunction with a fixed depletion potential to form 1D, 2D and 3D depletion crystals on periodically patterned substrates in equilibrium with bulk colloids.[87] The first comprehensive investigation into the influence of the patterned substrate on the structure

and dynamics of an interfacial colloidal fluid was performed by Bahukudumbi and Bevan for a purely repulsive 2D system of 2.34μm SiO_2 colloids in equilibrium with a physically patterned substrate.[88] Herein, we report the first experiments that combine tunable depletion attraction and physical substrates to engineer reversible, spatially controlled 2D colloidal crystallization.

In this work, we use video microscopy measurements in conjunction with Monte Carlo and Stokesian dynamic simulations to systematically quantify the effect heterogeneous patterned substrates have on the structure and dynamics of attractive colloidal particles. Specifically, we demonstrate the ability of a patterned substrate to control the spatial location of colloidal crystallization. From video microscopy measurements we were able to quantify the role the pattern has in inducing periodic enhancements in local density for set interparticle and particle-substrate interaction forces and how these enhancements evolved with changes in these solvent quality condition-controlled forces (Figure 6.1). We utilized our comprehensive understanding of this system developed from experiments and simulations reported in Section 5 to quantify the depth of the physical features (~310nm) and completely verify the experimentally observed structure and dynamics of attractive colloids on these heterogeneous substrates.

6.3. Results and Discussion

6.3.1 Experiments

The sample solution consisted of a mixture of 2.34μm SiO_2 colloids and PNIPAM (for diameters refer to Table 5.1) microgel particles dispersed in a 1.5mM NaCl solution. The two types of particles were mixed in a ratio that yielded a 2.34μm SiO_2 colloid area fraction of ϕ=0.431 and a PNIPAM microgel particle volume fraction of 24%. As in Section 5, temperature values of T=20°C, 22°C, 24°C, 26°C, 28°C and 29°C were investigated. It is important to note that the experiments performed in Sections 5 & 6 have the same salt concentration and PNIPAM microgel particle volume fraction and as a result, at a given temperature, are subject to the same interparticle and particle substrate forces (Figure 5.3). All the forces at work in the system investigated in this Section are therefore already known. For a detailed explanation of the measurement and effects of these forces, refer to Section 5.

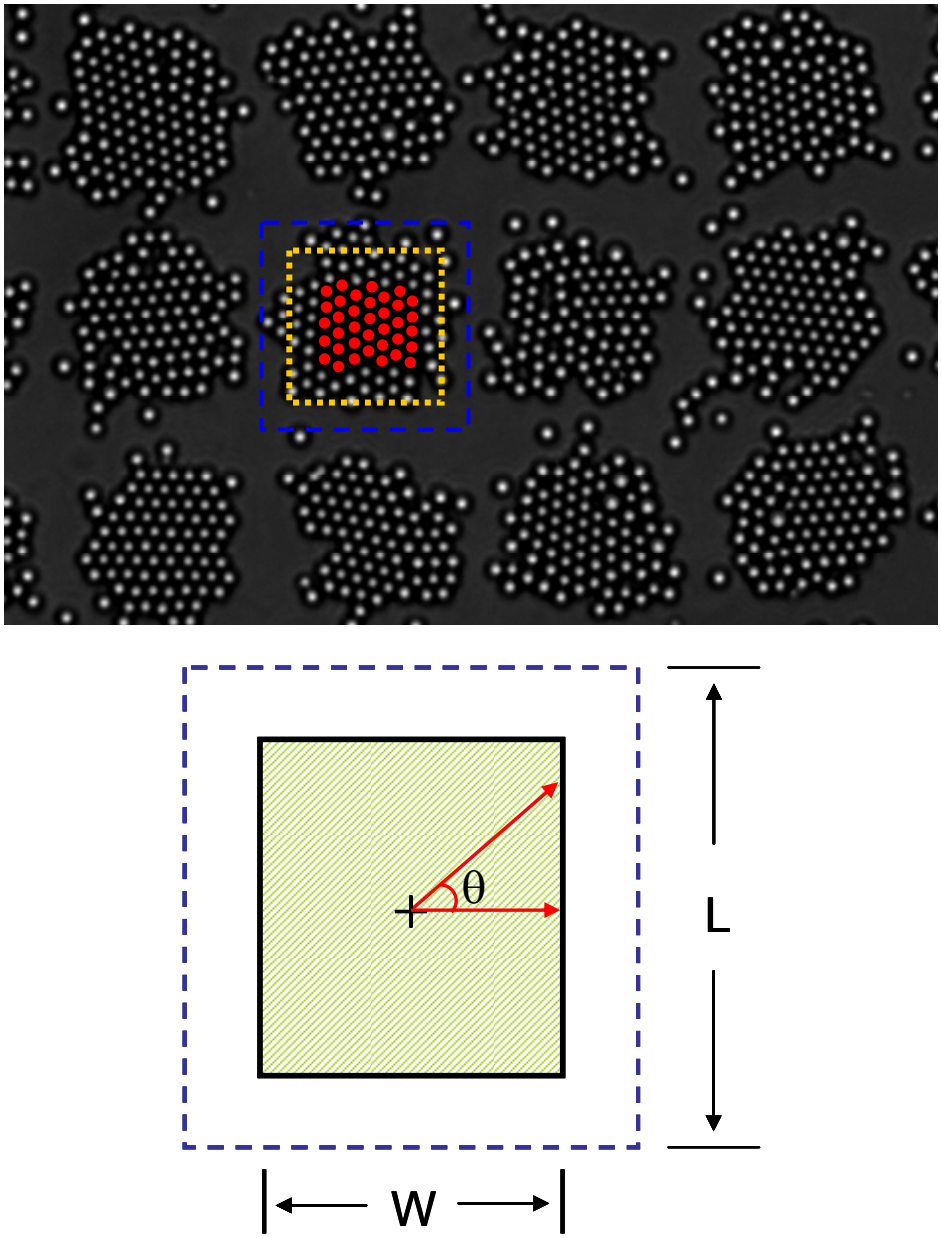

Figure 6.2. (Top) An experimentally observed configuration of 2.34μm SiO_2 colloids levitated over an array of physical patterns. The blue and yellow boxes correspond to the fMC simulation box and pattern size respectively (bottom). The 36 colloids overlaid in red represent a simulated equilibrium fMC configuration from which dynamic information is obtained via Stokesian Dynamics.

6.3.2 Brief Description of Physical Patterns

All experiments reported here were performed on glass microscope slides with ~310nm deep physical features etched into them. The etching procedure resulted in an array of nominal 22μm×22μm×310nm ($W \times W \times h_{depth}$) features spaced by 15μm (Figure 6.2). It is important to clarify that the dimensions of the physical features are not known before hand. Prior knowledge of interparticle and particle-substrate interactions (Section 5, Figure 5.3) allows the use of fMC simulations to obtain the dimensions of the features. The details of this procedure are explained in Section 6.3.3.

The glass substrates and etch procedures used in this work exactly match those used by Bahukudumbi and Bevan who report parabolic cross sections for physical features obtained by this procedure from AFM studies.[88] We can therefore safely assume a parabolic cross section for patterns used in this work. The potential energy profile across any radial section of these patterns takes the form $\frac{u(x,y)}{kT} = 4\frac{u_{welldepth}}{kT}\frac{(x^2+y^2)}{\left(W(\theta)\right)^2} - u_{welldepth}$, where $\frac{u_{welldepth}}{kT} = h_{depth}\left(\frac{4}{3}\pi a^3 \Delta\rho g\right)$. Here $\Delta\rho$ is the colloid and medium density difference, g is the acceleration due to gravity, $W(\theta)$ is the angle dependent width of the feature ($W(0)$, $W(\pi/2)$, $W(\pi)$, $W(3\pi/2)=W$) and h_{depth} is the depth of the feature at its center where it is at its deepest (Figure 6.2). From fMC simulations we find $\frac{u_{welldepth}}{kT} = 4$, which corresponds to an h_{depth}=310nm.

6.3.3 Equilibrium and Dynamic Property Simulations

Verification of the experimentally observed equilibrium-phase structure and dynamics on patterned substrates was achieved by the use of fMC and Stokesian Dynamics simulations respectively. A basic assumption inherent to our treatment of the system studied herein is that all features (Figure 6.2) are identical. The inter-pattern spacing allows colloid density to reach bulk values between patterns, justifying the use of a single pattern simulation study equivalent to the 4×3 array studied experimentally and represented in Figure 6.2. We will now explain in detail how we setup the fMC simulation.

Figure 6.2 (top) is an experimentally observed colloid configuration at an area fraction of ϕ=0.431 that we wish to verify via simulation. The simulation box (Figure 6.2, bottom) is specified such that its size (L=30μm) is the center-to-center separation between the patterns in Figure 6.2 (top) and it contains a square feature of width (W=22μm) within it. The square feature is parabolic along all radial sections taken across it. Fixing ϕ and L also fixes the number of particles $N = \frac{\left(\frac{L}{R}\right)^2 \phi}{\pi} = 100$, where R=1.1mm is the radius of the SiO_2 colloids. All (*NVT)* fMC simulations reported in this work were performed for ϕ=0.431, L=30μm, W=22μm and N=100. These simulation box dimensions are then overlaid on an experimental image to clarify the setup of the modeling study (Figure 6.2 (top), yellow and blue boxes). We then iterate over the value of pattern depth (h_{depth}) to get density profiles that match our experiments.

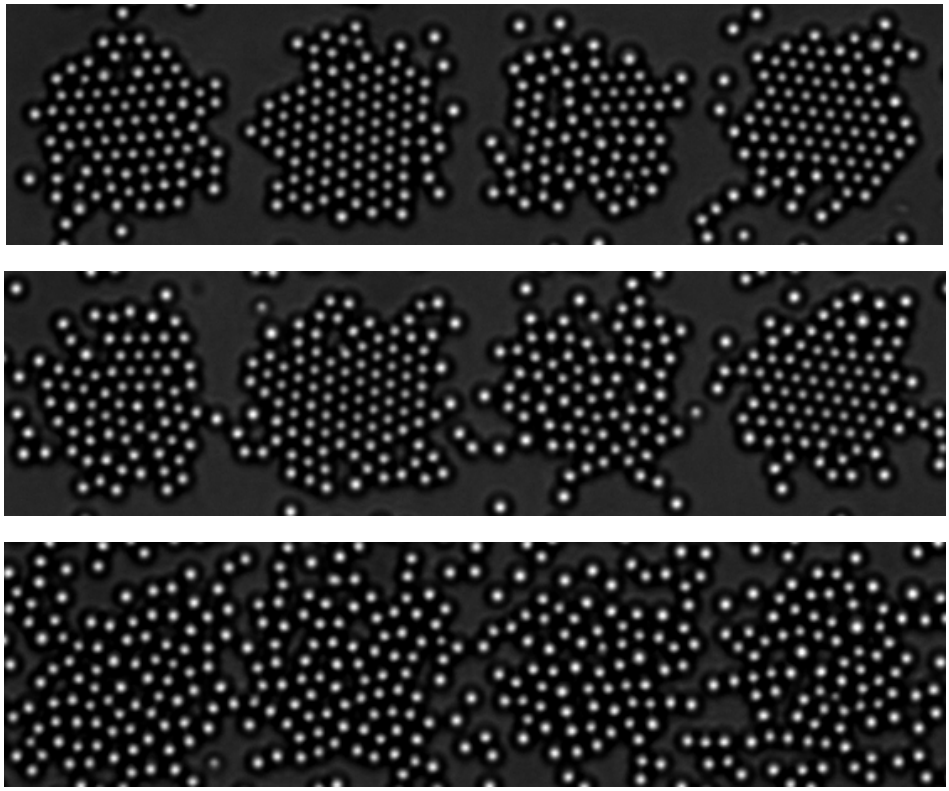

Figure 6.3. Experimentally observed configurations of 2.34μm SiO_2 colloids levitated over the same row of physical features at temperatures of T=20°C (top), 24°C (center) and 28°C (bottom) respectively.

Simulations aimed at verifying the experimentally observed dynamics are further simplified by treating the system shown in Figure 6.2 as homogenous over the area occupied by the 36 red particles. We already know the values of the enhanced colloidal density (ϕ) within these features at every temperature from experiment (Figure 6.1). Thus at a given temperature, fixed N and ϕ values fix the values of simulation box size, L. We run fMC simulations for 36 particles with temperature dependent L values and then use Stokesian Dynamics to obtain information about the diffusive behavior of the

colloids over distances less than their radii. The property that we obtain from the Stokesian Dynamics simulations is the lateral short-time mean squared displacement, D_S^S.

6.3.4 Interfacial Colloids and Heterogeneous Substrates

Figure 6.3 shows equilibrium configurations of 2.34μm SiO_2 colloids interacting with exactly the same four underlying features at temperatures of T=20°C (top), 24°C (center) and 28°C (bottom) respectively. The features are filled with crystals at 20°C and 24°C as opposed to 28°C, where a fluid state exists. We already know, from Section 5, that this transition is due to the fact that the interparticle depletion attraction decreases as the temperature is raised (Figure 5.3). It is clear that the underlying features are not deep enough to cause crystallization of a hard sphere system at this area fraction (ϕ=0.431) because even for the case of moderate interparticle attraction (T=28°C, Figure 6.3 (bottom)), no crystals exist.

It is however important to note that the underlying features are able to control the spatial location of the crystals. For the area fraction used, the highest values of interparticle attraction (T=20°C and T=22°C) yield crystals that completely filled in the feature but did not extend across them. While lower area fractions do not yield crystals that fill in the feature entirely, higher values would eventually result in a loss of the feature specific nature of the crystals. For features entirely filled with crystals, the addition of extra colloids will add ordered colloidal shells around the periphery of the crystal phase until adjacent patterns start getting bridged. This question is dealt with, in

some detail in the Section 7. Another important detail is the lack of consistent crystal quality from feature to feature.

Figure 6.3 (top, L-R) clearly shows that the colloids form more ordered structures in patterns two and four than in the first and third. The higher size non-uniformity of particles concentrated in the first and the third features as compared to the second and the fourth is a possible contributing factor. It is also important to note that while all features were formed in a single etch, it is unlikely for all of them to be exactly the same. It is easy to see how a feature with a less uniform cross section would be less conducive to crystallization, an observation crucial for later discussions that attempt to quantify and explain the equilibrium behavior shown in Figure 6.3. As the temperature is raised, the size of the pattern-localized crystals diminishes. At T=28°C, we observe no crystalline structures. Instead an 2D inhomogeneous fluid is observed. The spatial in-homogeneity is a result of the underlying patterned substrate.

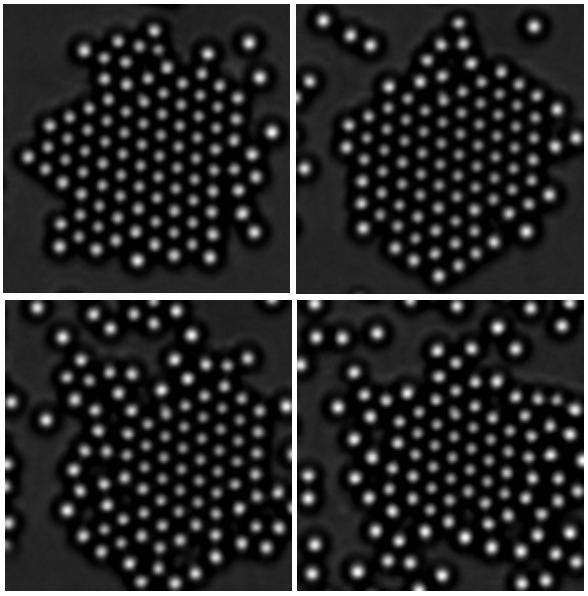

Figure 6.4 (Left-Right) Structural rearrangements in a pattern localized crystal due over a period of ~10mins at temperatures of T=20°C (top) and T=26°C (bottom). Note that exactly the same area is shown in all pictures.

Figure 6.4 highlights another important characteristic of the systems studied in this work. Over a period of ~10mins, the pattern localized crystal at a temperature value of T=20°C shows a significant change in its overall shape. This change can be attributed entirely due to the diffusive rearrangements of particles within the crystal. Particles that form the periphery of the crystal diffuse and rearrange more readily that those at inner core of the crystal phase, such as those represented by red circles in Figure 6.2. This observation is extremely important for the discussions that follow in which an attempt is made to quantify and explain the dynamics of the phases shown in Figure 6.3.

For the area fraction (ϕ=0.431) investigated in this work, at T=20°C, the colloids assemble into crystalline phases that completely fill-in the features (Figure 6.3 & 6.4,

top). In this case the periphery of the crystal and the perimeter of the feature are the same. As the temperature is raised, the drop in the interparticle attraction (Figure 5.3) results in this crystal "periphery" moving inward as the crystals shrink, decreasing the ratio of the "peripheral" to "core" particles. Figure 6.4 (bottom) illustrates this point perfectly and shows the still rearranging and feature localized but considerably shrunk crystal at T=26°C. The next higher temperature value of T=28°C yields a fluid phase both inside and outside the pattern (Figure 6.3, bottom). This kind of solid-fluid transition is characteristic of 2D systems and is also observed in the results reported in Section 5.

Figures 6.3 and 6.4 both show how the decreasing interparticle attraction changes the structure and dynamics of the equilibrium phases that result. The reason we compared T=20°C and T=26°C (Figure 6.4) is that shrinkage in the pattern localized crystals is large enough that visual comparison alone is enough to discern the differences between the two phases, a fact that while present in the crystals at T=20°C and T=24°C (Figure 6.3) is too subtle for visual comparison. The remainder of this Section is dedicated to following through with the quantitative analysis and verification of the differences in the structure and dynamics of the three equilibrium phases represented in Figure 6.3.

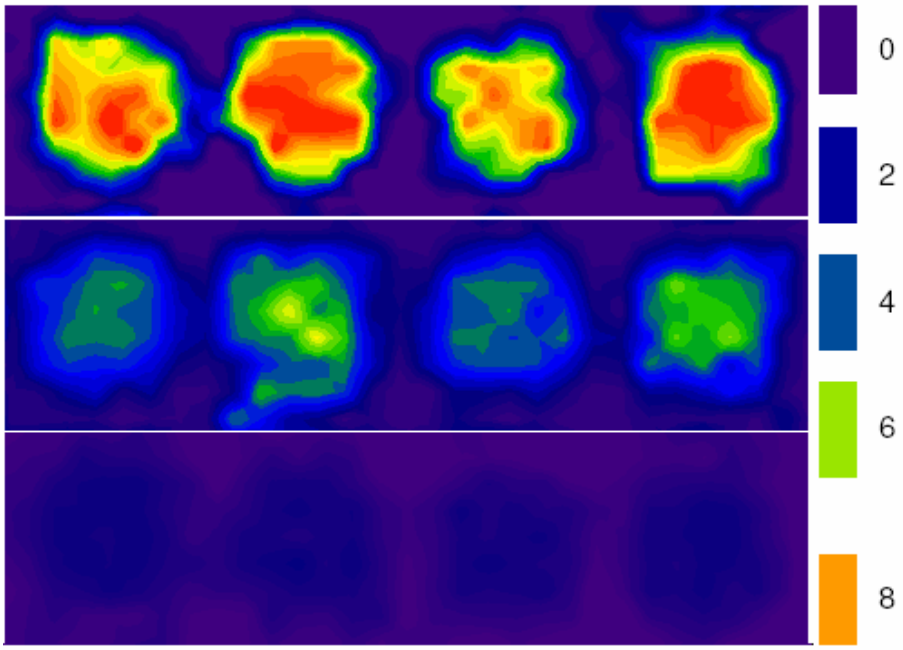

Figure 6.5 Experimental, time-averaged and normalized 2D colloid density, $\rho(x,y)/\rho_{out}$, at T=20°C (top), T=24°C (center) and T=28°C (bottom), from centers of colloids whose single equilibrium snapshots are represented in Figure 6.3.

6.3.5 Tunable Density Enhancements at Feature Specific Locations

By tracking the centers of the 2.34μm SiO_2 colloids diffusing over the pattern surface topography we were able to characterize the time averaged equilibrium distributions of these colloids as 2D density profiles, $\rho(x,y)/\rho_{out}$. ρ_{out} is the average density of colloids outside the geometric confines of the features shown in Figure 6.3. The fact that both the etched feature depth and the normal excursions of the colloids are small compared to the diameter of the particles (2.34μm), throws light on the quasi-2D nature of the system and suggests that the 2D $\rho(x,y)/\rho_{out}$ is effective in capturing the equilibrium sampling of the surface by the diffusing colloids. The first step in

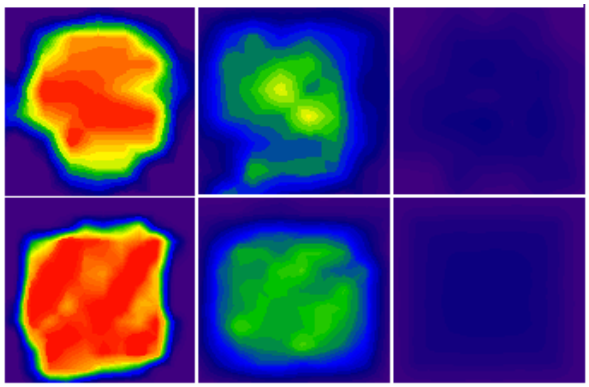

Figure 6.6 Normalized 2D colloid density, $\rho(x,y)/\rho_{out}$, at T=20°C (left), T=24°C (center) and T=28°C (right), from experiment (top row) and simulation (bottom row). The scale is the same as that in Figure 6.5.

constructing the experimentally measured $\rho(x,y)/\rho_{out}$, was locating the x,y coordinates of the diffusing colloids to within ~95nm in 10^4 images. The second step involved construction of 2D population histograms on a grid of ~6μm^2 pixels. The final step involved normalizing by the average number density in the area not occupied by the features, ρ_{out}.

Figure 6.5 shows the experimentally measured $\rho(x,y)/\rho_{out}$ for temperature values of T=20°C (top), T=24°C (center) and T=28°C (bottom), the representative equilibrium snapshots of which are shown in Figure 6.3. As mentioned earlier, the differences between the equilibrium structure in the crystal states is much more obvious in Figure 6.5 than in Figure 6.3. Figure 6.5 shows that for T=20°C (top), the density within the features is enhanced to as much as 10 times the average value outside it. At T=24°C (center) however, this value drops to 6 times the average density outside the features. Finally in the case of the fluid at T=28°C (bottom), the density within the feature is only

about 2 times the average values outside the feature. It is important to note that each of the cases in Figure 6.5 has a different value of ρ_{out}.

The experimentally measured $\rho(x,y)/\rho_{out}$ show that for a fixed (on average) total number of diffusing colloids levitated over features of fixed depth, as the attraction between the particles is increased, the number of particles within the features increases at the expense of the colloids diffusing outside to the point where we observe crystals within the features. This effect is supported by the images we see in Figure 6.3 wherein the density of the colloids outside the patterns increases as the temperature is raised. This means that with increasing attraction, a given colloid will start to sample locations within the feature more. The effect of the underlying features is evident in the limit of low attraction (T=28°C) where the pattern sets up a 2D inhomogeneous fluid. In order to verify the experimental results against knowledge of temperature tunable interparticle depletion attraction information obtained in Section 5, we performed fMC simulations.

6.3.6 Verification of Experimental Density Profiles via fMC

Figure 6.6 shows excellent agreement between $\rho(x,y)/\rho_{out}$ obtained from experiment (top) and simulation (bottom). The simulations were performed as per the procedure described in Section 6.3.3. The interparticle interaction values used in these simulations are shown in Figure 6.7 and showed excellent agreement with the previously measured values in Section 5 (Figure 5.3d) for the fluid case (T=28°C). The slight discrepancy seen for the crystal cases in Figure 6.7 stems from the ideal nature of the simulation features/particles as opposed to their experimental counterparts.

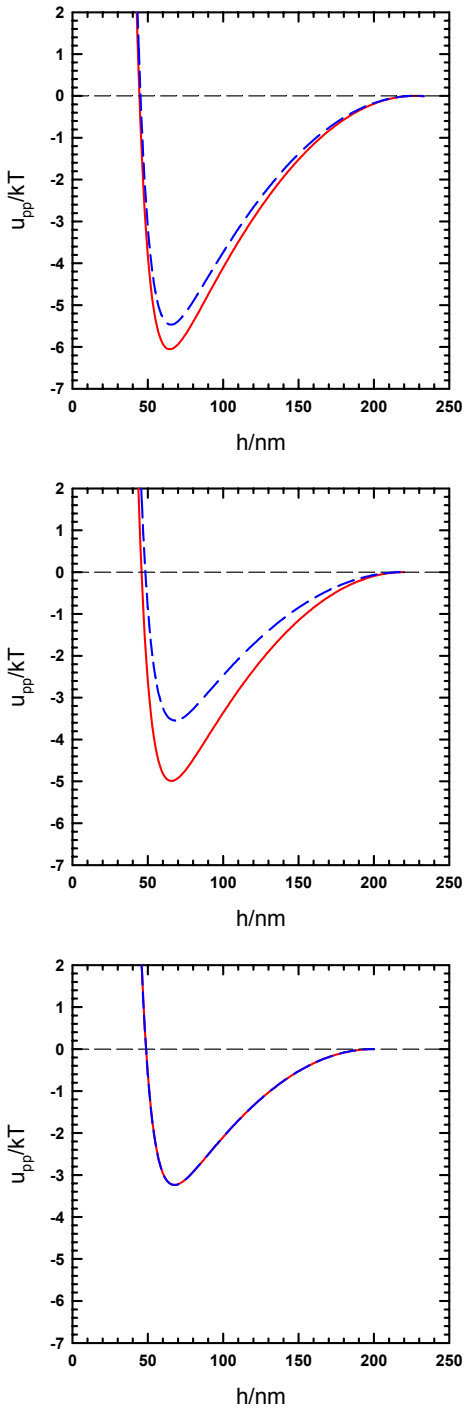

Figure 6.7 Interparticle attraction (blue curves) used in simulations at T=20°C (top), T=24°C (center) and T=28°C (bottom) compared with those obtained from VM and fMC on homogeneous substrates in Section 5, Figure 5.3d (red curves).

Packing efficiency and likewise crystal quality are highly affected by polydispersity and feature non-uniformity. The simulations are not plagued by these problems and as a result, for equal feature depth and interparticle attraction, would allow higher packing density than etched features used in experiments. The fluid phase is inherently more unaffected by these non-idealities and therefore shows excellent agreement.

Figure 6.8 compares cross sections of $\rho(x,y)/\rho_{out}$ for simulations with N=100, ϕ=0.431, L=30μm, W=22μm and h_{depth}=310nm (u_{well}=4kT) (Figure 6.6, bottom) with experiment (Figure 6.5) for T=20°C (top), T=24°C (center) and T=28°C (bottom) respectively. In each case the cross section is taken at exactly the same horizontal location for both the simulation as well as experiment. Figure 6.8 shows good agreement between experiment (red curves) and simulation (blues curves) for all three cases shown therein. As with Figures 6.5 and 6.6, Figure 6.8 shows that as interparticle attraction is increased, features of fixed depth become progressively more and more concentrated with colloids.

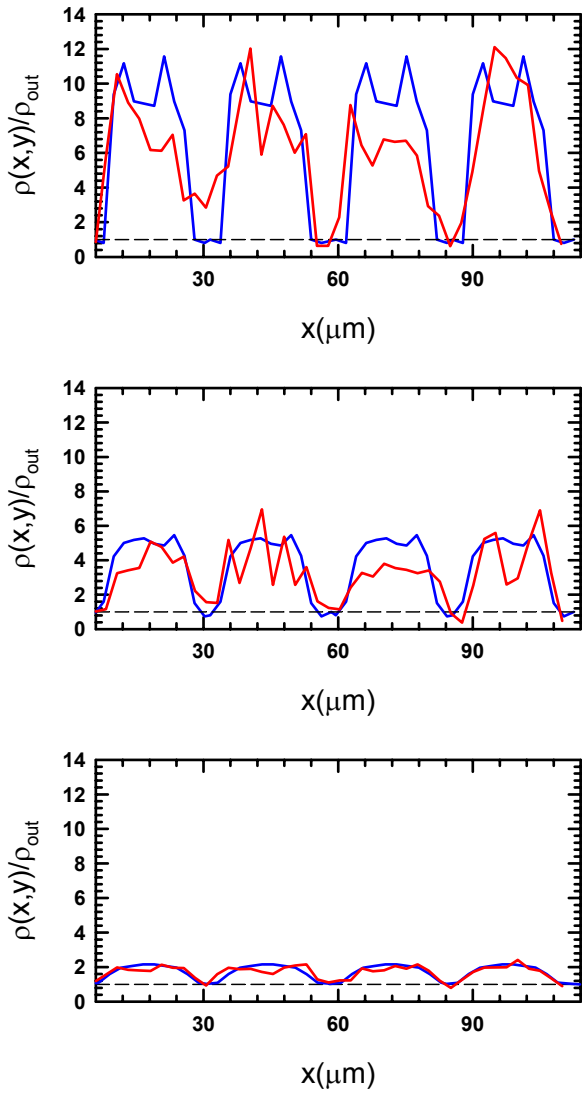

Figure 6.8 $\rho(x,y)/\rho_{out}$, at T=20°C (top), T=24°C (center) and T=28°C (bottom), for a horizontal cross section taken across the center of the features from experiment (red) and simulation (blue). The dashed line represents a $\rho(x,y)/\rho_{out}$ value of 1.

It is of some merit however to look carefully at the consistency in enhancement of density from pattern to pattern. As noted previously from purely visual observation in Figure 6.3 (L-R), patterns two and four appear to be more conducive to crystallization

than one and three. Figure 6.8 quantifies this claim by clearly showing greater density enhancements in the cross sections of features two and three and one and two for the two crystalline cases (T=20°C and T=24°C). For the fluid case at T=28°C (Figure 6.8, bottom) however these differences are not apparent. The fact that these compromised values of density enhancements manifest only for the crystal cases; states that are especially sensitive to the degree of uniformity causes us to believe that the non-uniformity of the feature and the polydispersity of the colloids that concentrate within it result in the inconsistencies seen in Figure 6.8.

Boltzmann's inversion of all the data in Figure 6.8 helps explain the temperature dependent behavior of the system. For an infinitely dilute system of colloids ($\phi \to 0$), Boltzmann's equation, $u(x,y) = -\ln\left[\rho(x,y)\right]$ directly relates the potential energy of the underlying feature with density profile of the diffusing colloids. Using Boltzmann's inversion on our concentrated systems yields a position dependent potential of mean force, *w(x,y)*. For ease of viewing, Figure 6.9 represents the Boltzmann's inversion of only the fMC $\rho(x,y)/\rho_{out}$ values shown in Figure 6.8 (blue curves).

Figure 6.9 shows that at $\phi \to 0$, a single 2.34μm SiO_2 colloid would need to escape a 4kT free energy well to diffuse over the entire surface of the pattern used in this work. For 100 such colloids at an area fraction of ϕ=0.431 diffusing over the same 4kT deep feature, the situation changes. In this case, a single colloid at T=28°C, would experience an interparticle attraction of ~3kT (Figure 6.7, bottom) and as a result of multiparticle packing effects within the feature (Figures 6.3, 6.5 and 6.8, bottom), would

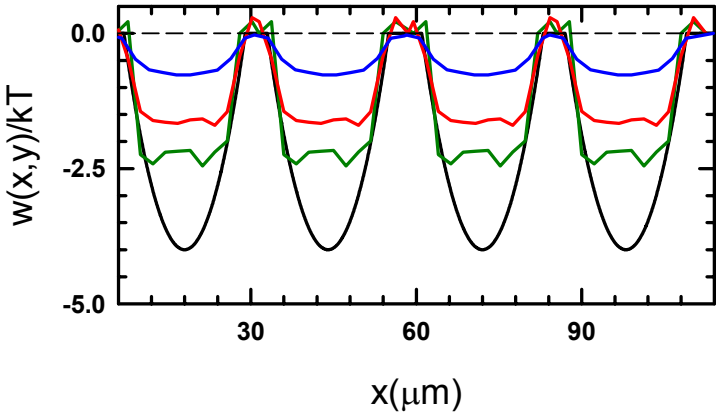

Figure 6.9 w(x,y)/kT, at T=20°C (green), T=24°C (red) and T=28°C (blue), obtained from Boltzmann inversions of the blue curves in Figure 7.8. The black curve represents the potential energy landscape of physical features that are ~310nm deep.

only need to escape a 0.8kT free energy well (Figure 6.9, blue curve) to diffuse over the entire surface. As the temperature is decreased, the increased interparticle attraction (Figure 6.7) causes more colloids to sample the features (Figure 6.8), thus depleting the average number of diffusing colloids outside the features. Boltzmann inversions of these density profiles mean a single colloid would need to escape 1.6kT and 2.4kT free energy wells at T=24°C and 20°C respectively.

6.3.7 Dynamics of the Equilibrium Phases

Ensemble-averaged Mean squared displacements (MSDs) over all colloids were calculated from the experiments at each temperature, from which short time self-diffusivities, D^S_S, were obtained. Figure 6.10 shows the experimentally calculated D^S_S/D_0 values for temperatures of T=20°C, 22°C, 24°C, 26°C, 28°C and 29°C (black

circles). As with the data in Section 5, D_0 in this case is the Stokes-Einstein diffusivity ($D_0=kT/6\pi\mu a$) for a single 2.34μm SiO_2 particle diffusing through a solvent consisting of 24% PNIPAM microgel hard sphere depletants in water. The error bars are due to the uncertainty in determining the low-shear limit viscosities for hard sphere dispersions.

The dashed line in Figure 6.10 is the D^S_S/D_0 trend followed by the 2.34μm SiO_2 colloids diffusing over a homogeneous substrate in Section 5. The diffusivities obtained from experiments presented in this Section agree well with the general trend seen in on homogeneous substrates for all temperatures except at T=26°C. The homogeneous substrate data-trend suggests a transition temperature of around T=27°C (dashed line). This means that at T=26°C, the system is a mere 1°C away from undergoing a solid-fluid transition. We know the substantial difference that exists between the D^S_S/D_0 values for a crystal and a fluid. It is therefore entirely possible a slight increase in the temperature above the measured value of T=26°C caused either by fluctuations about the set point or by a slightly compromised thermocouple attachment could result in the observed discrepancy.

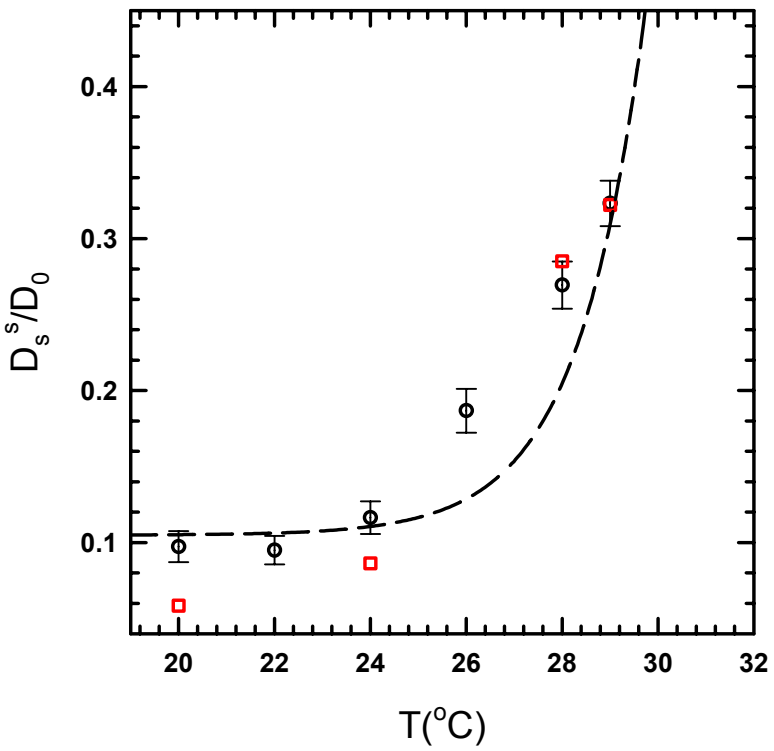

Figure 6.10 Temperature dependent, experimental, normalized, short-time lateral self-diffusivities (D_S^S/D_0) averaged over all observed particles (black circles) compared with those from simulations (red squares). The dashed curve is the trend followed by similar experiments performed on homogeneous substrates in Section 6.

Comparing the D^S_S/D_0 values obtained from the experiments, it is observed that increasing interparticle attraction (decreasing temperature), decreases D^S_S/D_0. This trend is best explained by Figure 6.8. As the interparticle attraction is increased, the number of nearby colloids within the pattern features increases, causing increased hindering on account of increased the hydrodynamic interactions due to greater numbers of neighbors. D^S_S/D_0 was also obtained from Stokesian Dynamics simulations via the procedure described in Section 6.3.3 (Figure 6.10, red squares). The area fractions and simulation

box sizes over which the simulations are carried out are ϕ=0.9163 and L=6 at T=20°C and 24°C, ϕ=0.6091 and L=7 at T=28°C and ϕ=0.5522 and L=8 at T=29°C. The interparticle interactions are shown in Figure 6.7 (blue curves).[107]

The experimental and simulation data display excellent agreement for the two fluid cases at T=28°C and T=29°C (Figure 6.10). For the two crystal cases however, the simulated D^S_S/D_0 values are lesser than their experimental counterparts with the values at the lower temperature being more unlike. This discrepancy can be explained by fact that the experimental D^S_S/D_0 values are determined by averaging over all colloids diffusing over the pattern represented in Figure 6.2 whereas the simulations calculate the D^S_S/D_0 over a much more specific area (Figure 6.2, red circles). We therefore miss out on the diffusive behavior of the particles outside this zone, a factor that does not affect the fluid cases due to the lower density enhancements therein.

For the crystal cases however, not capturing the diffusive behavior of colloids on the crystal periphery, major contributors to crystal rearrangement; and colloids outside the features could easily result in a lower simulation value than is expected. Another possible cause of the discrepancy is the fact that not all features in the experiments yield crystals of equivalent quality (Figure 6.8), a problem that does not plague simulations. It is easy to observe from Figure 6.8 (bottom) that the fluid cases would be less affected by inconsistent feature characteristics than the temperatures for which crystals exist.

Previous experiments on the diffusive behavior of submonolayer 2D repulsive colloids on physically patterned features showed that for a fixed feature depth, increased particle concentration resulted in a lower D^S_S values but higher D^S_L. This behavior was

modeled as a parallel resistive mechanism, $D_S^L = D_S^S\left[\exp\left(\Delta w / kT\right) + 2\phi g\left(2a_{eff}\right)\right]^{-1}$ in which Δw is obtained directly from Boltzmann inversions of the density profiles and $2\phi g(2a_{eff})$ accounts for particles moving through their coordination shell within the quasi-2D fluid parallel to the surface.[88] For the attractive systems studied in this report, as the interparticle attraction is increased, the local particle density within the features increases, thus decreasing D^S_S. However, this also increases both Δw and $2\phi g(2a_{eff})$ too, thus causing D^S_L decrease as well. For systems of colloids diffusing over patterned substrates, we therefore anticipate both D^S_S and D^S_L to decrease as the interparticle attraction is increased.

6.4. Conclusions

We have demonstrated how ~310nm physical features can be used to control the spatial location of colloidal crystallization. Using temperature tunable depletion attraction, we were able to obtain reversible 2D crystallization on these patterned substrates with the location of crystal growth always confined to the features. We also characterized and explained the structure and the dynamics of the equilibrium phases that assembled over these underlying substrates at each temperature. For a fixed underlying feature depth, increasing interparticle attraction concentrates more and more colloids within the feature at the expense of the fluid outside until crystallization occurs. For systems of colloids diffusing over patterned substrates, we found that both D^S_S and D^S_L decrease as the interparticle attraction increases.

7. 2D CRYSTALLIZATION ON PATTERNED SUBSTRATES: A SIMULATION STUDY

7.1. Synopsis

The last set of studies we would like to present in this dissertation builds on the information obtained from the experiments and simulations reported in Sections 4-6. The primary objective of this section is to isolate conditions under which physical or chemical patterns are completely filled with hexagonally close packed crystal phases (Figure 7.1). We investigated two different types of patterns: channels and hexagons. For each case, we studied two different pattern cross-sections: parabolic and square. As will be explained in later in the Section, parabolic wells are representative of physical

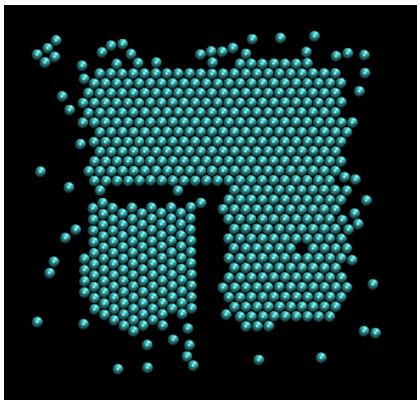

Figure 7.1. An equilibrium configuration of colloids levitated above a pattern with a square cross-section and a well depth of 12kT. The interparticle attraction depletion potential minimum is 4kT.

patterns obtained by HF etching whereas square wells behave like chemical patterns obtained by gold vapor deposition.

All simulations reported in this section are pure-2D MC simulations. We investigated how pattern size, shape and depth affect the ability of a system to crystallize. In addition, we also investigated the influence of area fraction and interparticle depletion attraction on pattern induced crystallization. The aforementioned studies were used to construct phase plots which were then used to achieve crystallization on a 2D projection of the famous "micropolis" circuit,[9] thus motivating the potency of this system in achieving tunable, reversible and spatially controlled 2D crystallization with potential applications to photonics.

7.2. Introduction

In addition to being excellent model systems for freezing-melting studies,[2] colloids, when in an ordered state, find applications in the areas of optical filters, switches and photonic bandgap materials.[3,9] One of the biggest challenges in colloidal science is the engineering of robust, large, single crystals. To achieve this goal, van Blaaderen suggested the use of colloidal epitaxy,[82] wherein a physically patterned substrate was used to direct the crystallization of slowly sedimenting colloids. This approach has since been extended to a variety of patterned substrates ranging from physical[170-172] to chemical[173,174] to biomolecular[175,176] in nature.

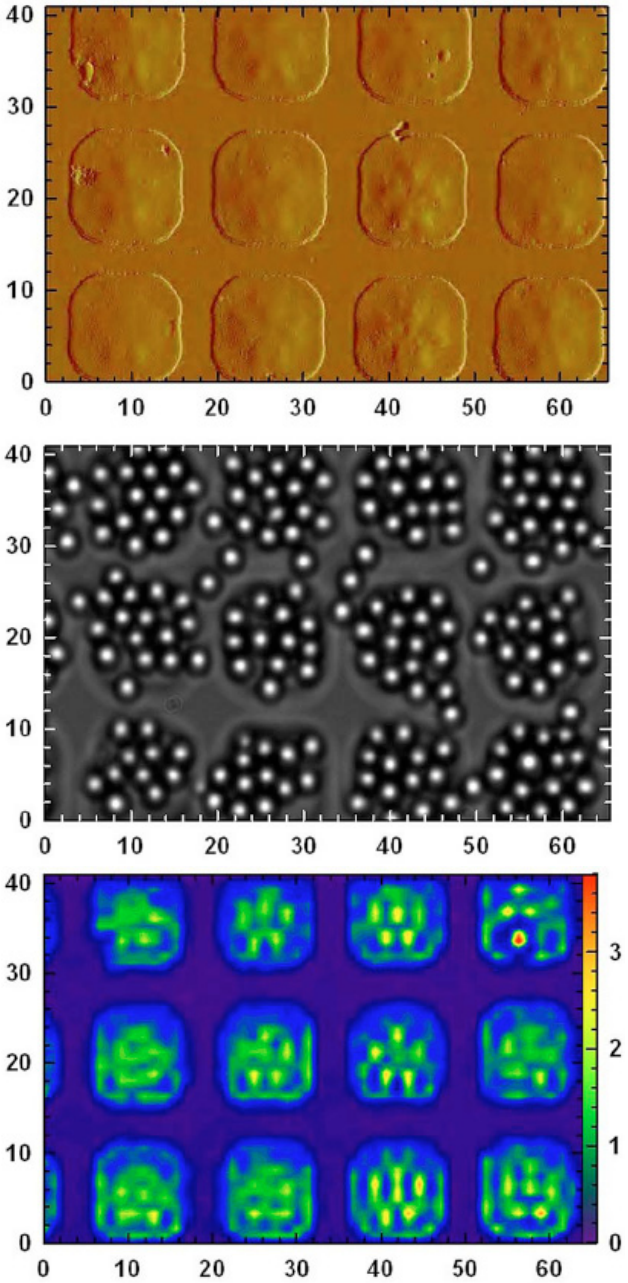

Figure 7.2. (Top-bottom) a) AFM image of a physically patterned glass microscope slide. b) Equilibrium configurations of 2.34μm SiO_2 colloids leviatated above the pattern. c) Periodic density variations induced in the repulsive colloidal fluid due to the pattern shown in (a) and (b). The color bar represents the scale for the time averaged colloid density $\rho(x,y)$.[88]

Bahukudumbi and Bevan studied the 2D diffusive behavior of two different concentrations of repulsive 2.34μm SiO_2 particles over a physically patterned substrate with a parabolic cross-section and were able to quantify both the density distributions and the dynamics of these repulsive systems, thus yielding valuable insights into the role templates in inducing periodic spatial inhomogeneities in a colloidal fluid (Figure 7.2).[88] Similarly fabricated physical patterns were used to study template controlled crystallization in attractive systems. In Section 6, we demonstrated the use physically patterned substrates to control the spatial location of crystals. In the current Section, we investigate the effects of feature size, cross-section and depth on the control of interfacial crystallization for a range of colloid area fractions and interparticle attraction.

Herein, we report simulations performed on patterns designed to mimic both physical (parabolic cross-section) and chemical (square cross-section) templates. We also studied isotropic (hexagonal) and non-isotropic (channel) patterns. By transforming the pattern feature depth scale to an integrated total energy scale, it was possible to compare the different patterns. As expected, area fraction plays an important role in determining whether the entire pattern is filled-in with a single colloidal crystal phase. By constructing phase plots from the data obtained, we were then able to specify, for any pattern geometry or nature, conditions that would yield large single crystals.

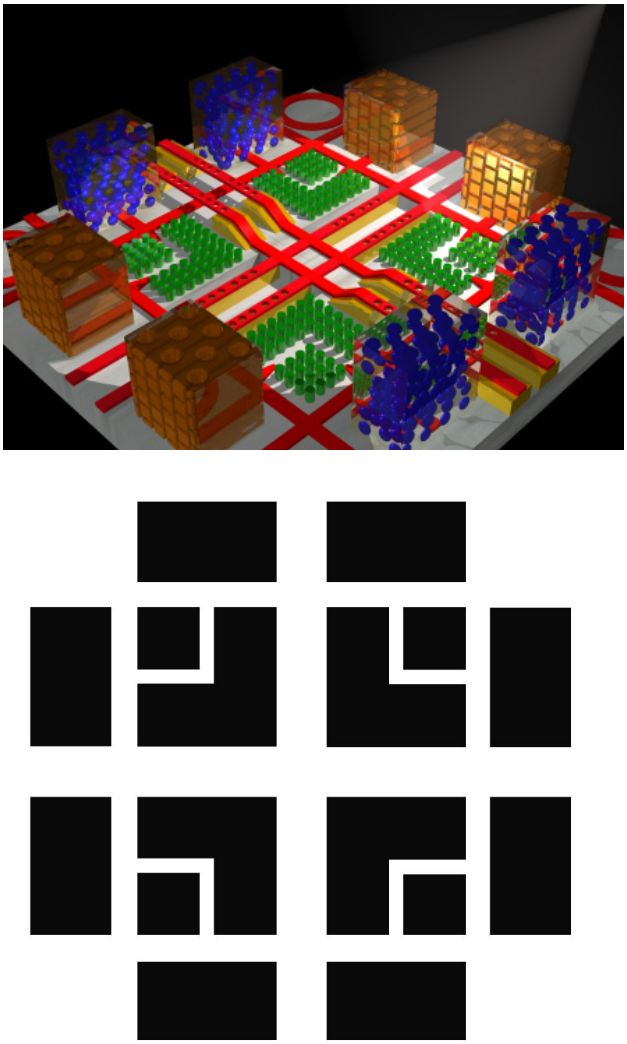

Figure 7.3. (top) A computer rendering of an all-optical integrated circuit based computer using photonic band gap materials engineered using colloidal particles and its simplified 2D fingerprint (bottom).[9]

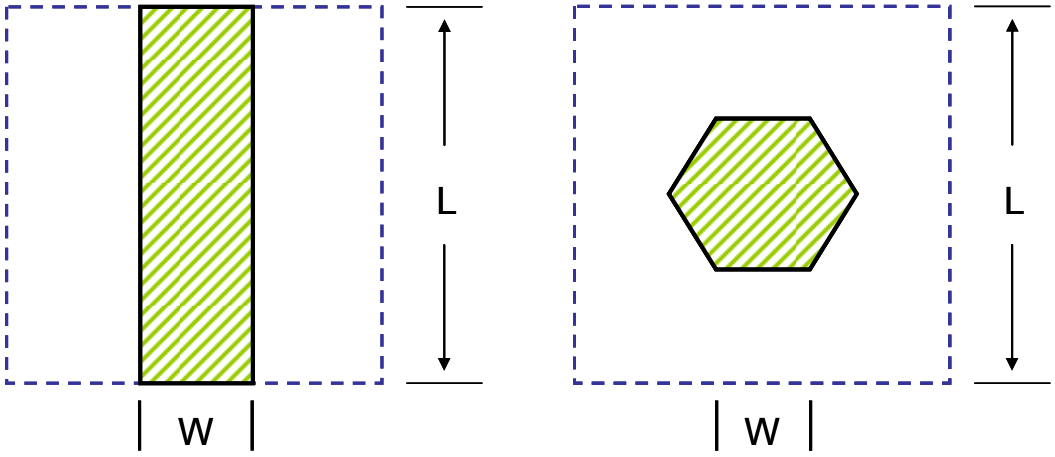

Figure 7.4. (left) Schematic representation of the simulation box (blue line) and the channel pattern (green). (right) Schematic representation of the simulation box (blue line) and the hexagonal pattern (green).

7.3. Results and Discussion

7.3.1 Description of Pattern Geometry and Cross-Section

Figure 7.3 throws light on the application of large robust single colloidal crystals to the field of photonic devices. For the 2D systems studied in this dissertation, we have already demonstrated in Sections 5-6, the ability to reversibly control not just the equilibrium phase by the use of tunable attraction but also its spatial position by templating/energy landscapes. In this Section we wanted to apply that knowledge to engineer a 2D equivalent of the colloidal integrated circuit shown in Figure 7.3. To achieve crystallization on this template in an informed, knowledgeable way, we combined our accumulated knowledge of solvent quality conditions, tunable potentials and energy landscapes with an investigation into how the geometries of the underlying

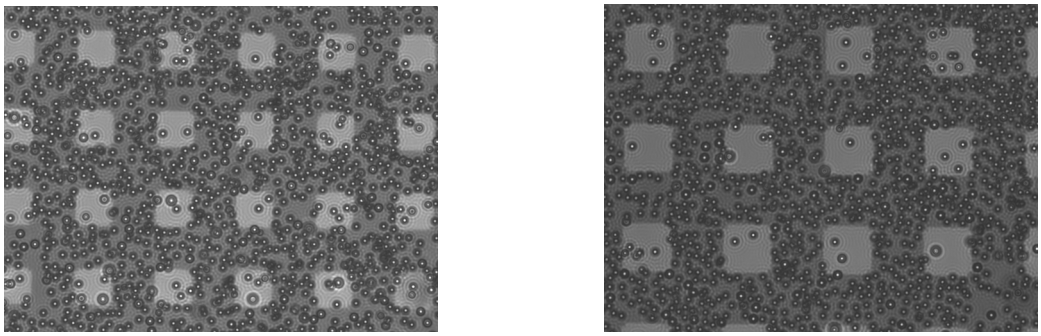

Figure 7.5. Lateral density variations in interfacial colloidal fluid of 4 μm PS particles on chemically patterned substrates. The lighter regions correspond to glass and the darker regions correspond to a 10 nm Au film vapor deposited on the glass substrate through a photomask.

substrates affect the equilibrium density distributions.

On the most basic level, the 2D fingerprint in Figure 7.3 can be broken down into two basic geometries: channels and squares. This motivated crystallization studies on channels and hexagons that are reported in this work. Figure 7.4 shows the two basic geometries studied in this Section in relation the overall simulation box size. For all simulations performed on channels, the width (W) of the channels was fixed at 6.2 times the particle radius and the number of particles (N) was fixed at 50. The size of the simulation box (L) and hence the length of the channel was varied for different area fractions. The variable channel area rules out a simple comparison of the various area fraction cases on the basis of feature depth. This is accounted for by using a transformed energy scale (*Etot*), the details of which are explained in Section 7.3.3.

For the hexagons, the area of the feature was kept constant. For all simulations

performed on hexagonal patterns, the minimal radius was set to be 5.283 times the particle radius which set the length of the side of the hexagon (W) to 6.1 times the particle radius. The size of the simulation box (L) was fixed at twice the maximal diameter of the hexagon (4W), and the number of particles was varied to obtain a range of area fractions. In this case too a transformed energy scale (*Etot*) was employed to facilitate comparison of the patterns.

Parabolic and square pattern cross sections are investigated in this report. As described in Section 3, an HF etch was used to fabricate the physical features used in our experiments. Previous AFM scans on these features confirm the parabolic nature of the physical well cross-section.[88] These parabolic profiles will be used to represent physical patterns during the remainder of this Section. The typical form of the parabolic well used is $\frac{u(x,y)}{kT} = 4\frac{u_{welldepth}}{kT}\frac{(x^2+y^2)}{W^2} - u_{welldepth}$, where $u_{welldepth}$ is the potential energy well minimum. For the channel patterns, the *y* term drops out of the equation.

While all the template directed experiments conducted in this dissertation involved the use of physical wells, equivalent experiments on chemically patterned substrates could be just as easily implemented. Chemical patterns with a uniform "square well" type attraction across their area can be produced by patterning 10nm Au films on SiO_2 surfaces (Figure 7.5) to produce van der Waals energy wells. The typical form of the square well used is $\frac{u(x,y)}{kT} = \frac{u_{welldepth}}{kT}$, where $u_{welldepth}$ is the potential energy well minimum. Figure 7.6 describes the cross sections in greater detail. For patterns of same width and energy minimum, Figure 7.6 shows the parabolic/physical pattern (red)

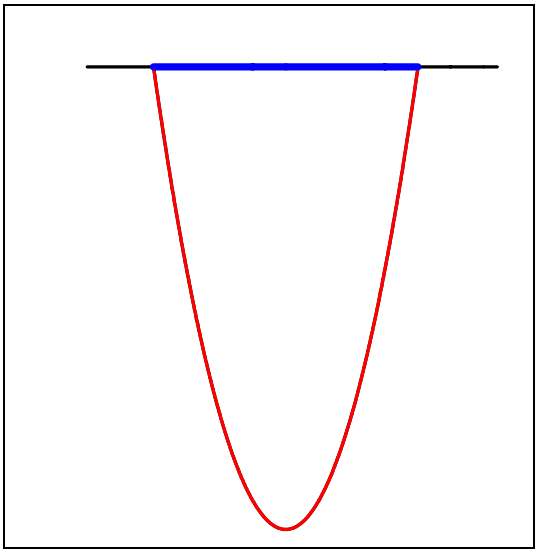

Figure 7.6. Schematic representation of a physical potential energy well (red) and a chemical "patch" of uniform energy across its surface (blue).

and the square/chemical pattern cross sections.

7.3.2 Reference Area Fraction

We are interested in isolating conditions under which patterns get completely filled with single colloidal crystals. It therefore follows that colloid area fraction and pattern area are important factors in determining the above mentioned thermodynamic state. A parameter that effectively captures this effect is the minimum number of particles that can be accommodated inside the pattern in a hexagonally closed packed lattice N_R. The area fraction that is associated with N_R is termed as the reference area fraction ϕ_R, and is calculated as N_R/L^2, where L is the length of the simulation box (Figure 7.4). All area fractions above this reference area fraction will yield, under the correct particle-particle attraction and pattern well depth conditions, single crystals that

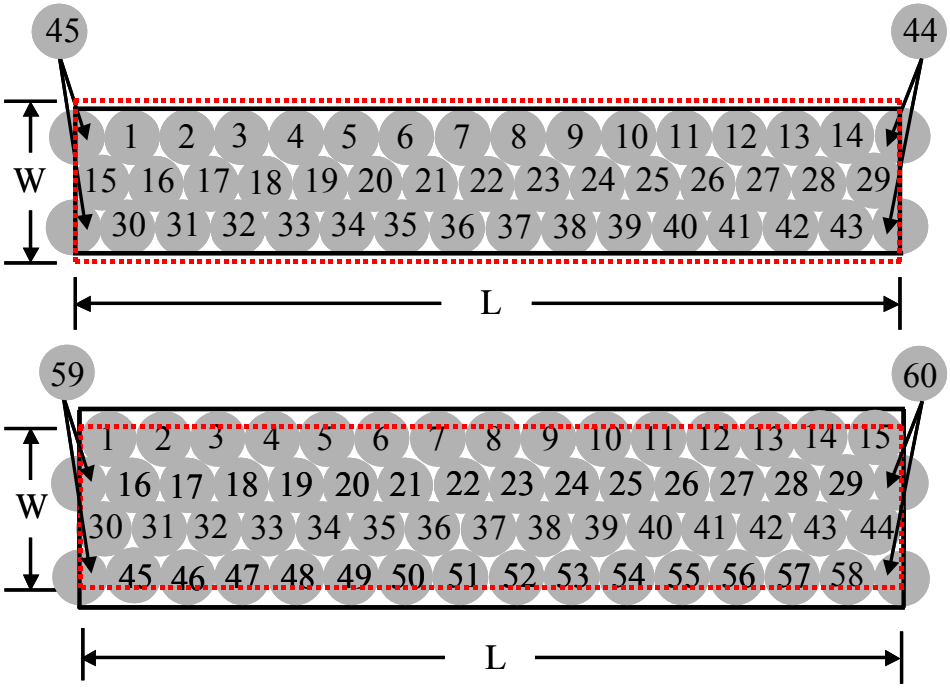

Figure 7.7. Different N_R values for parabolic (top) and square (bottom) channels of same length and width. The red rectangle represents the actual area occupied by the pattern and the black rectangle represents the area occupied by the hexagonally closed packed crystal that fills it up.

fill up the pattern. In the final phase plots, we therefore normalize the area fractions ϕ investigated by the reference area fraction and refer to this as $\phi^*=\phi/\phi_R$.

All four types of patterns investigated in this report have different N_R values. As a representative example, we show the difference in N_R for parabolic and square channels of the same width in Figure 7.7. It is easy to see that for a given feature geometry, parabolic wells accommodate a lesser number of closed packed particles than square wells. The N_R value for the parabolic channel at $\phi=0.16$ ($L/a=31.33$, where a is the particle radius) is N_R = 45, while that for the square channel at $\phi=0.16$ is N_R = 60.

Because the width (W) of the channels remains constant, an analysis of N_R at a ϕ=*0.16* is sufficient for calculating ϕ^* at all other ϕ values as $N_{R-\phi} = \frac{L_\phi}{L_{0.16}} N_{R-0.16}$. The N_R value for the hexagon with a parabolic cross section is N_R = 27, while that for the hexagon with a square cross section is N_R = 37. Since the feature size remains fixed in the case of the hexagonal patterns, all area fraction cases investigated therein have the same N_R.

Table 7.1. Summary of simulations carried out for each area fraction ϕ.

	u_{wall}/kT			
	3	***6***	***9***	***12***
u_{pp}/kT	0	0	0	0
	1.99	1.99	1.99	1.99
	2.832	2.832	2.832	2.832
	3.192	3.192	3.192	3.192
	3.529	3.529	3.529	3.529
	3.856	3.856	3.856	3.856
	4.168	4.168	4.168	4.168

7.3.3 Simulation and Phase Behavior Conditions/Parameters

Two dimensional, *NVT*, MC simulations were run for the parabolic channels at area fractions of ϕ = 0.16, 0.2, 0.28 and 0.32, for the square channels at area fractions of ϕ = 0.2, 0.24, 0.28 and 0.32 and for the hexagons at area fractions of ϕ = 0.2163, 0.3113, and 0.4116. For each of these cases, a range of particle-particle attractions, u_{pp} and feature depth, u_{well} are used as shown in Table 7.1. The u_{pp} and u_{well} values listed in the table signify potential energy minima. The interparticle potential used is the summation

of a hard wall repulsion and a simple AO depletion potential shown in Equations 2.2 & 2.13.

7.3.4 Transformed Pattern Energy (Etot)

From Figures 7.4-7, it is easy to deduce that each pattern presents the particles with a unique potential energy landscape (Section 6). As mentioned earlier, the varying area of the channel patterns (Figure 7.4 and Section 7.3.1) and different numbers of particles used in the hexagon patterns further complicate matters. A simplest way to compare these different potential energy landscapes is to perform a simple integration of the feature potential energy well, thus defining $Etot = \int u_{well}(x, y)dA$. *Etot*, along with ϕ^* are used to compare the various simulations conducted in this report.

7.3.5 Constructing the Phase Diagrams

We construct u_{pp} vs. *Etot* phase diagrams for each area fraction ϕ^*. We will now go over the procedure and criteria we use in the construction of these phase plots. Our purpose here is to determine whether a particular combination of u_{pp} and *Etot* results in crystallization within the patterns. It is important to note that for all ϕ^*, u_{pp} and *Etot* values investigated in this work, the location of the crystal growth was always within the features.

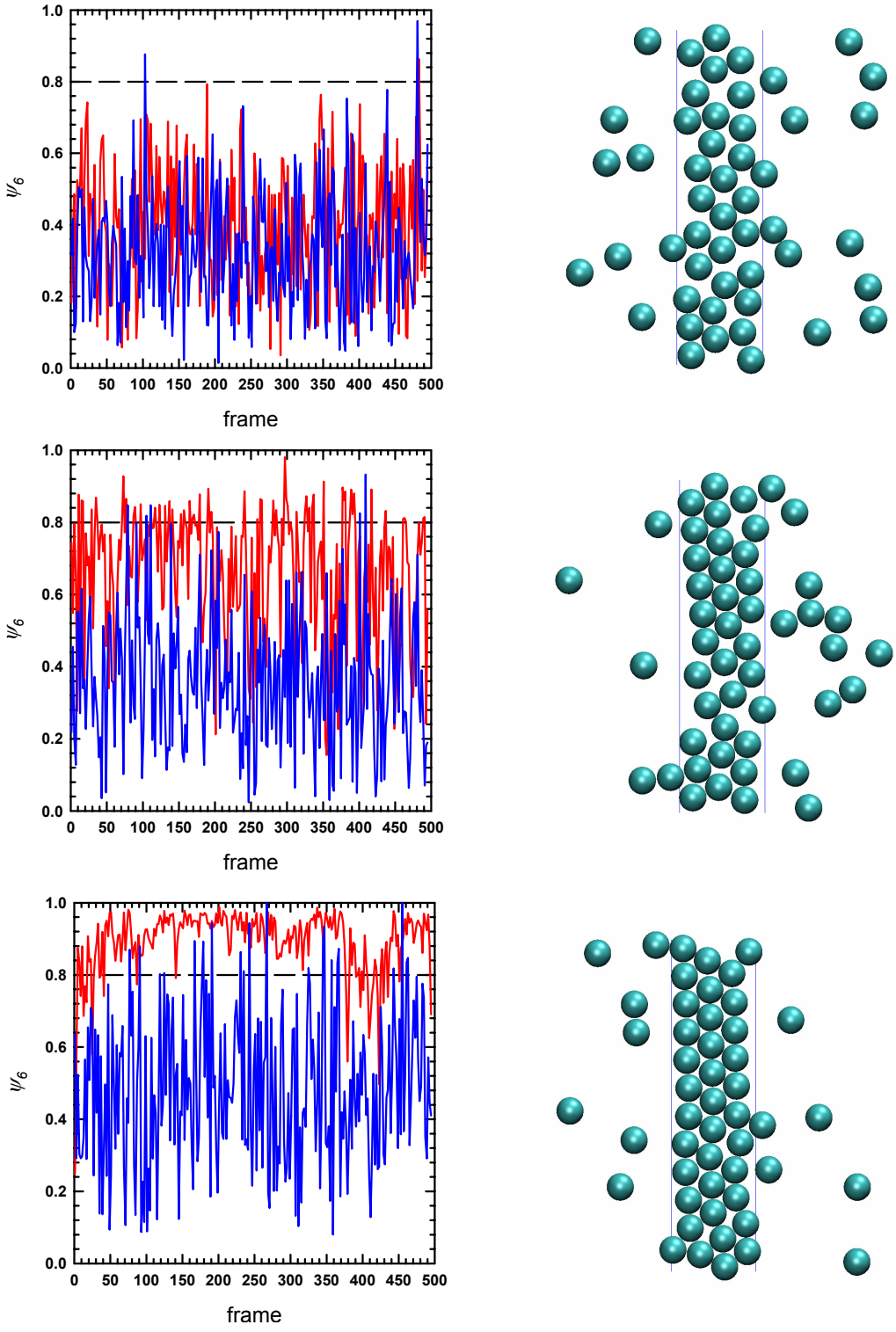

Figure 7.8. Global bond order parameters within (red) and outside (blue) the parabolic channels 12kT deep at ϕ=*0.28* for interparticle attractive potential minima of 1.99kT (top), 2.832kT (center) and 3.529kT (bottom).

To determine the onset of crystallization within the patterns we evaluate the global bond orientation parameter ψ_6 inside the features and set the condition for the prevalence crystals within the patterns at $\psi_6 \geq 0.8$. Instances when this condition is met for a large majority of the simulation frames (Figure 7.8, bottom) correspond to the existence of stable crystal phases. When ψ_6 is always below 0.8 we refer to that as a non-crystalline state (Figure 7.8, top). However there are cases where the system samples ψ_6 values both above and below the 0.8 value, indicating a system on the verge of crystallization (Figure 7.8, center). We determine these points as the phase boundary.

This procedure is performed for all conditions listed in Section 7.3.3 and Table 7.1. For purposes of clarity, we will follow through on the procedure for obtaining the phase diagram for a parabolic channel pattern over the entire range of u_{pp} and u_{well} values at $\phi=0.28$. As described in the earlier paragraph, three "states" are defined based on the how the degree of order within the pattern compares with the criterion $\psi_6 \geq 0.8$. In the phase diagram of u_{pp} vs. u_{well} and all other phase plots in this discussion, the case represented in row 1 of Figure 7.8 is plotted as a (+), that in row 2 of Figure 7.8 is plotted as a (o) and the case in row 3 of Figure 7.8 is plotted as a (•). Figure 7.9a shows the phase diagram that summarizes all the simulation conditions in Table 7.1 for the case of a parabolic channel and a particle area fraction of $\phi=0.28$.

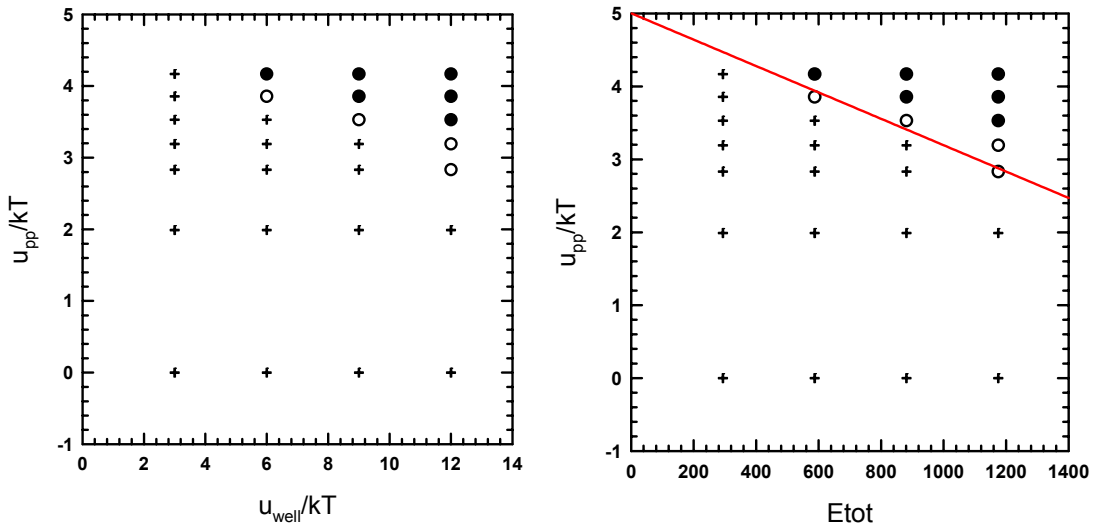

Figure 7.9. (a) A phase plot of u_{pp} vs. u_{well} for a parabolic channel at $\phi=0.28$. (b) The phase plot in (a) obtained by integrating the potential energy landscape of the well. The red line is the best fit to the lowest (o) points.

Figure 7.9a throws light on the effectiveness of patterns in inducing crystallization. The deeper parabolic wells in Figure 7.9 ($u_{well}\geq 6kT$) induce the formation of crystals states that would be absent for even the highest u_{pp} value (4.168kT), had the substrate been homogeneous. We make this claim because Figure 7.9a clearly shows that as the underlying substrate becomes more and more homogeneous ($u_{well}=3kT$), no crystal states were observed. As u_{well} increases, it is observed that lesser amounts of interparticle attraction are required to achieve crystallization within the patterns. As shown in Section 7.3.4, the integrated potential energy landscape of the parabolic channel, *Etot*, while representing the same information, allows different pattern areas to be directly compared, thus allowing a

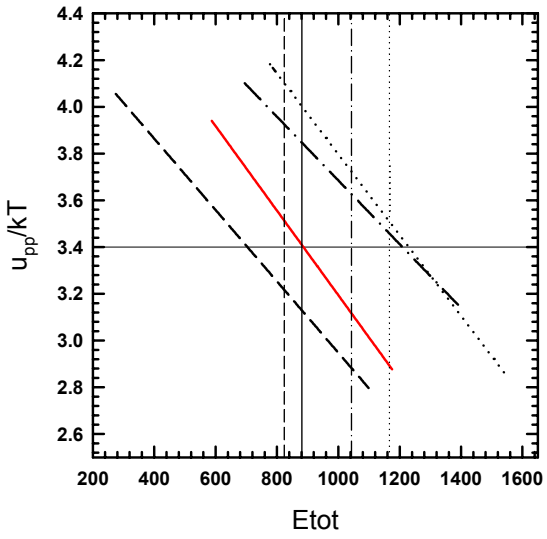

Figure 7.10. Summary phase diagram showing phase boundaries for attractive colloids at area fractions of 0.16(···), 0.2(-·-), 0.28(–) and 0.32(--) in equilibrium with parabolic channels shown schematically in Figure 7.4. The vertical lines correspond to $u_{well}=9kT$ at 0.16(···), 0.2(-·-), 0.28(–) and 0.32(--) respectively. The horizontal line corresponds to $u_{pp}=3.4kT$.

direct comparison between phase plots for different area fractions (Figure 7.9b).

The red line in Figure 7.9b is the best fit to the points that first show the phase behavior represented in Figure 7.7 (center). This line now represents the phase transition line for the system in equilibrium with that particular patterned substrate. The case plotted in Figure 7.9b, the patterned substrate is a parabolic channel with the system $\phi=0.28$. This is how phase plots and phase transition lines are obtained for all other area fractions and for each different kind of pattern.

7.3.6 Phase Transitions for Parabolic Channels

Figure 7.10 compares the phase boundary for a system of attractive colloids on parabolic channels at $\phi=0.28$ (Figure 7.9b, red line) with other area fraction conditions

investigated (ϕ*=0.16, 0.2 & 0.32)* for the selfsame patterns. For a given ϕ, all *Etot* and u_{pp} values that lie above the phase boundary line will yield single patterned crystals. As area fraction is increased, the phase boundary shifts to lower values of *Etot* and u_{pp}. It is important to keep in mind that equal values of *Etot* do not represent physical wells of equal depth.

To better explain the phase behavior, we have also plotted lines that correspond to u_{well}*=9kT* for ϕ*=0.16* (vertical dotted line)*, 0.2* (vertical dash-dot line)*, 0.28* (vertical solid line) *& 0.32* (vertical dashed line). It now becomes easy to see that for a parabolic physical pattern with u_{well}*=9kT*, an interparticle attraction of u_{pp}*=3.4kT* (horizontal line) suffices for filling the patterns with crystal phases at $\phi \geq 0.28$. At lower area fractions (ϕ*<0.28*), for the same u_{well}, higher amounts attraction (u_{pp}*>3.4kT*) are required to induce crystallization. Figure 7.10 therefore shows that for fixed u_{pp} and u_{well}, as the area fraction of the colloidal fluid is increased, the system undergoes a pattern-localized, fluid-solid phase transition at an area fraction value that approaches the value obtained on homogeneous substrates as $u_{well} \rightarrow 0$. It is also important to note that ϕ*=0.16, 0.2, 0.28 & 0.32* correspond to ϕ^**=1.111, 1.242, 1.47 & 1.57* respectively for a parabolic pattern, indicating that for all cases investigated here, the crystal phase completely fills up the pattern.

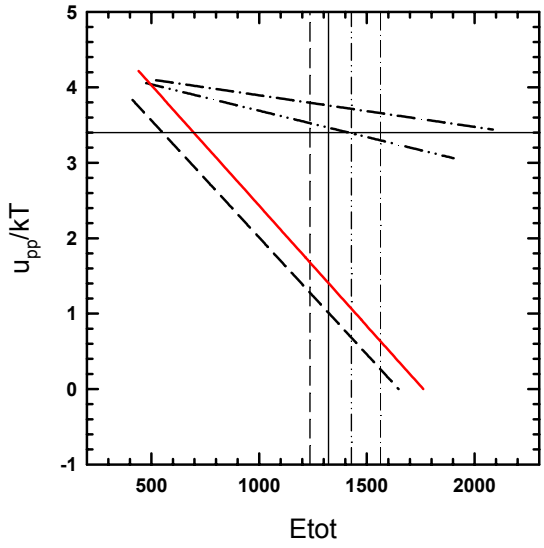

Figure 7.11. Summary phase diagram showing phase boundaries for attractive colloids at area fractions of 0.2(-·-), 0.24(-···-), 0.28(–) and 0.32(--) in equilibrium with square channels shown schematically in Figure 7.4. The vertical lines correspond to $u_{well}=9kT$ at 0.2(-·-), 0.24(-···-), 0.28(–) and 0.32(--) respectively. The horizontal line corresponds to $u_{pp}=3.4kT$.

7.3.7 Phase Transitions for Square Channels

Figure 7.11 compares the phase boundary for a system of attractive colloids on square channels at $\phi=0.28$ (red line) with other area fraction conditions investigated ($\phi=0.2,\ 0.24$ & 0.32) for the selfsame patterns. A shifting of the phase boundary to lower values of *Etot* and u_{pp} reported previously for parabolic channels is observed for square channels too. Once again, it is important to keep in mind that equal values of *Etot* do not represent chemical patterns of equal well depth.

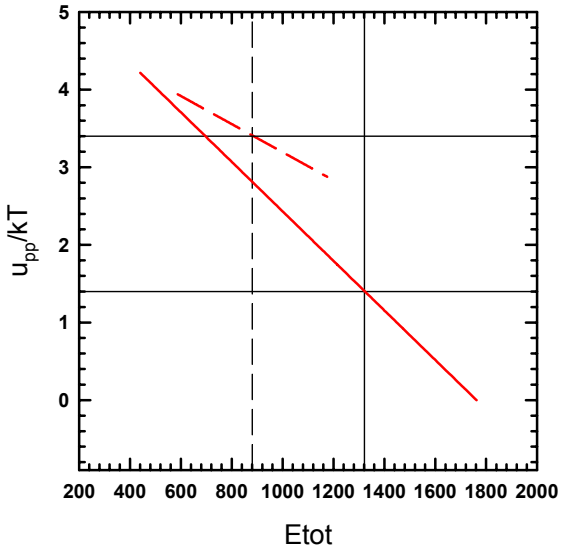

Figure 7.12. Phase boundaries for attractive colloids at $\phi=0.28$ for square (–) and parabolic (––) channels. The vertical lines correspond to $u_{well}=9kT$ and $\phi=0.28$ for square (–) and parabolic (––) channels respectively.

As with the previous case, we have plotted lines that correspond to $u_{well}=9kT$ for $\phi=0.2$ (vertical dash-dot line), 0.24 (vertical dash-dot-dot-dash line), 0.28 (vertical solid line) & 0.32 (vertical dashed line). For a square physical pattern with $u_{well}=9kT$, an interparticle attraction of $u_{pp}=3.4kT$ (horizontal line) suffices for filling the patterns with crystal phases at $\phi\geq0.24$ as opposed to $\phi\geq0.28$ for parabolic channels, an observation that will be discussed in detail in the next section. Note that $\phi=0.2, 0.24, 0.28$ & 0.32 correspond to $\phi^*=0.932, 1.02, 1.1$ & 1.18 respectively for a parabolic pattern. This is important because only three of the four cases yield crystal phases that completely fill up the pattern.

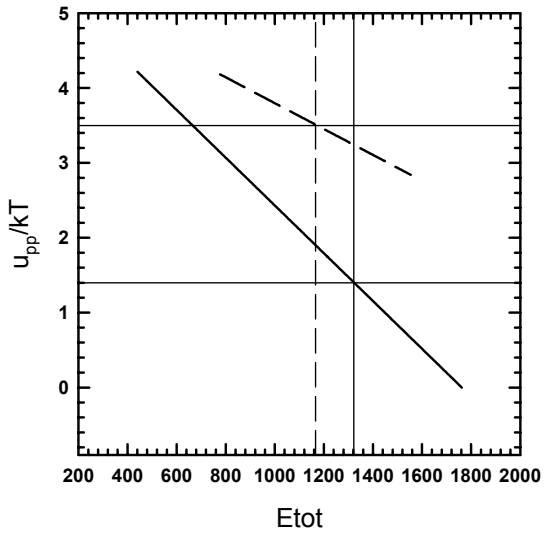

Figure 7.13. Phase boundaries for attractive colloids at $\phi^*=1.1$ for square (–) and parabolic (––) channels. The vertical lines correspond to $u_{well}=9kT$ and $\phi=0.28$ for square (–) and $u_{well}=9kT$ and $\phi=0.16$ for parabolic (––) channels respectively.

7.3.8 Comparing Parabolic and Square Channels

For the same L, W, N and ϕ, Figure 7.12 directly compares the phase boundaries for a system of attractive colloids in equilibrium with square (Figure 7.12, solid line) and parabolic (Figure 7.12, dashed line) channels. For patterns with $u_{well}=9kT$ at $\phi=0.28$, the parabolic patterns require $u_{pp}\geq 3.4kT$ (vertical dashed line) to have channels completely filled with crystals. At $u_{well}=9kT$ and $\phi=0.28$, the square patterns on the other hand require only $u_{pp}\geq 1.4kT$ (vertical solid line) to be entirely filled with crystals. At $\phi=0.28$, $\phi^*=1.1$ & 1.47 for the square and parabolic channels respectively. This clearly indicates that for same L, W, N and ϕ, for $\phi^*\geq 1.0$, the square channels are much more effective at forming localized, channel filling crystals than the parabolic channels.

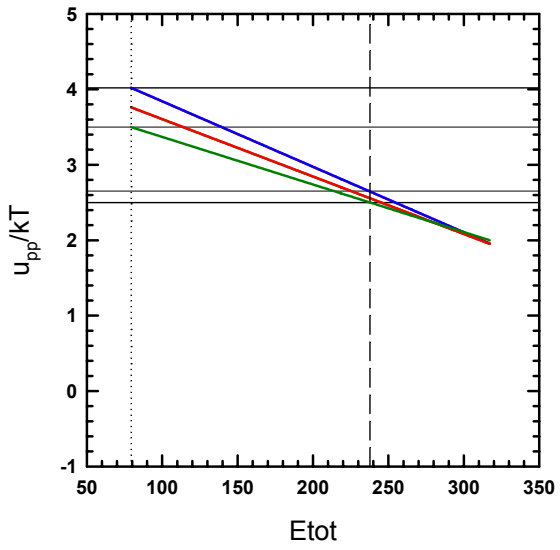

Figure 7.14. Summary phase diagram showing phase boundaries for hexagon patterns with parabolic cross sections at colloid area fractions of 0.22(–), 0.31(–) and 0.41(–). The vertical lines correspond to $u_{well}=9kT$ (···) and $u_{well}=3kT$ (--). The horizontal lines correspond to $u_{pp}=4kT$, $3.5kT$, $2.65kT$ and $2.5kT$.

We also compared square and parabolic channels at the same conditions of "supersaturation", $\phi^{*}=1.1$. Figure 7.13 compares the phase boundary for a square channel at $\phi=0.28$ with that of a parabolic channel at $\phi=0.16$. Under conditions of equivalent supersaturation too, square channels are far more effective at inducing crystallization than their parabolic counterparts. The important detail not to be glossed over here is that when it comes to single pattern-filling crystallization, square/chemical patterns are better than physical/parabolic patterns but, as explained in Section 7.3.2, due to the nature of the etch process, physical patterns and the parabolic cross sectional channels that represent them fill in completely at lower ϕ values than square patterns. This means that while it is possible to get single pattern-filling crystals for ϕ values as

low as *0.144* for the conditions listed in Table 7.1 on parabolic channels, square channels do not yield this equilibrium state until ϕ values as high as *0.255*.

7.3.9 Phase Transitions for Parabolic Hexagons

Figure 7.14 compares the phase boundary for a system of attractive colloids on hexagon with a parabolic cross section at ϕ*=0.22*, *0.31 & 0.41*. For a given ϕ, all *Etot* and u_{pp} values that lie above the phase boundary line will yield single patterned crystals. The phase boundary shifts to lower values of *Etot* and u_{pp} as area fraction is increased. Increasing u_{well} causes the crystallization to become area fraction independent. As shown in Section 7.3.1 & Figure 7.4, the size of the parabolic feature is kept constant and therefore equal *Etot* values represent physical wells of equal depth. We have also plotted lines that correspond to u_{well}*=3kT* (vertical dotted line) *& 9kT* (vertical dashed line). While a difference of Δu_{pp}*~0.5kT* exits between the ϕ*=0.22 & 0.41* cases at u_{well}*=3kT*, this difference becomes negligible when $u_{well} \rightarrow$*9kT*. It is also important to note that ϕ*=0.22, 0.31 & 0.41* correspond to ϕ^**=1.52, 2.18 & 2.89* respectively for a parabolic pattern, indicating that for all cases investigated here, the crystal phase completely fills up the pattern.

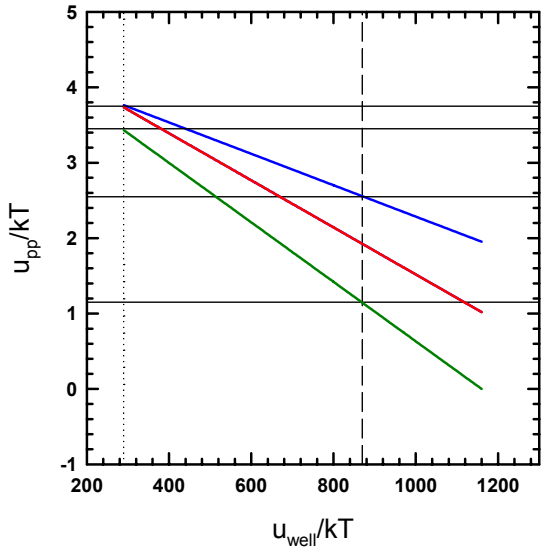

Figure 7.15. Summary phase diagram showing phase boundaries for hexagon patterns with square cross sections at colloid area fractions of 0.22(–), 0.31(–) and 0.41(–). The vertical lines correspond to $u_{well}=9kT$ (···) and $u_{well}=3kT$ (--). The horizontal lines correspond to $u_{pp}=3.75kT$, $3.45kT$, $2.55kT$ and $1.15kT$.

7.3.10 Phase Transitions for Square Hexagons

Figure 7.15 compares the phase boundary for a system of attractive colloids on hexagon with a square cross section at $\phi=0.22$, 0.31 & 0.41. The phase boundary shifts to lower values of *Etot* and u_{pp} as area fraction is increased. As opposed to the area fraction independent behavior induced by increasing u_{well} on parabolic patterns, square patterns show area fraction independent behavior as $u_{well}\rightarrow 0kT$. Here too, the size of the parabolic feature is kept constant and therefore equal *Etot* values represent physical wells of equal depth. We have also plotted lines that correspond to $u_{well}=3kT$ (vertical dotted line) & $9kT$ (vertical dashed line) which serve to reiterate the loss of area fraction dependence as $u_{well}\rightarrow 0kT$. It is also important to note that $\phi=0.22$, 0.31 & 0.41

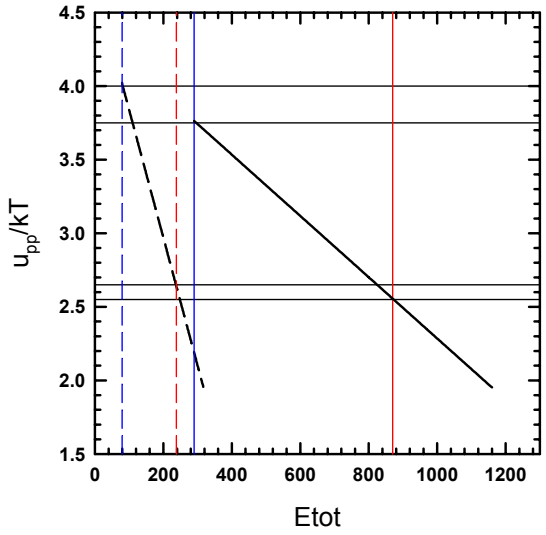

Figure 7.16. Phase boundaries for attractive colloids at $\phi=0.22$ for square (–) and parabolic (––) channels. The vertical lines correspond to $u_{well}=3kT$ and $9kT$ for square (–), (–) and parabolic (––), (––) channels respectively.

correspond to $\phi^{*}=1.11,\ 1.59\ \&\ 2.11$ respectively for a square pattern, indicating that for all cases investigated here, the crystal phase completely fills up the pattern.

7.3.11 Comparing Parabolic and Square Hexagons

For the same L, W, N and ϕ, Figure 7.16 directly compares the phase boundaries for a system of attractive colloids in equilibrium with square (Figure 7.16, solid line) and parabolic (Figure 7.16, dashed line) cross sectioned hexagons. For both $u_{well}=3kT$(blue vertical lines) & $u_{well}=9kT$(red vertical lines), the square patterns fill up with crystals at lower u_{pp} values than parabolic patterns. While this observation is consistent with the results from simulations on the channel patterns, the difference in the u_{pp} values for crystallization on square as opposed to parabolic cross sectioned hexagons for equal u_{well} is negligible ($\Delta u_{pp}\sim 0.1kT$) when compared to their difference on the channels ($\Delta u_{pp}\sim 2kT$) (Figure 7.12). Comparing conditions of equivalent "supersaturation" ($\phi^{*}=1.59$ *or* $\phi=0.22$ on parabolic and $\phi=0.31$ on square) also suggests that pattern cross section is not as significant in determining the crystallization phase boundary on hexagon/isotropic

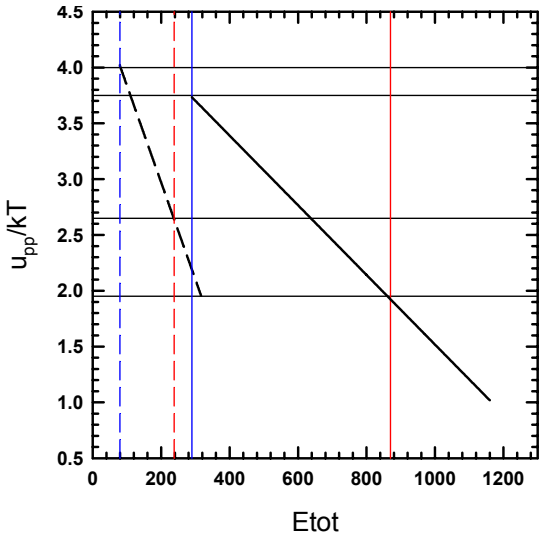

Figure 7.17. Phase boundaries for attractive colloids at $\phi^{*}=1.59$ for square (–) and parabolic (––) channels. The vertical lines correspond to $u_{well}=3kT$ and $9kT$ for square (–), (–) and parabolic (––), (––) channels respectively.

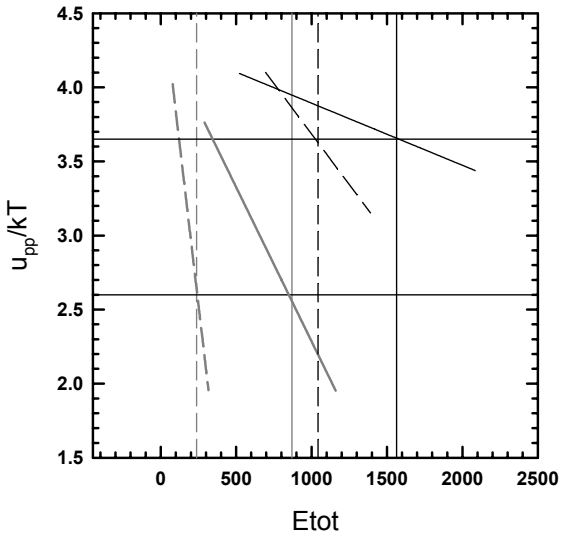

Figure 7.18. Comparing the hexagon/isotropic features (–), (––) with the channel/non-isotropic features (–), (––) for equal ϕ*=0.2*. The vertical lines correspond to u_{well}*=9kT*.

features as it is in channel or non-isotropic features (Figure 7.17).

7.3.12 Comparing Isotropic and Non-Isotropic Patterns

For equal ϕ, Figure 7.18 clearly shows that for the same u_{well}*=9kT* (vertical lines), hexagon/isotropic features require far lesser values of u_{pp} (*~2.6kT*) than channel/non-isotropic features (*~3.65kT*) to be entirely filled with crystals. However due to the differences in the definition of pattern size relative to simulation boxsize between the two cases, a comparison of the two types of features on an equivalent "supersaturation" basis is required. In Figure 7.19, we compared the hexagons with the channels at ϕ^**=1.59*, which amounts to a ϕ*=0.32* parabolic channel, a ϕ*=0.22* parabolic cross sectioned hexagon and a ϕ*=0.31* square cross sectioned hexagon respectively. For a u_{well}*=9kT* (vertical lines), its easy to see that isotropic patterns with square/chemical

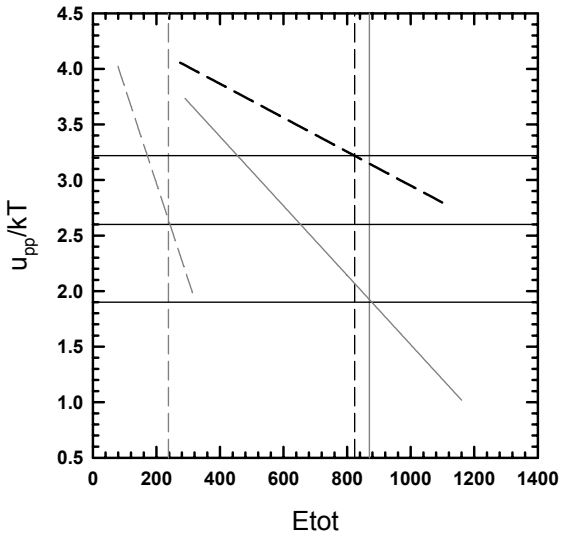

Figure 7.19. Comparing the hexagon/isotropic features (–), (––) with the channel/non-isotropic features (–), (––) for equal $\phi^*=1.59$. The vertical lines correspond to $u_{well}=9kT$.

nature require the least u_{pp} (solid gray line) followed by parabolic/physically patterned isotropic patterns (dashed gray line) and finally the non-isotropic pattern. Thus we can say, with some confidence that if we ensure conditions of crystallization on non-isotropic patterns, under those self-same conditions, crystallization on isotropic patterns is assured.

7.3.13 Summary and Application to Micropolis Circuit

From the results in Sections 7.3.6-12, we observe that a) when comparing patterns of equal size, features with parabolic cross sections always fill in at lower values of ϕ than their square equivalents. Therefore, for a given ϕ^*, $(\phi)_{parabolic}<(\phi)_{square}$ because $(\phi_R)_{parabolic}<(\phi_R)_{square}$. b) For channel/non-isotropic features, under conditions of equal u_{well}, patterns with square cross sections require significantly lesser u_{pp} than the

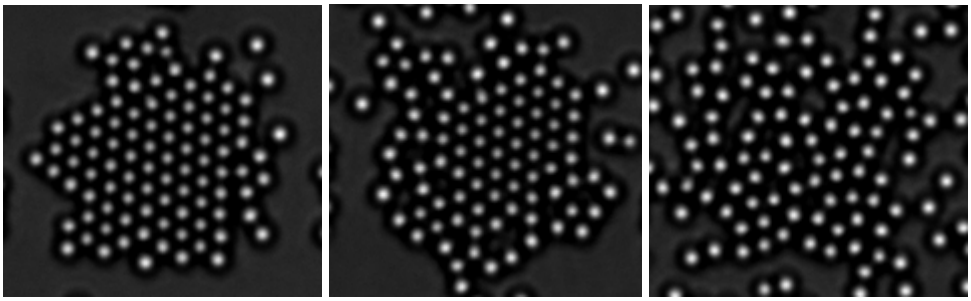

(a) (b) (c)

Figure 7.20. Equilibrium configurations of 2.34μm SiO_2 colloids levitated over $u_{well}=4kT$ deep physical features etched on a glass substrate. The interparticle depletion potential minimum, u_{pp} changes from $u_{pp}=6kT$ at 20°C (a) to $u_{pp}=4.5kT$ at 26°C (b) to $u_{pp}=3.2kT$ at 28°C (c). The value of $\phi^*=1.22$.

equivalent parabolic channels to induce pattern filling crystals. This effect observed when comparing patterns of equal size as well as systems of equal "supersaturation". c) For hexagonal/isotropic features, under conditions of equal u_{well}, patterns with square cross sections are just as effective at inducing crystals (u_{pp} is the same) as equivalent parabolic channels. d) Conditions of ϕ, u_{pp} and u_{well} that result in single pattern filling crystals on channel/non-isotropic features will also form this thermodynamic equilibrium state on hexagonal/isotropic features.

We wish to discuss the observations made in the preceding paragraph in reference to the experimental results presented in Section 6. Figure 7.20 serves as experimental evidence in verifying the simulation results presented in this Section. The experiment was conducted for a $\phi^*=1.22$ which, under appropriate conditions of u_{well} and u_{pp}, should yield single pattern filling crystals. Figure 7.20a shows that for T=20°C, $u_{pp}=6kT$ and that, in combination with the underlying parabolic feature depth of

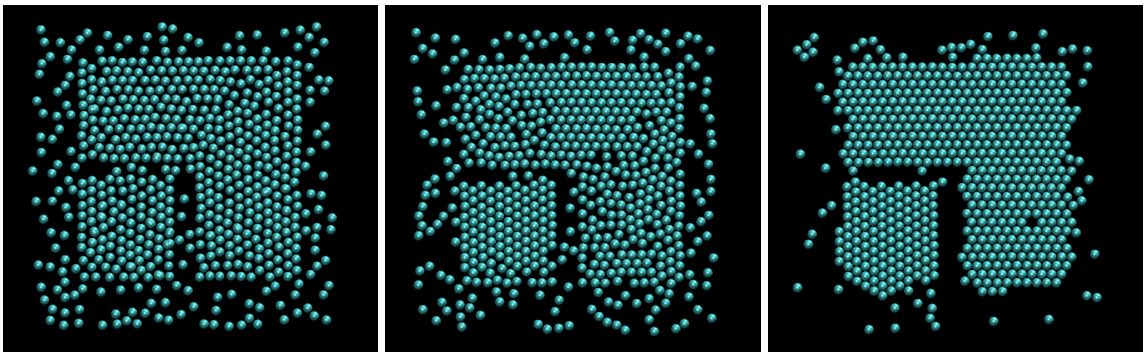

(a) (b) (c)

Figure 7.21. Equilibrium configurations of 2.34μm SiO_2 colloids levitated over $u_{well}=12kT$ deep square features. The interparticle depletion potential minimum, u_{pp} changes from $u_{pp}=0kT$ in (a) to $u_{pp}=2kT$ in (b) to $u_{pp}=4kT$ in (c). (a), (b) & (c) correspond to (+), (o) & (•) in Figure 7.22. The value of $\phi^*=1.11$.

$u_{well}=4kT$, yields a phase similar to that described in Figure 8.8 (bottom) and represented by a (•) in phase plots of the form shown in Figures 7.9(a) & (b).

As described in the previous Section, we have an experimental system where it is possible to tune the interparticle attraction. We use this ability to reduce the attraction minimum to $u_{pp}=4.5kT$ at 26°C (Figure 7.20b) for the same ϕ^* & u_{well}, which results in an equilibrium state similar to that described in Figure 7.8 (middle) and represented by a (o) in phase plots of the form shown in Figures 7.9(a) & (b). Finally, at T=20°C, $u_{pp}=3.2kT$ which results in phases similar to those described in Figure 7.8 (top) and represented by a (+) in phase plots of the form shown in Figures 7.9(a) & (b). We now want to use the information we have gathered to suggest an experiment (Figure 7.21) that should enable the engineering of the 2D equivalent of the "micropolis" circuit shown in Figure 7.3.

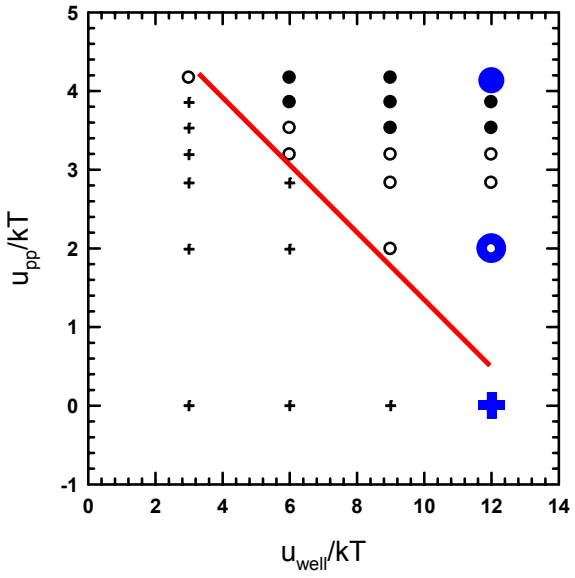

Figure 7.22. A phase plot of u_{pp} vs. u_{well} for a square channel at $\phi=0.28$. (+), (o) & (•) correspond to (a), (b) and (c) in Figure 7.21 respectively. The value of $\phi^*=1.11$.

We first demonstrate the use of the phase diagrams to engineer single pattern localized colloidal crystals on a small part of the micropolis circuit. The patterned area has a uniform attraction of $u_{well}=12kT$ all over its surface. It therefore behaves like a chemical pattern/square well. We then used $\phi^*=1.11$ to ensure that the crystals that formed filled in the patterns. Finally, we navigated the phase diagram shown in Figure 7.21 to achieve the thermodynamic states observed in Figure 7.21. By starting out with $u_{pp}=0kT$ (Figure 7.22, (+)), we get the equilibrium state shown in Figure 7.21a in which the deep pattern concentrates the hard spheres. At $u_{pp}=2kT$ (Figure 7.22, (o)), we get the equilibrium state shown in Figure 7.20b. Finally, at $u_{pp}=4kT$ (Figure 7.22, (•)), we get the desired equilibrium crystalline state shown in Figure 7.20c. We then extended this to

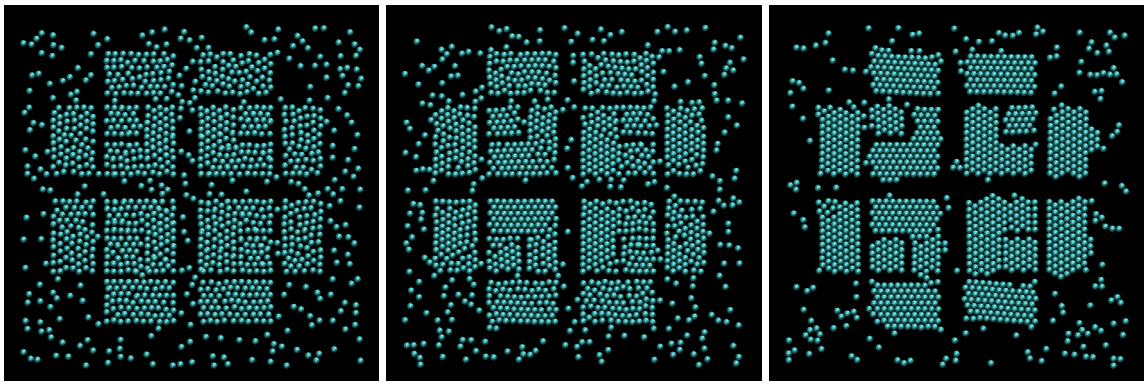

(a) (b) (c)

Figure 7.23. Equilibrium configurations of 2.34μm SiO_2 colloids levitated over $u_{well}=12kT$ deep square features. The interparticle depletion potential minimum, u_{pp} changes from $u_{pp}=0kT$ in (a) to $u_{pp}=2kT$ in (b) to $u_{pp}=4kT$ in (c). (a), (b) & (c) correspond to (+), (o) & (•) in Figure 7.22. The value of $\phi^{*}=1.11$.

the full micropolis circuit for the same $\phi=0.28$ and u_{pp} and u_{well} conditions explored in Figure 7.22 ((+), (o) & (•)). The results are shown in Figure 7.23.

7.4. Conclusions

We studied pattern mediated 2D interfacial crystallization for physically/parabolic and chemically/square pattern substrates. For each of these cases, we studied crystallization on isotropic/hexagons and non-isotropic/channel patterns. For patterns of equal size, we found that features with parabolic cross sections always filled in with crystals at lower ϕ values than their square equivalents. The channel/non-isotropic features with square cross sections, under conditions of equal u_{well}, required significantly lesser interparticle attraction to induce crystallization than the equivalent parabolic channels. This effect observed when comparing patterns of equal size as well

as systems of equal “supersaturation”.

Hexagonal/isotropic features however, under conditions of equal $u_{well,}$ showed that square cross sections are just as effective at inducing crystals (u_{pp} is the same) as equivalent parabolic ones. Also, conditions of ϕ, u_{pp} and u_{well} that result in single pattern filling crystals on channel/non-isotropic features also formed the said thermodynamic equilibrium state on hexagonal/isotropic features. We verified our simulation findings against experimental results presented in this dissertation and also used phase diagrams to suggest the engineering of a “micropolis” circuit[9] templated colloidal crystal.

8. CONCLUSIONS

8.1. Summary of Conclusions

Spatially controlled interfacial self assembly of micron sized particles into robust ordered structures via intelligent predictions and sensitive manipulation of attractive colloidal interactions on the order of thermal energy, kT, with applications to photonic devices, has been the motivation behind the work reported in this dissertation. At the most basic level, we explore the forces, hydrodynamics and phase behavior of submonolayer sediments of SiO_2 particles over glass substrates in an aqueous medium. A synergistic experiment and simulation approach is adopted to intelligently exploit the solvent-quality sensitivity of two water soluble polymers to induce reversible, exquisitely controlled, short-ranged attractive interactions between the SiO_2 colloids and between the sediment and the underlying substrate, with the view of manipulating the structure and dynamics of these interfacial systems. The main goal of this research is to provide solutions to a long standing problem of achieving reversible, attraction-induced crystallization in colloidal systems, an area with tremendous materials and device applications.

With that in mind, the following tasks essential to accomplishing that goal were addressed in this dissertation: 1) use a combination of sensitive measurements and established theory to comprehensively understand and experimentally prove the tunability of van der Waals attraction between SiO_2 colloids through solvent quality control over the thickness of stabilizing polymer brush layers adsorbed to their surfaces,

2) make synergistic use of sensitive experimental measurements, established theory and simulation predictions to intelligently design a system wherein cross-linked, non-adsorbing, thermoresponsive, polymer nano-particles provide exquisite, reversible control over the attractive short ranged-depletion forces in the interfacial SiO_2 particle/glass wall system and result in reversible interfacial crystallization, 3) effectively use shallow physically patterned glass substrates to control the location of tunable, depletion attraction-induced crystallization and 4) use the knowledge gained from studies conducted in this dissertation in conjunction with simulations to isolate conditions under which template directed, spatially controlled crystallization occurs for all kinds of patterns, be they physical or chemical, isotropic or non-isotropic, thus allowing for more informed design of future crystallization experiments. The significant conclusions from this work are summarized below:

- The first approach for inducing a tunable attraction in these aqueous interfacial SiO_2 colloid systems involved the use of adsorbing polymer. The basic idea was to control the short ranged colloid-colloid and colloid-substrate van der Waals attraction by controlling the thickness of adsorbed polymer layers on the surfaces of the colloids and the interface and thus achieve interfacial self-assembly of the said particles. We implemented control over the adsorbed polymer layer thicknesses by using temperature and specific ion effects. ETRIM measurements combined with Lifshitz theory yielded direct and sensitive (~1nm or ~0.2kT) proof of the fact that it was indeed possible to control, with an exceedingly high level of accuracy and reproducibility, the strength of the attraction in these interfacial colloidal systems. We also observed an

equivalence of increasing temperature and increasing $MgSO_4$ concentration in decreasing solvent quality and the collapse of the adsorbed polymer layers. By applying established theory to the direct experimental measurements, we are able to link any given solvent condition with an accurate estimate of polymer layer thickness and thereby control the colloid-colloid and colloid-substrate van der Waals attraction to within ~0.2kT. Control over the polymer layer thickness and hence the attractive interactions in this interfacial system was completely reversible. Understanding how to manipulate such interactions between polymer coated colloids provides the ability to reversibly control the stability, phase behavior, and self-assembly of such particles.

- Even though the polymerically stabilized colloid-substrate system we designed allowed the interparticle and particle-substrate attraction to be precisely controlled via temperature and specific ion effects, we were unable to achieve interfacial crystallization even for the highest values of van der Waals attraction. This was probably the most important step towards achieving the research objectives of this dissertation. The reason we were not seeing any crystallization had everything to do with the nature of the attraction potential. Colloid phase behavior depends on a "total attraction area" of sorts, a quantity captured by the second virial coefficient. For equal values of attraction potential minimum and range, depletion interaction potentials have a higher "total attraction area" than a van der Waals potential and therefore induce crystallization. This meant that if we could design an interfacial colloidal system that allowed us to reversibly tune colloid-colloid and colloid substrate depletion attraction; we could achieve the crystallization that was lacking in systems that afforded similar

control over van der Waals attraction. In order to achieve this we needed to use a depletant that either swelled or shrunk with certain changes in solvent conditions and did so reversibly.

- Using cross-linked microgel nanospheres of the thermoresponsive polymer PNIPAM gave us a depletant that shrunk with increasing temperature. At a fixed concentration, larger depletant sizes result in higher amounts of attraction than smaller ones. We used this temperature sensitively of PNIPAM microgel depletants to reversibly control the attraction in interfacial colloidal systems in order to achieve fluid-crystal transitions with decreasing temperature. ETRIM experiments yielded direct and sensitive measurements of the tunable depletion attraction as a function of temperature. By using the simplest theoretical description of the system (AO model) in conjunction with direct DLS measurements of the temperature-dependent PNIPAM depletant size, we were able to quantify the ETIRM measurements. These directly measured interparticle and particle-substrate interaction were used in MC simulations that yielded phase behavior that showed excellent quantitative agreement with the experimental observations. The same video microscopy experiments that recorded the structure of the equilibrium phases were also used to quantify the dynamics of the interfacial colloidal system. By using the directly measured and quantified attractive potentials in Stokesian Dynamic simulations, we were able to obtain diffusivities that showed excellent agreement with experimental values. We have therefore developed a colloidal system wherein we can precisely control interparticle and particle-substrate attraction to yield desired interfacial colloidal phases. Control over the forces and their relation to the

structure and the dynamics of the resulting phases has been achieved but there was still a lack of control over the spatial location of the crystals.

- In Section 6, we demonstrated the use of shallow (~310nm) physically etched features on a glass substrate to control the crystallization location of colloids diffusing above them. The SiO_2 colloid/PNIPAM microgel depletant system developed and quantified in Section 5 was used in this study. Using this already quantified and accurately known temperature-tunable depletion attraction, we were able to obtain reversible 2D crystallization on these patterned substrates with the location of crystal growth always confined to the features. We also characterized and explained the structure and the dynamics of the equilibrium phases that assembled over these underlying substrates at each temperature. It was observed that for a fixed underlying feature depth, increasing interparticle attraction concentrated more and more colloids within the feature at the expense of the fluid outside until crystallization occurred. For systems of colloids diffusing over patterned substrates, we found that both D^S_S and D^S_L decreased as the interparticle attraction increased. For the shallow patterns used in this dissertation, the change in crystallization temperature as compared to its value on a homogeneous substrate (26°C) was less than 2°C, the minimum temperature increment used in the experiments and was therefore missed. We postulate that if we had used deeper physical features, we could have observed this shift above the limited temperature resolution of our studies (i.e. crystals at 28°C). We have successfully engineered spatially controlled, attraction driven, reversible colloidal crystals on physical features. If we wished to perform informed crystallization experiments on

patterns of any nature (chemical or biomolecular) or shape (isotropic or non-isotropic), we would need to conduct a systematic simulation studies to guide future experiments.

- We studied pattern-mediated 2D interfacial crystallization for physically (parabolic) and chemically (square) patterned substrates. For each of these cases, we studied crystallization on isotropic/hexagons and non-isotropic/channel patterns. The measured and quantified temperature dependent forces that govern the phase behavior and dynamics of the interfacial SiO_2 colloid/PNIPAM microgel depletant system we designed are used in the simulations in Section 7. For patterns of equal size, we found that physical features always filled in with crystals at lower colloid area fractions than their chemical equivalents. The channel/non-isotropic chemical patterns, under conditions of equal pattern depth (van der Waals), required significantly lesser interparticle attraction to induce crystallization than the equivalent physically etched channels. This effect was observed when comparing patterns of equal size as well as systems of equal "supersaturation". Hexagonal/isotropic features however, under conditions of equal pattern depth, showed that chemical patterns are just as effective at inducing crystals as equivalent physically etched ones. Also, conditions of area fraction, interparticle attraction and pattern depth that result in single pattern filling crystals on channel/non-isotropic features also formed the said thermodynamic equilibrium state on hexagonal/isotropic features. We verified our simulation findings against experimental results presented in this dissertation and found them to be accurate in their predictive capabilities. We also used the generated phase diagrams to suggest the engineering of a "micropolis" circuit-templated colloidal crystal. We have therefore 1) developed a

system that gives us reversible 2D interfacial colloidal crystallization 2) achieve spatial control over the crystal location in these systems and 3) performed simulations that will guide future experiments that may look at applying this system to achieve crystallization on patterns of different geometries and nature.

9. FUTURE RESEARCH

9.1. Synopsis

This section briefly summarizes current and future work not presented as part of this dissertation. The ideas discussed below are closely related to Sections 4-7 and are in tune with the central research theme of informed use of tunable colloid-colloid and colloid-substrate attraction with the aim of achieving a desired equilibrium interfacial colloidal configuration, be it ordered or disordered.

9.2. Crystallization via Combined Use of Adsorbed and Non-Adsorbed Polymer

The results presented in this dissertation used polymer to control the interactions between colloids in one of two ways. Results presented in Section 4 of this dissertation used adsorbed polymer to control van der Waals attraction in interfacial colloidal systems. In Sections 5 & 6, we used a non-adsorbing polymer to control depletion forces and influence interfacial phase behavior. A system containing both adsorbed and non-adsorbed polymer is an easy extension and allows for very interesting polymer manipulation of both van der Waals (vdW) and depletion attraction in order to control phase behavior.

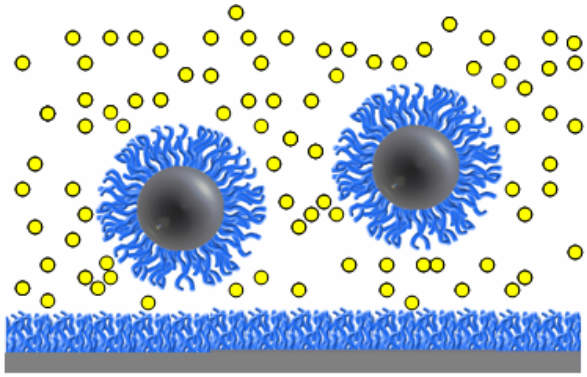

Figure 9.1. A system of 2.34μm SiO_2 colloids levitated above a homogeneous glass substrate. The colloids and the wall are stabilized with an adsorbed PEO brush layer. The bulk contains depletant particles (yellow).

The first investigation we propose involves the use of the system represented in Figure 9.1. As in Section 4, we will adsorb PEO-PPO-PEO block copolymers to hydrophobically modified silica colloids and glass surfaces. The PEO chains shown in blue in Figure 9.1 form a stabilizing brush layer on the surfaces of the particles and the wall. We will also maintain a 24% volume fraction of ~227nm (T=20°C) PNIPAM microgel particles used in Section 6. The system in Figure 9.1 allows us to tune both colloid-colloid and colloid-surface van der Waals and depletion attraction simultaneously. We have already shown (Sections 4&6) that we can reversibly control these forces to within ~0.2kT.

While we have used both temperature and specific ion effects to control the thickness of the adsorbed polymer layers (Section 4), experiments with tunable depletion potentials have only exploited temperature effects on PNIPAM. However, as proven for PEO in Section 4, we anticipate the temperature and specific ion effects on PNIPAM to

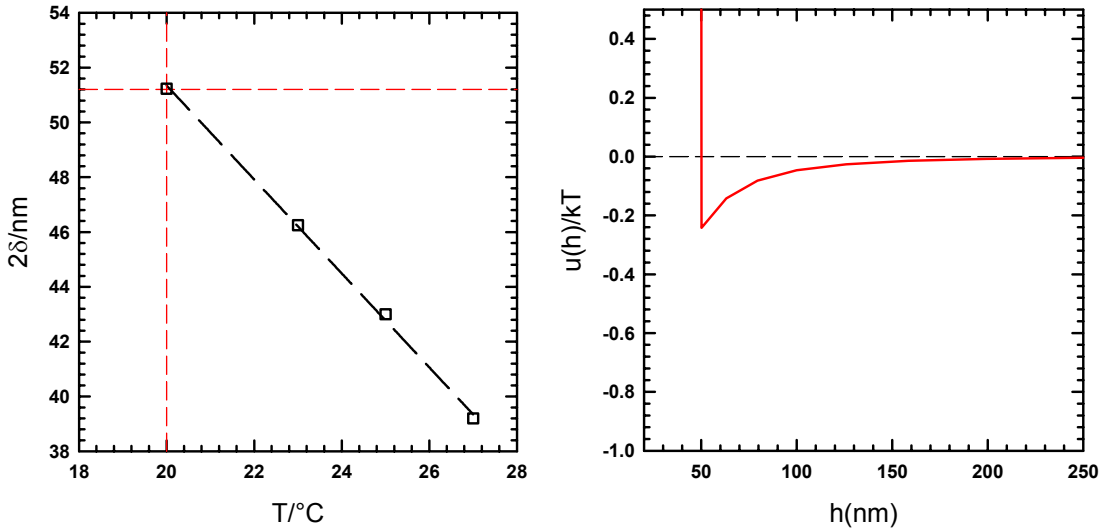

Figure 9.2. (L-R)Adsorbed layer thickness and resulting 2.34μm SiO_2 interparticle van der Waals attraction at 0.4M $MgSO_4$ at T=20°C (red lines/curve).

be equivalent.[32] We intend to use specific ion effects to achieve "equivalent" tuning of interfacial system depletion forces to achieve crystallization in much the same way as was reported in Section 6.

The main problem of using specific ion effects is the colloidal aggregation/deposition behavior that results at moderate ionic strengths. However, as shown in Section 4, moderately thick adsorbed PEO layers do an excellent job of stabilizing these interfacial systems. Understanding the differences in the way the two polymers respond to changes in temperature and the concentrations of specific ions is crucial if we are to realize our goal of specific ion mediated depletion crystallization. We intend to achieve reversible colloidal crystallization by varying the ionic strength of the aqueous solution between a mixture of 1.5mM NaCl/400mM Na_2SO_4 and 1.5mM

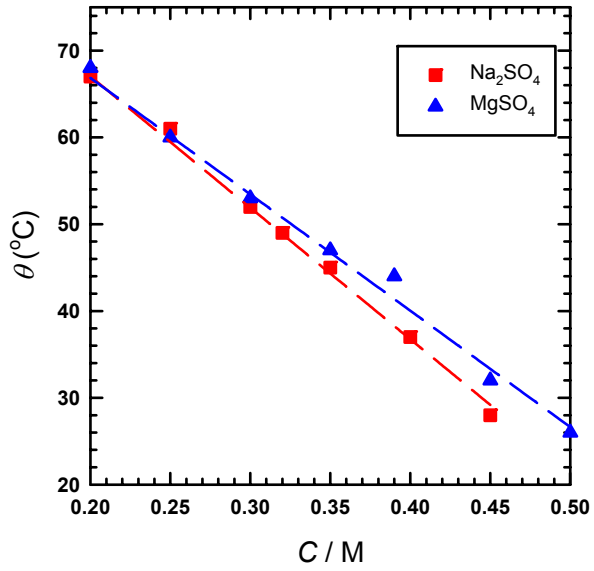

Figure 9.3. Effects of $MgSO_4$ and Na_2SO_4 salt concentrations on the theta temperature of PEO.[25]

NaCl/0mM Na_2SO_4.

Direct measurements in Section 4 suggest that the PEO brush thickness is unaffected by this solvent quality change. At solvent conditions of 1.5mM NaCl/0mM $MgSO_4$ the PEO adsorbed layers are completely solvated and are ~53nm thick. Figure 9.2 shows that at 1.5mM NaCl/400mM, the PEO layers are still at their maximum thickness (Figure 9.2, left), which corresponds to a vdW well depth of ~0.2kT (Figure 9.2, right). Changing the $MgSO_4$ concentration from 0-400mM will not affect the colloid-colloid and colloid-substrate vdW interaction at all. For this solvent quality change, the vdW interactions are constant and negligible. Note that the temperature is held constant at T=20°C for this experiment. We do not expect any change in the behavior of the PEO layers with a change from $MgSO_4$ to Na_2SO_4 (Figure 9.3).[25]

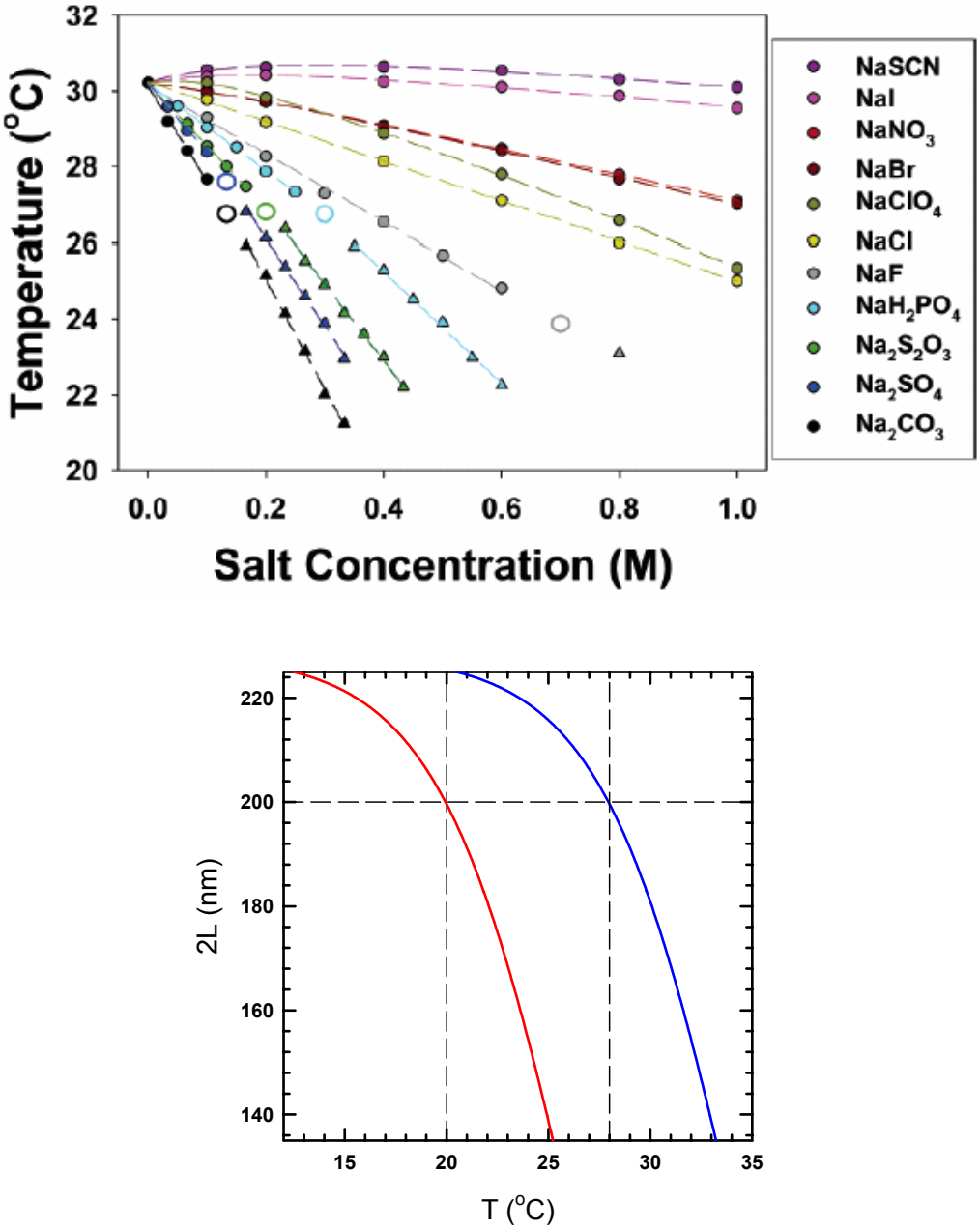

Figure 9.4. (Top)LCST values measured for sodium salts at concentrations from 0 to 1.0M.[74] (Bottom)Expected shift in PNIPAM microgel size dependence on temperature for a Na_2SO_4 salt concentration of C=0.4M (red curve) as compared to 0M (blue curve).

Figure 9.4 (top) clearly shows that when the Na_2SO_4 salt concentration is increased from 0M to 0.4M, the LCST of PNIPAM decreases by ~8°C.[74] We already have DLS data describing the change in PNIPAM depletant size with temperature in the absence of Na_2SO_4 (Figure 9.4 (bottom), blue curve). By making the assumption that like the LCST, solvent quality effects at all other temperatures are changed by the same amount, we get the red curve by translating the blue data over by 8°C. Figure 9.4 (bottom) shows that PNIPAM microgel particles have the same size at solvent conditions of T=20°C and a Na_2SO_4 concentration of C=0.4M or T=28°C and a Na_2SO_4 concentration of C=0M. Form Section 5, experiments done at T=28°C and a Na_2SO_4 concentration of C=0M gave a homogeneous fluid while lower temperatures yielded crystals.

Therefore, at T=20°C, as solvent conditions are changed from 1.5mM NaCl/0mM Na_2SO_4 to 1.5mM NaCl/400mM Na_2SO_4, the adsorbed PEO layer thickness on all surfaces should remain unaffected. As a result, the interparticle and particle substrate van der Waals attraction should remain negligible and unchanged whereas the depletion attraction will change form ~6kT at C=0M Na_2SO_4 to 3kT at C=0.4M Na_2SO_4. We already know from past experiments and measurements that this change in depletion attraction results in crystal to fluid transition. In summary, this proposed future work aims to:

- **use only specific ion effects to control the interfacial phase behavior of 2D colloids** via tunable depletion attraction.

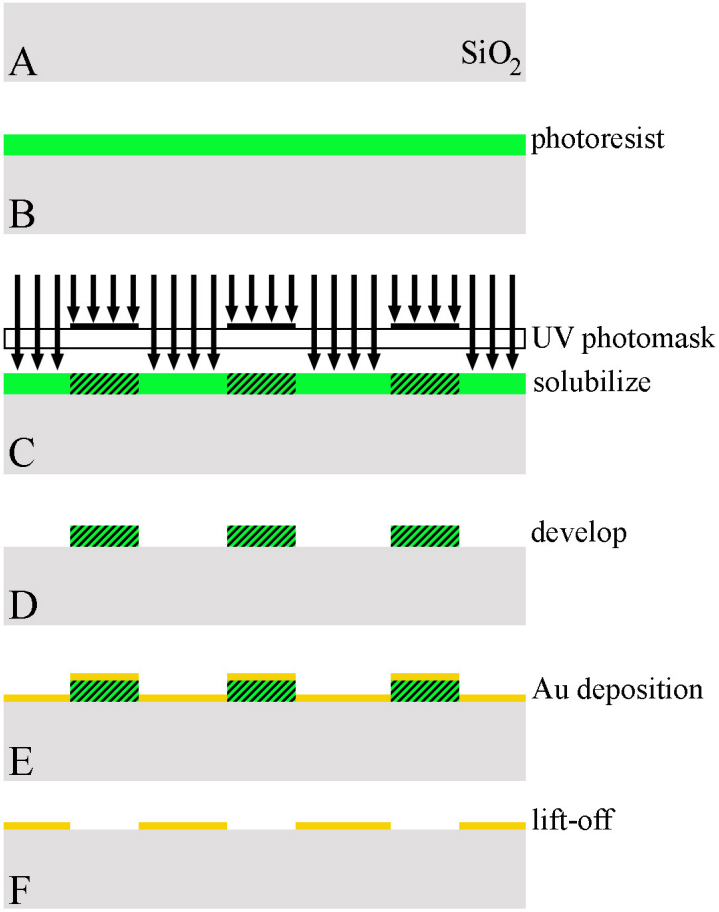

Figure 9.5. The fabrication procedure of a glass substrate patterned with gold using vapor depositions.

9.3. Spatially Controlled Crystallization on Chemical Patterns

In Section 6 we demonstrated the utility of ~310nm (4kT) physical features in controlling the spatial location of interfacial depletion attraction driven colloidal crystallization. Simulation studies performed in Section 7 were used to generate phase

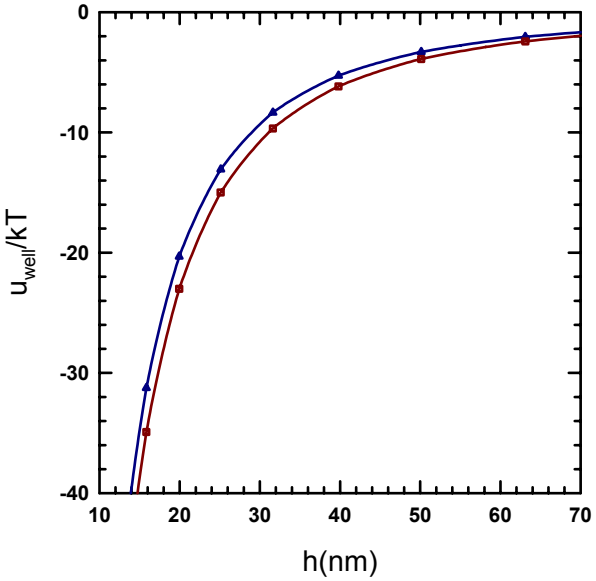

Figure 9.6. Control over 2.34μm SiO_2 particle-wall van der Waals attraction via thin deposited layers of Au. The blue curve corresponds to a 10nm deposited Au layer while the red curve corresponds to a 25nm deposited Au film. The x-axis represents surface to surface separation.

diagrams that predicted the equilibrium interfacial colloidal phase for any combination of colloid area fraction, colloid-colloid depletion attraction and physical/chemical feature well depth. We showed that these simple phase diagrams successfully predicted the phase behavior reported in the crystallization studies on the physically patterned features used in Section 7. We would like to use these phase diagrams to guide intelligent experiments in which we attempt to achieve similar spatially controlled crystallization on chemical patterns.

Chemical patterns can be easily produced by patterning nanometer thick Au films on SiO_2 surfaces (Figures 9.5, 9.6 and 7.3, bottom) to produce van der Waals energy

wells of desired depth. We will use exactly the same colloidal mixture used in Sections 5 & 6 for this proposed work. Our sample solution will consist of a mixture of 2.34μm SiO_2 colloids and PNIPAM microgel particles dispersed in a 1.5mM NaCl solution. The two types of particles were mixed in a ratio that yielded a 2.34μm SiO_2 colloid normalized area fraction of $\phi^*=1.11$ (see Section 7) and a PNIPAM microgel particle volume fraction of 24%. By adjusting the thickness of the deposited Au films, we can achieve a balance van der Waals attraction and electrostatic repulsion that translates into the 2.34μm SiO_2 colloids experiencing 12kT van der Waals attractive wells when diffusing over the Au chemical patterns. So doing, we will have set up the experiment to realize the simulation study on the micropolis circuit crystallization conducted in Section 7 (Figures 7.20, 7.21 and 7.22). In summary, this proposed future work aims to:

- **experimentally realize the 2D equivalent of the micropolis circuit on chemical patterns** via an informed, synergistic simulation-experiment approach.

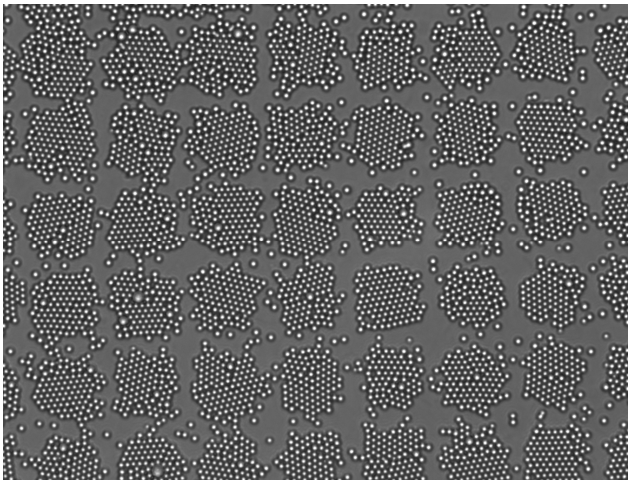

Figure 9.7. Lack of control over the orientation of attraction induced crystals of 2.34μm SiO_2 assembled over a physically patterned glass substrate.

9.4. Kinetic Control of 2D Attractive Colloidal Crystals using AC fields

In this dissertation, we have discussed the use of short-ranged interparticle attraction in inducing crystallization in interfacial colloidal systems. We have also demonstrated the use of physically patterned substrates in achieving control over the spatial location of the crystals. While crystals defects can be easily annealed out of the attractive condensed phases via temperature cycling in these systems, we have no way to control the orientation of the crystals. Figure 9.7 shows the lack of orientation control over depletion attraction induced crystallization over the physical templates reported in Section 6. We suggest the use of external AC electric fields as an alternative annealing method and as a way to achieve orientation control over the assembled crystals in Figure 9.7.

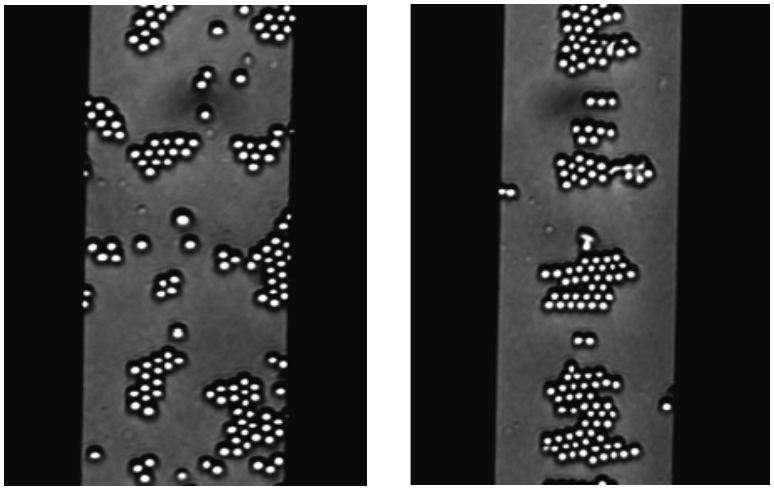

Figure 9.8. Depletion crystals of 2.2 μm SiO2 colloids between gold film electrodes with (top) no applied field, and (bottom) 2.5V-1MHz AC field resulting in crystal alignment with field via dielectrophoretic forces.

Preliminary studies on the use of lateral AC electric fields produced via thin gold films on either side of a bare glass surface region[177] for the purpose of annealing and orienting 2D crystals have been undertaken previously in the research group. In Figures 9.8 and 9.9, 2.34μm SiO_2 particles levitated above glass between gold electrode films have been subjected to lateral fields to use oscillatory electrophoretic motion to anneal polycrystalline structures and to use dielectrophoretic forces to form linear precursors to oriented, single domain crystals or square lattice structures. We plan to incorporate this work to achieve orientation control over the depletion crystals reported in this dissertation. This is the most exploratory task in this future work. In summary this proposed objective aims to:

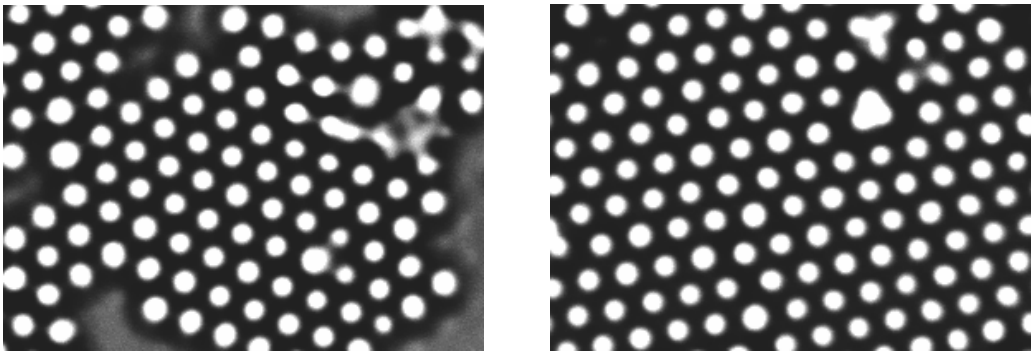

Figure 9.9. Depletion crystals of 2.2 μm SiO2 colloids between gold film electrodes with (top) no applied field, and (bottom) 2.5V-1MHz AC field resulting in an annealed hexagonally closed packed colloidal crystal.

- **investigate AC electrophoretic and dielectrophoretic forces**

normal/parallel to surface for mechanical annealing and orientation control of 2D crystallites.

REFERENCES

[1] W. B. Russel, D. A. Saville, and W. R. Schowalter, *Colloidal Dispersions*. (Cambridge University Press, New York, 1989).

[2] A. P. Gast and W. B. Russel, Phys. Today **51** (12), 24 (1998).

[3] J. D. Joannopoulos, Nature **414** (6861), 257 (2001).

[4] E. Yablonovitch, Physical Review Letters **58**, 2059 (1987).

[5] S. John, Physical Review Letters **53** (22), 2169 (1984).

[6] S. John, Physical Review Letters **58** (23), 2486 (1987).

[7] P. W. Anderson, Physical Review **109** (5), 1492 (1958).

[8] A. Z. Genack and N. Garcia, Physical Review Letters **66** (16), 2064 (1991).

[9] J. D. Joannopoulos, P. R. Villeneuve, and S. Fan, Nature **386** (13), 143 (1997).

[10] Y. A. Vlasov, X.-Z. Bo, J. C. Sturm, and D. J. Norris, Nature **414**, 289 (2001).

[11] P. Wette, H. J. Schope, and T. Palberg, Journal of Chemical Physics **123** (17) (2005).

[12] B. J. Alder, W. G. Hoover, and D. A. Young, Journal of Chemical Physics **49** (8), 3688 (1968).

[13] Z. Cheng, P. M. Chaikin, W. B. Russel, W. V. Meyer, J. Zhu, R. B. Rogers, and R. H. Ottewill, Materials & Design **22** (7), 529 (2001).

[14] Z. D. Cheng, P. M. Chaikin, J. X. Zhu, W. B. Russel, and W. V. Meyer, Physical Review Letters **88** (1) (2002).

[15] Z. D. Cheng, J. X. Zhu, W. B. Russel, W. V. Meyer, and P. M. Chaikin, Applied Optics **40** (24), 4146 (2001).

[16] W. B. Russel, P. M. Chaikin, J. Zhu, W. V. Meyer, and R. Rogers, Langmuir **13** (14), 3871 (1997).

[17] J. X. Zhu, M. Li, R. Rogers, W. Meyer, R. H. Ottewill, W. B. Russell, and P. M. Chaikin, Nature **387** (6636), 883 (1997).

[18] M. A. Bevan, J. A. Lewis, P. V. Braun, and P. Wiltzius, Langmuir **20**, 7045 (2004).

[19] M. A. Bevan and D. C. Prieve, Langmuir **15** (23), 7925 (1999).

[20] D. Rudhardt, C. Bechinger, and P. Leiderer, Phys. Rev. Lett. **81** (6), 1330 (1998).

[21] J. R. Savage, D. W. Blair, A. J. Levine, R. A. Guyer, and A. D. Dinsmore, Science **314**, 795 (2006).

[22] D. H. Napper, Transactions of the Faraday Society **64** (546P), 1701 (1968).

[23] D. H. Napper, J. Colloid. Interface Sci. **33** (3), 384 (1969).

[24] D. H. Napper, *Polymeric Stabilization of Colloidal Dispersions*. (Academic Press, New York, 1983).

[25] E. A. Boucher and P. M. Hines, Journal of Polymer Science **14**, 2241 (1976).

[26] C. Cowell and B. Vincent, J. Colloid Interface Sci. **87** (2), 518 (1982).

[27] E. Florin, R. Kjellander, and J. C. Erikson, J. Chem. Soc., Faraday Trans. I **80**, 2889 (1984).

[28] C. Cowell and B. Vincent, Journal of Colloid and Interface Science **95** (2), 573 (1983).

[29] M. A. Bevan and D. C. Prieve, Langmuir **16** (24), 9274 (2000).

[30] M. A. Bevan, S. N. Petris, and D. Y. C. Chan, Langmuir **18** (21), 7845 (2002).

[31] K. Hwang, H.-J. Wu, and M. A. Bevan, Langmuir **20** (26), 11393 (2004).

[32] G. E. Fernandes and M. A. Bevan, Langmuir **23**, 1500 (2007).

[33] S. Asakura and F. Oosawa, J. Chem. Phys. **22**, 1255 (1954).

[34] J. C. Crocker, J. A. Matteo, A. D. Dinsmore, and A. G. Yodh, Physical Review Letters **82** (21), 4352 (1999).

[35] R. Verma, J. C. Crocker, T. C. Lubensky, and A. G. Yodh, Physical Review Letters **81** (18), 4004 (1998).

[36] R. Verma, J. C. Crocker, T. C. Lubensky, and A. G. Yodh, Macromolecules **33** (1), 177 (2000).

[37] D. L. Sober and J. Y. Walz, Langmuir **11** (7), 2352 (1995).

[38] C. Bechinger, D. Rudhardt, P. Leiderer, R. Roth, and S. Dietrich, Physical Review Letters **83** (19), 3960 (1999).

[39] A. Sharma, S. N. Tan, and J. Y. Walz, Journal of Colloid and Interface Science **190** (2), 392 (1997).

[40] A. Sharma and J. Y. Walz, Journal of the Chemical Society-Faraday Transactions **92** (24), 4997 (1996).

[41] D. Rudhardt, C. Bechinger, and P. Leiderer, Journal of Physics-Condensed Matter **11** (50), 10073 (1999).

[42] L. Helden, R. Roth, G. H. Koenderink, P. Leiderer, and C. Bechinger, Phys. Rev. Lett. **90** (4), 048301 (2003).

[43] A. P. Gast, C. K. Hall, and W. B. Russel, Journal of Colloid and Interface Science **96** (1), 251 (1983).

[44] A. P. Gast, W. B. Russel, and C. K. Hall, Journal of Colloid and Interface Science **109** (1), 161 (1985).

[45] Y. Mao, M. E. Cates, and H. N. W. Lekkerkerker, Physica A **222** (1-4), 10 (1995).

[46] P. R. Sperry, H. B. Hopfenberg, and N. L. Thomas, Journal of Colloid and Interface Science **82** (1), 62 (1981).

[47] H. Dehek and A. Vrij, Journal of Colloid and Interface Science **84** (2), 409 (1981).

[48] B. Vincent, P. F. Luckham, and F. A. Waite, Journal of Colloid and Interface Science **73** (2), 508 (1980).

[49] P. N. Pusey, A. D. Pirie, and W. C. K. Poon, Physica A **201** (1-3), 322 (1993).

[50] V. J. Anderson, E. H. A. de Hoog, and H. N. W. Lekkerkerker, Physical Review E **65** (1) (2002).

[51] C. Smits, B. Vandermost, J. K. G. Dhont, and H. N. W. Lekkerkerker, Advances in Colloid and Interface Science **42**, 33 (1992).

[52] E. H. A. de Hoog, W. K. Kegel, A. van Blaaderen, and H. N. W. Lekkerkerker, Physical Review E **6402** (2) (2001).

[53] S. Ramakrishnan, M. Fuchs, K. S. Schweizer, and C. F. Zukoski, J. Chem. Phys. **116** (5), 2201 (2002).

[54] S. Ramakrishnan, M. Fuchs, K. S. Schweizer, and C. F. Zukoski, Langmuir **18** (4), 1082 (2002).

[55] S. M. Ilett, A. Orrock, W. C. K. Poon, and P. N. Pusey, Physical Review E **51** (2), 1344 (1995).

[56] A. D. Dinsmore, A. G. Yodh, and D. J. Pine, Phys. Rev. E **52** (4), 4045 (1995).

[57] P. D. Kaplan, J. L. Rouke, A. G. Yodh, and D. J. Pine, Physical Review Letters **72** (4), 582 (1994).

[58] A. D. Dinsmore, A. G. Yodh, and D. J. Pine, Physical Review E **52** (4), 4045 (1995).

[59] P. N. Pusey, W. C. K. Poon, S. M. Ilett, and P. Bartlett, Journal of Physics: Condensed Matter **6**, A29 (1994).

[60] A. Imhof and J. K. G. Dhont, Physical Review Letters **75** (8), 1662 (1995).

[61] W. C. K. Poon and P. B. Warren, Europhysics Letters **28** (7), 513 (1994).

[62] T. Biben and J. P. Hansen, Physical Review Letters **66** (17), 2215 (1991).

[63] A. D. Dinsmore, P. B. Warren, W. C. K. Poon, and A. G. Yodh, Europhysics Letters **40** (3), 337 (1997).

[64] E. K. Hobbie, Physical Review E **55** (5), 6281 (1997).

[65] E. K. Hobbie, Physical Review Letters **81** (18), 3996 (1998).

[66] E. K. Hobbie, Langmuir **15** (26), 8807 (1999).

[67] E. K. Hobbie and M. J. Holter, Journal of Chemical Physics **108** (6), 2618 (1998).

[68] E. K. Hobbie and A. D. Stewart, Physical Review E **61** (5), 5540 (2000).

[69] J. Z. Wu, B. Zhou, and Z. B. Hu, Physical Review Letters **90** (4) (2003).

[70] H. G. Schild and D. A. Tirrell, Journal of Physical Chemistry **94** (10), 4352 (1990).

[71] R. Freitag and F. Garret-Flaudy, Langmuir **18** (9), 3434 (2002).

[72] F. Hofmeister, Arch. Exp. Pathol. Pharmakol. **24**, 247 (1888).

[73] W. Kunz, J. Henle, and B. W. Ninham, Current Opinion in Colloid & Interface Science **9** (1-2), 19 (2004).

[74] Y. Zhang, S. Furyk, L. B. Sagle, Y. Cho, D. E. Bergbreiter, and P. S. Cremer, Journal of Physical Chemistry C **111** (25), 8916 (2007).

[75] Y. J. Zhang and P. S. Cremer, Current Opinion in Chemical Biology **10** (6), 658 (2006).

[76] Y. J. Zhang, S. Furyk, D. E. Bergbreiter, and P. S. Cremer, Journal of the American Chemical Society **127** (41), 14505 (2005).

[77] S. Furyk, Y. J. Zhang, D. Ortiz-Acosta, P. S. Cremer, and D. E. Bergbreiter, Journal of Polymer Science Part a-Polymer Chemistry **44** (4), 1492 (2006).

[78] R. H. Pelton and P. Chibante, Colloids and Surfaces **20** (3), 247 (1986).

[79] D. C. Prieve, Adv. Colloid Interface Sci. **82** (1-3), 93 (1999).

[80] D. C. Prieve and N. A. Frej, Langmuir **6** (2), 396 (1990).

[81] D. C. Prieve and J. Y. Walz, Applied Optics **32** (9), 1629 (1993).

[82] A. van Blaaderen, R. Ruel, and P. Wiltzius, Nature **385** (23), 321 (1997).

[83] J. P. Hoogenboom, A. K. van Langen-Suurling, J. Romijn, and A. van Blaaderen, Physical Review Letters **90** (13) (2003).

[84] J. P. Hoogenboom, A. K. van Langen-Suurling, J. Romijn, and A. van Blaaderen, Physical Review E **69** (5) (2004).

[85] J. Aizenberg, P. V. Braun, and P. Wiltzius, Physical Review Letters **84** (13), 2997 (2000).

[86] W. Lee, A. Chan, M. A. Bevan, J. A. Lewis, and P. V. Braun, Langmuir **20** (12), 5262 (2004).

[87] K.-H. Lin, J. C. Crocker, V. Prasad, A. Schofield, D. A. Weitz, T. C. Lubensky, and A. G. Yodh, Phys. Rev. Lett. **85** (8), 1770 (2000).

[88] P. Bahukudumbi and M. A. Bevan, J. Chem. Phys. **126**, 244702 (2007).

[89] T. Solomon and M. J. Solomon, Journal of Chemical Physics **124** (13) (2006).

[90] M. Trau, S. Sankaran, D. A. Saville, and I. A. Aksay, Nature **374** (6521), 437 (1995).

[91] T. Gong and D. W. M. Marr, Langmuir **17** (8), 2301 (2001).

[92] S. Yamamuro, D. F. Farrell, and S. A. Majetich, Physcial Review B **65**, 224431 (2002).

[93] C. Mio and D. W. M. Marr, Advanced Materials **12** (12), 917 (2000).

[94] P. Korda, G. C. Spalding, E. R. Dufresne, and D. G. Grier, Rev. Sci. Instr. **73**, 1956 (2002).

[95] M. M. Burns, J.-M. Fournier, and J. A. Golovchenko, Science **249**, 749 (1990).

[96] S. H. Park and Y. Xia, Langmuir **15**, 266 (1999).

[97] B. J. Ackerson and N. A. Clark, Phys. Rev. A **30** (2), 906 (1984).

[98] W. C. K. Poon, A. D. Pirie, and P. N. Pusey, Faraday Discussions (101), 65 (1995).

[99] G. Odriozola, R. Leone, A. Schmitt, J. Callejas-Fernandez, R. Martinez-Garcia, and R. Hidalgo-Alvarez, Journal of Chemical Physics **121** (11), 5468 (2004).

[100] N. A. M. Verhaegh, D. Asnaghi, H. N. W. Lekkerkerker, M. Giglio, and L. Cipelletti, Physica A **242** (1-2), 104 (1997).

[101] L. J. Kaufman and D. A. Weitz, Journal of Chemical Physics **125** (7) (2006).

[102] V. J. Anderson and H. N. W. Lekkerkerker, Nature **416**, 811 (2002).

[103] N. A. M. Verhaegh, D. Asnaghi, and H. N. W. Lekkerkerker, Physica A **264** (1-2), 64 (1999).

[104] J. C. Crocker and D. G. Grier, J. Colloid. Interface Sci. **179**, 298 (1996).

[105] D. Frenkel and B. Smit, *Understanding Molecular Simulation: From Algorithms to Applications*, 2nd ed. (Academic Press, San Diego, CA, 2002).

[106] M. P. Allen and D. J. Tildesley, *Computer Simulation of Liquids*. (Oxford Science, New York, 1987).

[107] J. F. Brady and G. Bossis, Journal of Fluid Mechanics **155** (JUN), 105 (1985).

[108] A. M. Kulkarni and C. F. Zukoski, Langmuir **18** (8), 3090 (2002).

[109] J. H. Holtz and S. A. Asher, Nature **389**, 829 (1997).

[110] G. S. Pan, R. Kesavamoorthy, and S. A. Asher, Phys. Rev. Lett. **78** (20), 3860 (1997).

[111] E. M. Lifshitz, J. Exp. Theor. Phys. USSR **29**, 94 (1955).

[112] I. E. Dzaloshinskii, E. M. Lifshitz, and L. P. Pitaerskii, Adv. Phys. **10**, 165 (1961).

[113] V. A. Parsegian and G. H. Weiss, J. Colloid Interface Sci. **81**, 285 (1981).

[114] B. A. Pailthorpe and W. B. Russel, J. Colloid Interface Sci. **89** (2), 563 (1982).

[115] A. Vrij, Pure and Appl. Chem. **48**, 471 (1976).

[116] D. C. Prieve, F. Luo, and F. Lanni, Faraday Disc. **83**, 297 (1987).

[117] H. Chew, D. S. Wang, and M. Kerker, Applied Optics **18**, 2679 (1979).

[118] H. J. Wu and M. A. Bevan, Langmuir **21** (4), 1244 (2005).

[119] H. Brenner, Chem. Eng. Sci. **16** (3-4), 242 (1961).

[120] A. J. Goldman, R. G. Cox, and H. Brenner, Chem. Engr. Sci. **22**, 637 (1967).

[121] M. A. Bevan and D. C. Prieve, J. Chem. Phys. **113** (3), 1228 (2000).

[122] H.-J. Wu, T. O. Pangburn, R. E. Beckham, and M. A. Bevan, Langmuir **21** (22), 9879 (2005).

[123] R. J. Phillips, J. F. Brady, and G. Bossis, Phys. Fluids **31** (12), 3462 (1988).

[124] J. F. Brady and G. Bossis, Ann. Rev. Fluid Mech. **20**, 111 (1988).

[125] P. R. Nott and J. F. Brady, J. Fluid Mech. **275**, 157 (1994).

[126] A. Singh and P. R. Nott, J. Fluid Mech. **412**, 279 (2000).

[127] C. W. J. Beenakker, J. Chem. Phys. **85** (3), 1581 (1986).

[128] G. M. Whitesides and B. Grzybowski, Science **295**, 2418 (2002).

[129] A. K. van Helden, J. W. Jansen, and A. Vrij, J. Colloid Interface Sci. **81** (2), 354 (1981).

[130] P. J. Flory, *Principles of Polymer Chemistry*. (Cornell University Press, Ithica, NY, 1953).

[131] P.-G. de Gennes, *Scaling Concpets in Polymer Physics*. (Cornell University Press, Ithica, NY, 1979).

[132] R. Kjellander and E. Florin, J. Chem. Soc., Faraday Trans. I **77**, 2053 (1981).

[133] J. Israelachvili, Proc. Nat. Acad. Sci. USA **94**, 8378 (1997).

[134] K. D. Collins and M. W. Washabaugh, Quart. Rev. Biophys. **18**, 323 (1985).

[135] M. G. Cacace, E. M. Landau, and J. J. Ramsden, Quart. Rev. Biophys. **30** (3), 241 (1997).

[136] R. Langer and N. A. Peppas, AIChE Journal **49** (12), 2990 (2003).

[137] C. F. Zukoski, Chemical Engineering Science **50** (24), 4073 (1995).

[138] V. A. Parsegian, J. Colloid Interface Sci. **51** (3), 543 (1975).

[139] G. J. Fleer, M. A. C. Stuart, J. M. H. M. Scheutjens, T. Cosgrove, and B. Vincent, *Polymers at Interfaces*. (Chapman & Hall, New York, 1993).

[140] V. A. Parsegian, *Van der Waals Forces*. (Cambridge University Press, Cambridge, 2005).

[141] M. A. Bevan and D. C. Prieve, in *Polymers in Particulate Systems: Properties and Applications*, edited by V. A. Hackley, P. Somasundran, and J. A. Lewis (Marcel Dekker, New York, 2001), Vol. 104.

[142] M. J. Vold, Journal of Colloid Science **16**, 1 (1961).

[143] B. Vincent, J Colloid Interface Sci. **42** (2), 270 (1973).

[144] J. Mahanty and B. W. Ninham, *Dispersion Forces*. (Academic Press, New York, 1976).

[145] D. Langbein, *Van der Waals Attraction*. (Springer-Verlag, Berlin, 1974).

[146] G. Min, M. A. Bevan, D. C. Prieve, and G. D. Patterson, Colloids & Surfaces A **202**, 9 (2002).

[147] M. A. Bevan, PhD Dissertation, Carnegie Mellon University, 1999.

[148] D. B. Hough and L. R. White, Adv. Colloid Interface Sci. **14**, 3 (1980).

[149] I. E. Dzyaloshinskii, E. M. Lifshitz, and L. P. Pitaevskii, Adv. Phys. **10**, 165 (1961).

[150] O. V. Elisseeva, N. A. M. Besseling, L. K. Koopal, and M. A. C. Stuart, Langmuir **21**, 4954 (2005).

[151] E. B. Zhulina, O. V. Borisov, V. A. Pryamitsyn, and T. M. Birshtein, Macromolecules **24**, 140 (1991).

[152] J. Czarnecki and V. Itchenskij, J. Colloid Interface Sci. **98** (2), 590 (1984).

[153] V. A. Parsegian, in *Physical Chemistry: Enriching Topics from Colloid and Surface Science*, edited by K. J. Mysels (Theorex, La Jolla, CA, 1975), pp. 27.

[154] V. S. Stenkamp and J. C. Berg, Langmuir **13**, 3827 (1997).

[155] J. A. Baker and J. C. Berg, Langmuir **4**, 1055 (1988).

[156] P. R. Sperry, Journal of Colloid and Interface Science **99** (1), 97 (1984).

[157] F. L. Calderon, T. Stora, O. M. Monval, P. Poulin, and J. Bibette, Phys. Rev. Lett. **72** (18), 2959 (1994).

[158] W. C. K. Poon, J. S. Selfe, M. B. Robertson, S. M. Ilett, A. D. Pirie, and P. N. Pusey, Journal De Physique Ii **3** (7), 1075 (1993).

[159] S. Hirotsu, Y. Hirokawa, and T. Tanaka, Journal of Chemical Physics **87** (2), 1392 (1987).

[160] T. O. Pangburn and M. A. Bevan, J. Chem. Phys. **123**, 174904 (2005).

[161] T. O. Pangburn and M. A. Bevan, J. Chem. Phys. **124**, 054712 (2006).

[162] D. Beltran, P. Bahukudumbi, and M. A. Bevan, in preparation (2007).

[163] H. G. Schild, Progress in Polymer Science **17** (2), 163 (1992).

[164] S. Anekal and M. A. Bevan, submitted (2005).

[165] C. G. d. Kruif, E. M. F. v. Iersel, A. Vrij, and W. B. Russel, J. Chem. Phys. **83** (3), 4717 (1985).

[166] M. Trau, D. A. Saville, and I. A. Aksay, Langmuir **13** (24) (1997).

[167] T. Gong, D. T. Wu, and D. W. M. Marr, Langmuir **19**, 5967 (2003).

[168] J. P. Hoogenboom, D. Derks, P. Vergeer, and A. v. Blaaderen, J. Chem. Phys. **117** (24), 11320 (2002).

[169] J. P. Hoogenboom, A. K. v. Langen-Suurling, J. Romijn, and A. v. Blaaderen, Phys. Rev. Lett. **90** (13), 138301 (2003).

[170] G. Binnig, C. F. Quate, and C. Gerber, Phys. Rev. Lett. **56** (9), 930 (1986).

[171] W. A. Ducker, T. J. Senden, and R. M. Pashley, Nature **353** (6341), 239 (1991).

[172] J. K. H. Horber and M. J. Miles, Science **302**, 1002 (2003).

[173] C. D. Frisbie, L. F. Rozsnyai, A. Noy, M. S. Wrighton, D. V. Vezenov, and C. M. Lieber, Science **265** (5181), 2071 (1994).

[174] E. Kokkoli and C. F. Zukoski, Langmuir **17**, 369 (2001).

[175] K.-B. Lee, S.-J. Park, C. A. Mirkin, J. C. Smith, and M. Mrksich, Science **295**, 1702 (2002).

[176] L. T. Mazzola, C. W. Frank, S. P. A. Fodor, C. Mosher, R. Lartius, and E. Henderson, Biophysical Journal **76**, 2922 (1999).

[177] P. Bahukudumbi, W. N. Everett, A. Beskok, G. H. Huff, D. Lagoudas, Z. Ounaies, and M. A. Bevan, Appl. Phys. Lett. **90**, 224102 (2007).

VITA

Gregory Fernandes graduated with a B.E. in Chemical Engineering from Mumbai University, India in May 2002. In August 2002, he joined the Department of Chemical Engineering at Texas A&M University as a graduate student. He graduated with an M.S. in Chemical Engineering from Texas A&M University, College Station, Texas in August 2004. In August 2008, he graduated with a Ph.D. in Chemical Engineering from Texas A&M University.

Gregory Fernandes may be contacted at gregorygrad@gmail.com or through Dr. Michael Bevan at the Chemical and Biomolecular Engineering Department, Johns Hopkins University, Maryland Hall, Baltimore, MD-21218.